

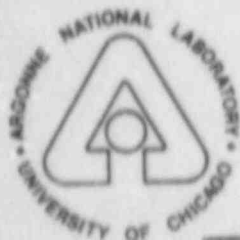
NUREG/CR-4277
ANL-85-31

NUREG/CR-4277
ANL-85-31

INVERTED ANNULAR FLOW EXPERIMENTAL STUDY

by

G. De Jarlais and M. Ishii



B507050406 B50430
PDR NUREG
CR-4277 R PDR

ARGONNE NATIONAL LABORATORY, ARGONNE, ILLINOIS
Operated by THE UNIVERSITY OF CHICAGO

Prepared for the Office of Nuclear Regulatory Research
U. S. NUCLEAR REGULATORY COMMISSION
under Interagency Agreement DOE 40-550-75

Argonne National Laboratory, with facilities in the states of Illinois and Idaho, is owned by the United States government, and operated by The University of Chicago under the provisions of a contract with the Department of Energy.

NOTICE

This report was prepared as an account of work sponsored by an agency of the United States Government. Neither the United States Government nor any agency thereof, or any of their employees, makes any warranty, expressed or implied, or assumes any legal liability or responsibility for any third party's use, or the results of such use, of any information, apparatus, product or process disclosed in this report, or represents that its use by such third party would not infringe privately owned rights.

Available from
Superintendent of Documents
U. S. Government Printing Office
Post Office Box 37082
Washington, D.C. 20013-7982

and

National Technical Information Service
Springfield, VA 22161

NUREG/CR-4277

ANL-85-31

Distribution

Codes: R2

and R4

ARGONNE NATIONAL LABORATORY
9700 South Cass Avenue
Argonne, Illinois 60439

INVERTED ANNULAR FLOW EXPERIMENTAL STUDY

by

G. De Jarlais and M. Ishii

Reactor Analysis and Safety Division

April 1985

Prepared for the Division of Accident Evaluation
Office of Nuclear Regulatory Research
U. S. Nuclear Regulatory Commission
Washington, D. C. 20555
under Interagency Agreement DOE 40-550-75

NRC FIN No. A2026

INVERTED ANNULAR FLOW EXPERIMENTAL STUDY

by

G. De Jarlais and M. Ishii

ABSTRACT

In experiments, steady-state inverted annular flow of Freon 113 in up flow was established in a transparent test section. Using a special inlet configuration consisting of long aspect-ratio liquid nozzles coaxially centered within a heated quartz tube, idealized inverted annular flow initial geometry (cylindrical liquid core surrounded by coaxial annulus of gas) could be established. In addition, inlet liquid and gas velocities were measured and varied systematically. Gas species and liquid inlet subcooling were also varied.

The hydrodynamic behavior of the liquid core, and the subsequent downstream break-up of this core into slugs, ligaments and/or droplets of various sizes, was observed, utilizing both still photographs and high speed motion pictures. In general, for low inlet liquid velocities (roughly less than 15 cm/s) it was observed that after the initial formation of roll waves on the liquid core surface, an agitated region of high surface area, with attendant high momentum and energy transfers, occurs. This agitated region appears to propagate downstream in a quasi-periodic pattern. Increased inlet liquid flow rates, and high gas annulus flow rates tend to diminish the significance of this agitated region.

Observed inverted annular flow (and subsequent downstream flow pattern) hydrodynamic behavior is reported, and comparisons are drawn to data generated by previous experimenters studying post-CHF flow.

NRC
FIN No.

A2026

Title

Phenomenological Modeling of Two-phase Flow in Water Reactor
Safety Research

TABLE OF CONTENTS

	<u>Page</u>
NOMENCLATURE.....	viii
EXECUTIVE SUMMARY.....	1
I. INTRODUCTION.....	3
A. Basic Boiling Curve/CHF Discussion.....	3
B. Post-CHF Flow Regime Prediction.....	6
II. REVIEW OF POST CHF STUDIES.....	12
III. INVERTED ANNULAR FLOW EXPERIMENT.....	18
A. Apparatus.....	24
1. Test Section.....	25
2. Heat Transfer Fluid Delivery System.....	26
3. Test Liquid Delivery/Recovery System.....	29
4. Gas Delivery System.....	30
5. Photographic Observation Apparatus.....	31
B. Experimental Procedure.....	32
1. Equipment Calibrations.....	32
2. Optical/Photographic Determinations.....	33
3. Alignment of Test Section.....	34
4. Test Runs.....	35
C. Data Formulation.....	41
IV. ANALYSIS OF RESULTS.....	42
A. Analysis of Photographic Information.....	42
B. General Flow Field Observations.....	43
1. Review of Adiabatic Inverted Annular Flow Study Results...	43
2. Hydrodynamic Behavior Observed in Present Diabatic Study.....	44
C. Discussion of Specific Flow Field Photographs.....	49
1. Figures 11 and 12: High Inlet Void Fraction.....	51
2. Figures 13 and 14: Low Inlet Void Fraction.....	51
3. Figures 15 and 16: Effect of Subcooling, Lower v_F	57
4. Figure 17: Effect of Increase v_F	57
5. Figures 18, 19 and 20: Effect of Subcooling, Very Low v_F	61

TABLE OF CONTENTS (Cont'd)

	<u>Page</u>
6. Figures 21 and 22: Agitated Region Variability, Effects of v_G and ρ_G	61
7. Figures 23, 24, 25 and 26: Details of Flow Field Structure.....	68
8. Figures 27, 28, 29 and 30: Sidelighting, Helium Inlet Gas, Flow Field Structure.....	73
D. Selected Data on Flow Regimes, Droplet Sizes.....	73
1. Formation/Motion of Agitated Film/Dense Droplet Annuli....	78
2. Droplets Generated in Agitated Region/Agitated Masses or Roll Waves.....	80
3. Dispersed Flow Droplet Sizes.....	80
4. Flow Pattern Axial Positions.....	82
V. CONCLUSIONS.....	87
A. Summary of Experimental Results.....	87
B. Comparison with Previous Post CHF Studies.....	88
C. Postulated Modeling of Phenomena Observed.....	90
ACKNOWLEDGMENTS.....	95
REFERENCES.....	96

LIST OF FIGURES

<u>No.</u>	<u>Title</u>	<u>Page</u>
1	Possible Flow Regimes in Post Dryout Region.....	4
2	Boiling Curve for Low Quality, Pool Boiling.....	5
3	Flow Regime Transitions at Dryout Point or Rewetting Front.....	7
4	Criteria for Initial Flow Regime at Dryout Point or Rewetting Front.....	8
5	Sketch of Test Facility.....	19
6a	Photograph of Test Facility, During Construction.....	20
6b	Photograph of Test Facility, During Construction.....	21
7	Sketch of Quartz Test Section, Liquid Nozzle.....	22
8	Photograph of Test Section, During Construction of Facility.....	23
9	Drawing of Test Section Inlet.....	27
10	Downstream Transitions From Inverted Annular Flow.....	50
11	Void = 0.56, $v_G = 71.6$ cm/s (N_2), $v_F = 43.4$ cm/s.....	53
12	Void = 0.56, $v_G = 154$ cm/s (N_2), $v_F = 43.4$ cm/s.....	54
13	Void = 0.37, $v_G = 1.7$ cm/s (N_2), $v_F = 15.6$ cm/s.....	55
14	Void = 0.37, $v_G = 64$ cm/s (N_2), $v_F = 15.6$ cm/s.....	56
15	$v_G = 14.1$ cm/s (N_2), $v_F = 6.3$ cm/s, $T_F = 35^\circ\text{C}$	58
16	$v_G = 14.0$ cm/s (N_2), $v_F = 6.3$ cm/s, $T_F = 14^\circ\text{C}$	59
17	$v_G = 102$ cm/s (N_2), $v_F = 6.3$ cm/s, $T_F = 14^\circ\text{C}$	60
18	$v_G = 4.5$ cm/s (N_2), $v_F = 3.2$ cm/s, $T_F = 38^\circ\text{C}$	62
19	$v_G = 4.4$ cm/s (N_2), $v_F = 3.2$ cm/s, $T_F = 27^\circ\text{C}$	63
20	$v_G = 4.6$ cm/s (N_2), $v_F = 3.2$ cm/s, $T_F = 15^\circ\text{C}$	64
21a	$v_G = 24.8$ cm/s (N_2), $v_F = 3.2$ cm/s, $T_F = 25^\circ\text{C}$	65
21b	$v_G = 24.8$ cm/s (N_2), $v_F = 3.2$ cm/s, $T_F = 25^\circ\text{C}$	66
22	$v_G = 66.5$ cm/s (He), $v_F = 3.2$ cm/s, $T_F = 24^\circ\text{C}$	67

LIST OF FIGURES (Cont'd)

<u>No.</u>	<u>Title</u>	<u>Page</u>
23	$v_G = 40.9 \text{ cm/s (N}_2\text{)}, v_F = 10.5 \text{ cm/s}, T_F = 23^\circ\text{C}.....$	69
24	$v_G = 19.0 \text{ cm/s (N}_2\text{)}, v_F = 10.5 \text{ cm/s}, T_F = 23^\circ\text{C}.....$	70
25	$v_G = 25.1 \text{ cm/s (N}_2\text{)}, v_F = 4.2 \text{ cm/s}, T_F = 15^\circ\text{C}.....$	71
26	$v_G = 29.7 \text{ cm/s (N}_2\text{)}, v_F = 4.2 \text{ cm/s}, T_F = 23^\circ\text{C}.....$	72
27	$v_G = 37.5 \text{ cm/s (He)}, v_F = 10.5 \text{ cm/s}, T_F = 24^\circ\text{C}.....$	74
28	$v_G = 97.0 \text{ cm/s (He)}, v_F = 10.5 \text{ cm/s}, T_F = 24^\circ\text{C}.....$	75
29	$v_G = 159 \text{ cm/s (He)}, v_F = 10.5 \text{ cm/s}, T_F = 24^\circ\text{C}.....$	76
30	$v_G = 66.3 \text{ cm/s (He)}, v_F = 10.5 \text{ cm/s}, T_F = 24^\circ\text{C}.....$	77
31	Droplet Sizes from Roll Waves/Agitated Surface: Trials 708, 727.....	81
32	Dispersed Flow Droplet Size Distribution, Trials 216, 224.....	83
33	Flow Pattern Axial Extents, $v_F = 4.2 \text{ cm/s (Inlet)}.....$	85
34	Flow Pattern Axial Extents, $v_F = 10.5 \text{ cm/s (Inlet)}.....$	86

LIST OF TABLES

<u>No.</u>	<u>Title</u>	<u>Page</u>
I	Initial Flow Regime.....	9
II	Post-CHF Flow Regime Transition.....	11
III	Flow Visualization for Internal Inverted Flow.....	17
IV	Flow Parameters Studied to Date (Inlet Conditions).....	36
V	Inlet Flow Parameters for Figures in Flow Field Photographic Series.....	52
VI	Agitated Annuli Formation/Motion Data.....	79

NOMENCLATURE



NOMENCLATURE

C_o	Distribution parameter, defined by Eq. (3)	Δp
d	Droplet diameter	λ
d_{max}	Average maximum droplet diameter	μ_F
d_{vs}	Volumetric mean droplet diameter	μ_G
D	Hydraulic diameter	v_F
D_J	Free jet, liquid core jet diameter	p_F
D_o	Heated flow passage diameter	p_G
g	Gravity acceleration	σ
j	Total volumetric flux ($= j_F + j_G$)	<u>Subscripts</u>
j_F	Liquid volumetric flux (superficial velocity)	F
j_G	Gas volumetric flux	G
L_B	Jet core break-up length (intact core length)	J
$N_{\mu F}$	Liquid viscosity number, defined by Eq. (6)	M
$N_{\mu G}$	Gas viscosity number, defined by Eq. (14)	rel
Re_G	Gas Reynolds number	
Re_J	Liquid jet Reynolds number	
T_F	Liquid temperature	
v_F	Liquid velocity	
v_G	Gas velocity	
v_{rel}	Relative velocity ($= v_G - v_F $)	
W_G	Volumetric gas flowrate	
$We_{G,rel}$	Gas Weber number ($= \rho_G v_{rel}^2 D_J / \sigma$)	
We_J	Liquid jet Weber number ($= \rho_F v_F^2 D_J / \sigma$)	

Greek Symbols

α	Void fraction
α_m	Mean void fraction at slug/churn transition, defined by Eq. (7)

Density difference ($\rho_F - \rho_G$)
Wavelength of maximum growth rate
Liquid viscosity
Gas viscosity
Liquid kinematic viscosity
Liquid density
Gas density
Surface tension

Liquid
Gas
Liquid jet
At flowmeter
Relative, or based upon v_{rel}

*Also Available On
Aperture Card*

**TI
APERTURE
CARD**

EXECUTIVE SUMMARY

Inverted annular flow is important in the areas of LWR accident analysis, cryogenic heat transfer, and other confined, low quality film boiling applications. And yet, while many analytical and experimental studies of heat transfer in this regime have been performed, there is very little understanding of the basic hydrodynamics of inverted annular flow. As a result, many film boiling applications are amenable to only limited analysis at present. One example of this can be seen in large-scale LWR safety codes such as TRAC and RELAP, which are essentially constrained by the not-well understood two-phase thermo-hydraulics under various accident conditions, including those resulting in inverted annular flow.

Inverted annular flow can be visualized as a liquid jet-like core surrounded by a vapor annulus. The shape of the liquid/vapor interface, the stability of the liquid jet core, and the disintegration/entrainment of this liquid core must be understood, and predictive methods established, in order to clarify the modeling of this regime and the development of interfacial transfer correlations. In typical film boiling experiments, however, control and measurement of the flow parameters necessary for such an understanding is difficult, if not impossible, to achieve. The principal objective of this study, therefore, was to systematically investigate the effect of various flow parameters on the jet core hydrodynamics, by means of a transparent test section, heated above the film boiling temperature of Freon-113. The inlet of this test section was so designed as to initiate an idealized inverted annular flow geometry (cylindrical liquid core, surrounded by a coaxial annulus of gas) at the start of the heated section. With this configuration, one can establish specific velocities, geometries and fluid properties at the test section inlet.

For relatively low inlet liquid velocities, it was observed that after liquid core expansion to proximity of the heated wall and the initial formation of roll waves on the liquid core surface, an agitated region of high surface area occurs, and tends to propagate downstream in a quasi-periodic pattern. Small droplets, typically under 400-600 μm , emerge from the downstream edges of the agitated liquid areas, while reduced-diameter remnants of the initial liquid core remain near the centerline of the test section. These

core remnants are quite smooth, and for very low liquid flow rates, often occur as multiple 1-2 mm diameter ligaments. Downstream break-up of these reduced-diameter core remnants occurs through varicose/sinusoidal jet instability. As inlet liquid flow rate is increased, the agitated region becomes less important, as more of the liquid remains in the central core. Fewer small droplets are formed, and varicose/sinusoidal break-up of the liquid core results in larger liquid slugs, which remain intact for much of the test section length. Similarly, as inlet gas velocity is increased, the agitated region again becomes less important, as more of the core is dispersed into droplets by entrainment from the crests of large amplitude roll waves near the test section inlet.

These general observations, along with more detailed specific information on the hydrodynamic behavior studied in this experiment, are presented at length, and are discussed in light of previous studies of post-CHF flow.

I. INTRODUCTION

Inverted annular flow occurs in confined boiling heat transfer systems, when low quality flow is coupled with wall surface temperature and heat flux values too high to allow direct liquid/wall contact. The resulting flow pattern is a liquid core surrounded by a blanketing annulus of vapor. Inverted annular flow may occur in light water reactor accident situations in which, after a loss of core coolant, core reflood brings coolant into the confined regions between very hot fuel rods [1] or in cryogenic heat transfer systems, such as those found in rocket propulsion applications [2]. The conditions leading to inverted annular flow, the need to understand the hydrodynamics of this regime, and previous studies of inverted annular flow are reviewed in greater detail below.

For inverted annular flow the shape of the liquid/vapor interface, the stability of the liquid jet core, and the disintegration/entrainment of this liquid core must be understood, and predictive methods established, in order to clarify the modeling of this regime and the development of interfacial transfer correlations. See Fig. 1 for the geometry of inverted annular flow. While, for confined flow conditions such as those presently under consideration, the boiling curve beyond the dry-out (CHF) point may differ greatly from the classical boiling curve (see Fig. 2) due to two-phase flow hydrodynamics, it is still illustrative of the basic problem to review the simpler, low quality pool boiling curve.

A. Basic Boiling Curve/CHF Discussion

Boiling heat transfer is a relatively complex subject, often involving two-phase thermo-hydraulics which are not well understood. Figure 2 shows a typical boiling curve for low quality, pool boiling conditions. In the segments of this curve marked BC and CD, nucleate boiling produces steadily increasing heat flux with increasing wall superheat. Heat transfer is high, due to good liquid/wall contact and convection caused by bubble motion. Nucleate boiling cannot continue indefinitely for increasing wall superheats. At some point, called the critical heat flux (CHF), the heated surface can no longer support continuous liquid contact. Zuber et al. [3] were able to explain the CHF phenomenon by examining the hydrodynamics of the vapor/liquid interface.

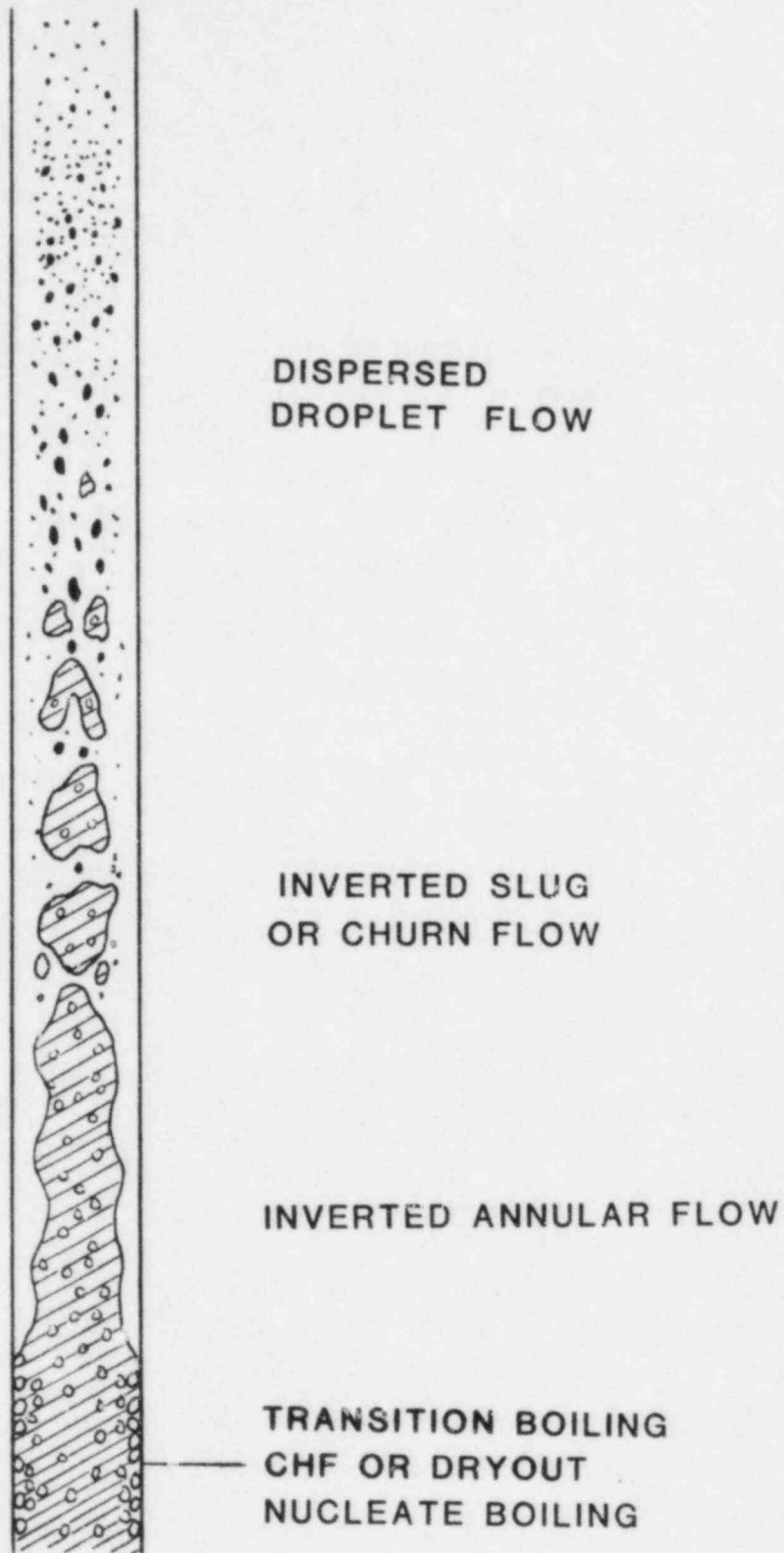
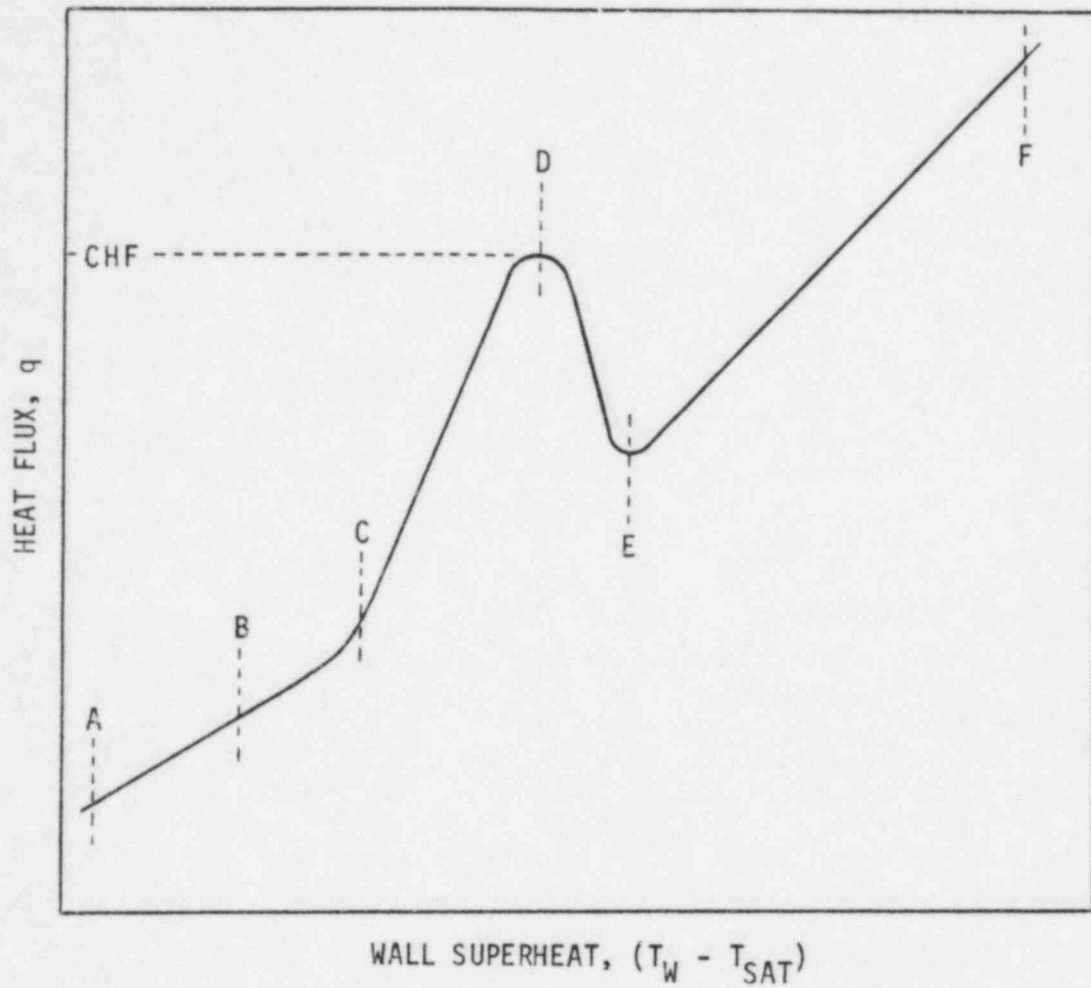


Fig. 1. Possible Flow Regimes in Post Dryout Region



- AB - NON-BOILING CONVECTION
- BC - SUBCOOLED NUCLEATE BOILING
- CD - SATURATED NUCLEATE BOILING
- DE - TRANSITION, OR PARTIAL FILM BOILING
- EF - STABLE FILM BOILING

Fig. 2. Boiling Curve for Low Quality, Pool Boiling

As nucleate boiling vapor generation increases, combined Taylor and Helmholtz instabilities cause a partial vapor blanket to form between the liquid and the heated surface, impeding heat transfer.

Beyond the CHF point, increasing wall superheat decreases the amount of liquid/wall direct contact, and the amount of heat flux. This corresponds to the curve segment DE in Fig. 2. In this transition region, nucleate boiling alternates with film boiling. Eventually, the liquid cannot come into direct contact with the heated wall, and a continuous blanket or film of vapor forms, marking the start of stable film boiling. Several different mechanisms have been proposed to predict the minimum film boiling point (point E in Fig. 2). Berenson [4] extended the hydrodynamic analysis of Zuber et al. [3] to predict a minimum film boiling wall superheat. His results are in agreement with only a limited amount of film boiling data, however. Spiegler et al. [5] proposed that the minimum film boiling point corresponds to the maximum liquid superheat predicted by van der Waals equation of state, which for low or moderate pressures is approximately equal to 0.84 times the critical temperature of the liquid. Again, only limited experimental data was found to be in agreement with this model. Henry [6] modified Berenson's analysis [4] to include the transient cooling of the heated surface due to liquid/wall contacting and evaporation of liquid microlayers wetting the wall. His results are in better agreement with experimental data than the two previous studies mentioned.

Once stable film boiling is established, heat flux again increases with increasing wall superheat. The stable film boiling region is represented by the curve segment EF in Fig. 2.

B. Post-CHF Flow Regime Prediction

When the two-phase flow hydrodynamics of confined flow become important, the boiling behavior becomes much more complicated. Flow regimes before and after CHF become important in determining heat transfer (along with mass and momentum transfer). Pre-CHF flow regimes may be predicted by using the criteria developed by Ishii and Mishima [7] and Mishima and Ishii [8], while flow regimes immediately beyond the dryout point may be viewed as the inverse forms of pre-CHF regimes [9] (see Figs. 3 and 4).

Thus the criteria for the initial flow regimes beyond the dryout point or rewetting front can be given as in Table I and in the following form [7,8].

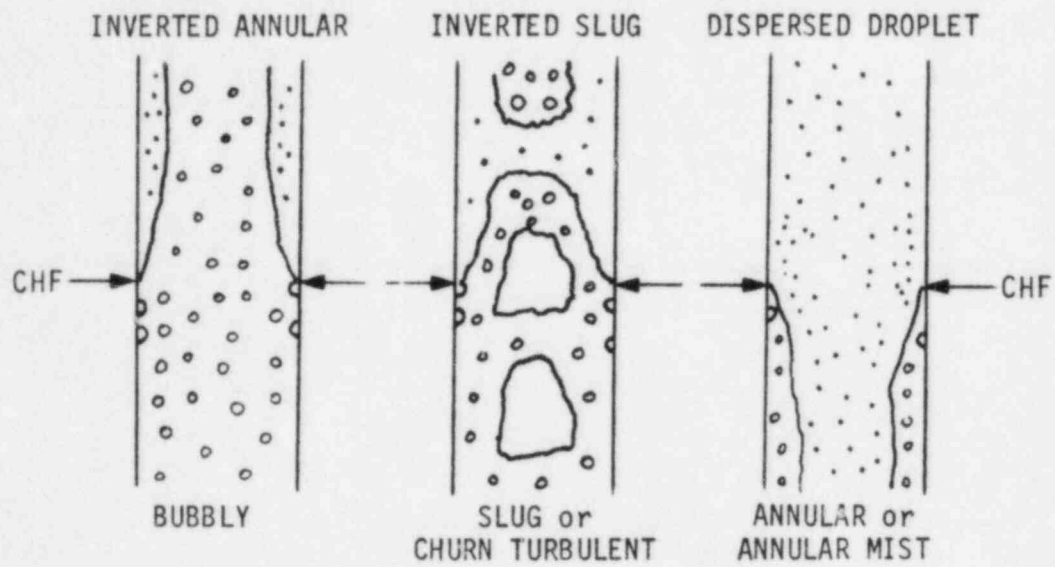


Fig. 3. Flow Regime Transitions at Dryout Point or Rewetting Front

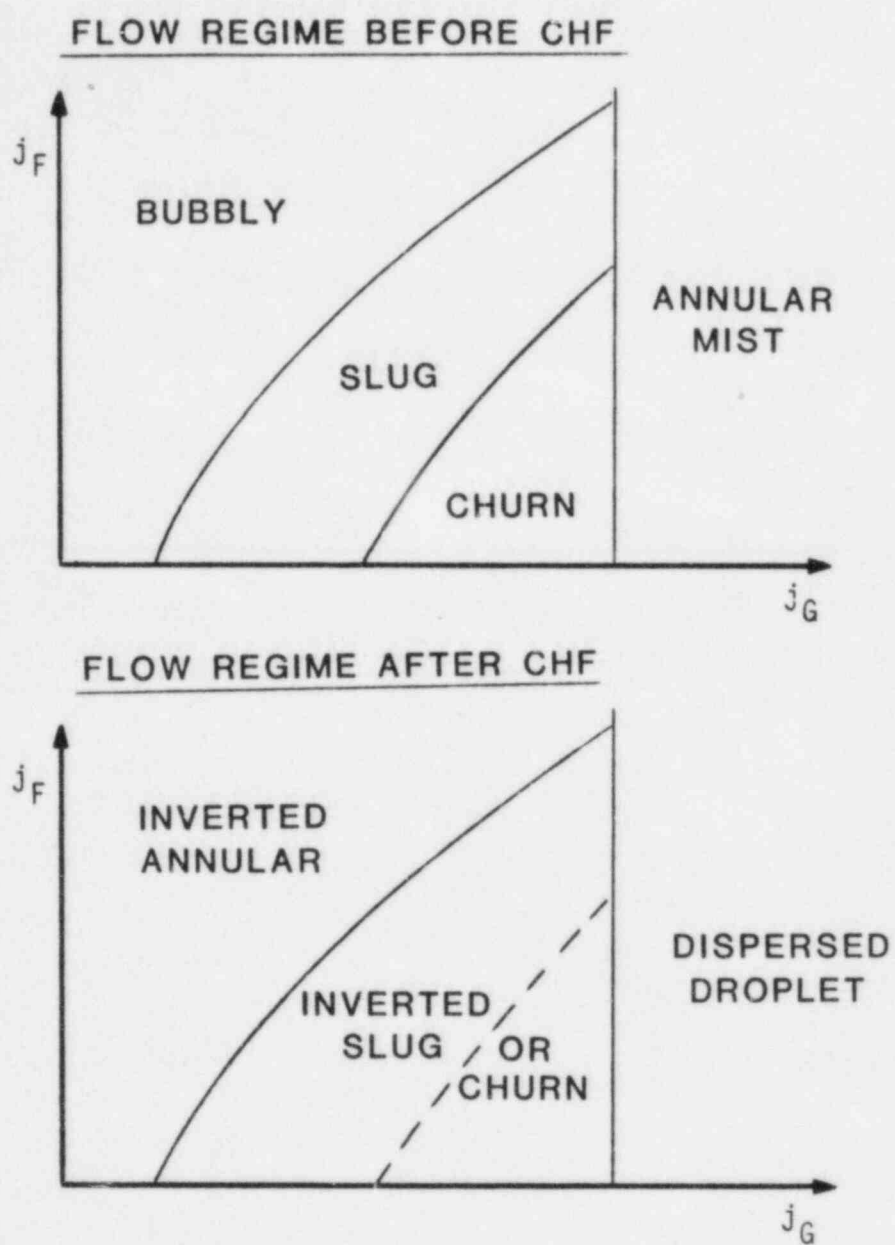


Fig. 4. Criteria for Initial Flow Regime at Dryout Point or Rewetting Front

Table I. Initial Flow Regime

Pre-CHF Flow Regime		Post CHF Flow Regime
Subcooled Liquid Bubbly	—————>	Inverted Annular Film Boiling
Slug Churn Turbulent	—————>	Inverted Slug or Churn
Annular Annular Mist	—————>	Dispersed Droplet

I. Initially Inverted Annular to Initially Inverted Slug or Churn Flow
(i.e. Pre-CHF Bubbly to Pre-CHF Slug/Churn Turbulent)

The flow regime transition criterion is given by

$$\alpha > 0.3 \quad (1)$$

for a two-fluid model formulation. For a drift flux formulation the same criterion may be expressed in terms of volumetric fluxes as

$$j_F < \left(\frac{3.33}{C_0} - 1 \right) j_G - \frac{0.76}{C_0} \left(\frac{\sigma g \Delta \rho}{2 \rho_F} \right)^{1/4} \quad (2)$$

where the distribution parameter C_0 [10], is given by

$$C_0 = 1.2 - 0.2 \sqrt{\rho_G / \rho_F} \quad (3)$$

II. Initially Inverted Slug or Churn to Initially Dispersed Droplet Flow
(i.e. Pre-CHF Slug/Churn Turbulent to Pre-CHF Annular/Annular Mist)

The transition criterion is given by

$$j_G > \sqrt{\frac{\Delta \rho g \eta}{\rho_G}} (\alpha - 0.11) \quad \text{and} \quad \alpha > \alpha_m \quad (4)$$

or

$$j_G > \left(\frac{\sigma g \Delta \rho}{2 \rho_G} \right)^{1/4} N_{\mu F}^{-0.2} \quad (5)$$

where viscosity number is given by

$$N_{\mu F} = \mu_F / \left(\rho_F \sigma \sqrt{\frac{\sigma}{g \Delta \rho}} \right)^{1/2} \quad (6)$$

Here α_m is the void fraction at the slug to churn turbulent flow transition and it is given by

$$\alpha_m = 1 - 0.813 \left\{ \frac{(C_0 - 1) j + 0.35 \sqrt{\Delta \rho g D / \rho_F}}{j + 0.75 \sqrt{\frac{\Delta \rho g D}{\rho_F}} \left(\frac{\Delta \rho g D}{\rho_F v_F^2} \right)^{1/18}} \right\}^{0.75} \quad (7)$$

The first criterion corresponds to the transition due to flooding of a liquid film along a large churn flow bubble, whereas the second criterion corresponds to the droplet entrainment induced transition.

It should be noted that the flow regime transitions within the post dryout region are quite different from the standard two-phase flow regime transitions. Consequently, the criteria for initial flow regime given by Eqs. (1) to (4) cannot be used for subsequent flow regime transitions beyond the CHF points.

For high quality, confined flow (annular flow) prior to CHF, post CHF flow is characterized by film dryout, with a transition to dispersed droplet flow. Heat transfer at the wall will be strongly influenced by droplet/wall and droplet/vapor interactions. At moderate quality, confined flow conditions, slug, or churn turbulent flow will occur prior to CHF. Just beyond CHF, the flow regime will be inverted slug, with large liquid slugs in a vapor

continuum. Transition or stable film boiling may develop, with the size and motion of the liquid slugs affecting transfer rates. Well downstream of the CHF point, break-up of the liquid slugs by the vapor stream will result in dispersed droplet flow. Finally, at low quality, confined flow conditions, pre-CHF flow will be in the bubbly or subcooled liquid regime. Beyond CHF, transition boiling and stable film boiling will result in a transition to inverted annular flow. The liquid core surrounded by a gas annulus is hydrodynamically unstable, and transfer rates across the vapor film may vary greatly with core surface wave motion [11]. After the break-up of the liquid core, inverted slug, inverted churn, or dispersed droplet flow will occur, leading to the dispersed droplet regime. The above is summarized in Table II. The boiling curves resulting from these confined flows will, in general, differ substantially from the one depicted in Fig. 2.

Table II. Post-CHF Flow Regime Transition

Pre-CHF	CHF	Post CHF		
Bubbly		Inverted Annular	→ Inverted Slug	→ Dispersed Droplet
			↘	
Slug or Churn Turbulent		Inverted Slug	→	Dispersed Droplet
Annular		Dispersed Droplet	→	Steam
Annular Mist				

From the above discussion, it becomes apparent that post CHF heat transfer cannot be properly assessed without extensive understanding of the hydrodynamics of the various two-phase flow regimes possible in confined film boiling heat transfer situations. Unfortunately, our understanding of the relevant thermo-hydraulics is far from complete. As a result, many film boiling applications are amenable to only limited analysis at present. One example of this can be seen in large-scale LWR safety codes such as TRAC and

RELAP, which are essentially constrained by limited understanding of the two-phase thermo-hydraulics possible under various accident conditions, including those resulting in inverted annular flow.

A brief review of our present knowledge of post CHF heat transfer in general is given in the next section, as is a more detailed summary of previous experimental work on the hydrodynamics of this region.

II. REVIEW OF POST CHF STUDIES

Even a brief discussion [12] of post CHF hydrodynamic behavior reveals that our knowledge of the relevant thermo-hydraulics is still quite limited. Prior to 1950, one of the few significant works in the area was the 1756 treatise by Leidenfrost, who observed the film boiling of small droplets on heated surfaces. Following early studies such as those by Bromely et al. [13] and Hsu and Westwater [14], a great deal of post CHF research has been done. Most of the research carried out has been focused on the heat transfer aspect of the problem. There are a large number of heat transfer correlations for this region as reviewed and tabulated by Kalinin et al. [15], Groeneveld and Gardiner [16], Groeneveld [17], Collier [18], and Mayinger and Langner [19]. Existing experimental data were also reviewed in the above mentioned papers. Experimental data up to 1970 is reviewed in great detail by Clements and Colver [20]. Nearly 200 film boiling data for cryogenic fluids, organic fluids, water, and liquid metals are tabulated. Review articles have also been written by Hsu [21] and by Bressler [22]. A large number of empirical or semi-empirical heat transfer correlations have also been proposed based on these data. There are few phenomenological models however, these are generally of a heuristic or hypothetical nature. In the absence of detailed hydrodynamic data, it is nearly impossible to establish a reliable mechanistic model for the complicated two-phase flow phenomena in this post CHF region.

It can be said that very limited studies have appeared on the hydrodynamic mechanisms of the post CHF two-phase flow as invariably pointed out in these review articles. The main reason for this lack of information on the flow characteristics is the considerable experimental difficulties associated with flow measurements in this region. Due to the high temperature of the wall to sustain the film boiling, a flow visualization requires special

attention. Furthermore, local flow and temperature measurements of liquid and vapor in this adverse two-phase flow condition is extremely difficult or costly. Often the heat transfer and hydrodynamics are so tightly coupled such that it is almost impossible to obtain clean hydrodynamic data.

Some understanding of the film boiling mechanisms has been obtained from visual observations such as those using high speed motion pictures and flash photography. In view of the difficulties associated with flow instrumentation, the visual studies have been quite important for the researchers to obtain an insight to the interfacial characteristics, flow regimes, and heat transfer mechanisms. There are a sizable number of photographic studies of film boiling for external flows [20]. For example, Hsu [23], Hsu and Westwater [14], and Coury and Dukler [11] measured the interface wave characteristics for film boiling from a vertical surface. A similar study for a vertical cylindrical heater was carried out by Arif Caglar and Madsen [24].

However, the extent of visual studies for film boiling in channels is much more limited. Film boiling of liquid hydrogen in a horizontal tube was studied by Chi and Vetere [25], Chi [26], and Chi [2]. The experiment was carried out under the transient quenching conditions. The existence of three regimes, i.e., inverted annular, inverted slug, and dispersed droplet flows was observed. Chan [27] performed rewetting experiments of a hot horizontal glass tube. A significant stratification of the liquid core has been observed, thus the quenching of the bottom of the pipe precedes that of the mid-side or top.

A visual experimental study of liquid nitrogen film boiling in a vertical tube by Laverty and Rohsenow [28] demonstrated that similar two-phase flow regimes also existed in a vertical up flow system. The inverted annular flow which exists at very low quality is broken up at higher qualities to form liquid slugs and dispersed droplets. The drag force on the liquid core increases downstream due to higher gas flux and eventually the core is torn apart into filaments and droplets. Forslund and Rohsenow [29] extended the above experiments and measured the droplet size at the exit of the heated section. It was observed that the size of the droplets present appeared to be relatively insensitive to the liquid flow rate and quality, however, it was affected strongly by the heat flux. Smaller droplets were observed at higher heat fluxes. The measured droplet size of 100 to 1000 microns should represent the upper end of the droplet size distribution.

Kalinin et al. [30-32] performed similar experiments using liquid nitrogen in a vertical down flow system. They also confirmed the existence of inverted annular, slug, and dispersed droplet flows. However, they observed a different mechanism of liquid core disintegrations in this transient quenching experiment. They explained that the cyclic changes in the flow regime between the inverted annular and slug flows were caused by the cyclic pressure changes at the leading edge of the liquid due to rapid vaporization. Similar behavior was also observed in vertical up flow film boiling (Banerjee [33]). This type of cyclic oscillations of the liquid core may be particularly notable in a boiling flow in a glass tube. It is well-known (Ishii [34] and Jeglic and Grace [35]) that boiling inside a glass tube is much more unstable due to thermodynamic nonequilibrium. Because of poor nucleation characteristics of a smooth surface, the liquid can be highly superheated in the quench zone. This leads to quite unstable boiling and oscillating inlet conditions for the film boiling region.

Important visual observation studies of film boiling based on high speed movies were made for flow in a rod bundle by Cadek et al. [36] and Lee et al. [37]. Cadek et al. [36] carried out experiments on flow regimes in the FLECHT facility. The experimental conditions were transient quenching or rewetting of a rod bundle with upward vertical water flow at 3.7 to 4 atm pressure. The observed two-phase flow regimes were similar to those recorded in single tube experiments. The high speed movies (967 frames/sec) were taken through a 12 cm square window at one side of the rod bundle. Various flow regime boundaries were recorded as a function of time as these flow regimes moved upward. The existence of seven flow regimes, nucleate boiling, transition boiling, film boiling, flow pattern transition, dispersed droplet, and steam regimes were visible. A stable film boiling regime existed just above the quench front or leading edge of the transition boiling regime. The interfacial wave velocity was from five to ten times the liquid velocity. The wave length was about 1.3 cm, or slightly larger than the rod diameter. An unstable flow pattern transition regime existed between the stable film boiling and dispersed flow regimes. In this regime flow changed from mostly liquid flow to mostly vapor flow. It was highly turbulent and the interface was very unstable.

Lee et al. [37] carried out droplet velocity and size distribution studies using high speed movies in the FLECHT SEASET series of experiments. With

the photographic technique used, the data is limited to relatively large droplets. The droplet sizes of 0.3 to 1.5 mm and velocities of 0.2 to 12 m/sec were reported. These give valuable information on the dispersed droplet regime of the post CHF region.

Cumo et al. [38] studied the rewetting of a hot wall by a falling water film. The formation of rivulet flow and subsequent droplet generations by sputtering of a liquid film were observed. Two different size groups of droplets were generated. A large number of smaller droplets having the mean diameter of about 0.2 mm were generated by escaping vapor bubbles near the tip of the rivulet. The larger droplets were generated due to the detachment of the rivulet by the film boiling. The mean diameter of the larger droplets was in the order of 3 mm.

A simulation study of inverted annular flow was performed by Ishii and De Jarlais [9,39-42] using coaxial jets of water and various gases in a glass tube. The liquid core disintegrated into droplets in two different mechanisms, i.e., wave instabilities at the interface and roll-wave entrainment. Since both the liquid and gas fluxes were measured, it was possible to quantify the liquid core disintegration in terms of flow conditions. Two different droplet size groups were identified and size distributions were measured.

Recently, Costigan and Wade at Harwell [43] performed a flow visualization study of the reflooding of a hot vertical tube using dynamic neutron radiography. The test tube was 0.925 cm ID and 60 cm in length, and was exposed to a low energy neutron beam from a material testing nuclear reactor. The quenching phenomena within the tube was visualized by using a neutron imaging system and from this a video movie of real time images was made. At the beginning of the inverted annular flow, pinching of the liquid core jet was observed. In the downstream section the liquid jet was in violent motion and appeared to break down within about 10 cm. The breakdown was either due to varicose or sinuous instabilities and typical jet instability motions were visible. The important characteristic of the neutron radiography is that it can locate the liquid mass clearly. On the other hand, the optical method tends to show the detail of interfacial structures. Therefore, these two methods compliment each other in studying the hydrodynamics of inverted flow.

Besides these flow visualization experiments, only a limited number of studies have been made for the understanding of fluid mechanics of the post

CHF region. For example, the hydraulic resistance was measured and correlated by Kalinin et al. [31] and by Graham et al. [44]. Ottosen [45] obtained the void fraction measurement using γ -ray absorption technique in the flow visualization experiments in a vertical glass tube with liquid nitrogen as a coolant. He noted that at void fractions above 80% at atmospheric pressure, the inverted annular flow changed to dispersed droplet flow. Kurilenko et al. [46] measured void fraction during the transient quenching of a steel tube, using liquid hydrogen in both vertical up flow and vertical down flow. In many of the above mentioned experiments, the significant effects of subcooling on the stability of film boiling were reported. With highly subcooled liquid, the considerable portion of the heat added to the coolant goes into heating up of the subcooled liquid core. This reduces the production of vapor. Since the relative velocity between vapor and liquid contributes significantly to the instability of the interface, this stabilizing effect of subcooling can be explained. A recent development of the measurement technique of vapor superheat in the post CHF regime (Nijhawan et al. [47] and Gottula et al. [48]) also increased the experimental information on the flow field.

In an analytical study of inverted annular flow hydrodynamics, Jensen [49] investigated the stability of the liquid jet-like core which develops immediately beyond the CHF point. His predictions for the length of the intact liquid core, and maximum growth rate wavelength on the liquid core surface are in general agreement with observations made during the FLECHT SEASET series of experiments [36,37].

The various hydrodynamic studies of the post-dryout regime are summarized in Table III. In spite of these efforts, the present understanding of the hydrodynamics of the post CHF region is very limited. This leads to the initial development of various empirical or semi-empirical correlations (Groeneveld and Gardiner [16] and Groeneveld [17]) for the heat transfer coefficient without considering the details of the flow characteristics. However, applications of such a correlation method is limited to well-understood flow conditions. When these correlations are applied to complicated transient conditions, some unexpected discrepancies can show up in analyses.

As was previously stated, much of the difficulty in obtaining sufficient data on the hydrodynamic behavior of post CHF two-phase flow results from the close coupling of heat transfer and hydrodynamics in this region. In

Table III. Flow Visualization for Internal Inverted Flow

Classification	Fluid	Observation
Quenching in Horizontal Flow Chi & Vetere [25], Chi [26], Chi [2] Chan [27]	H ₂ Water	Flow Regime Flow Regime
Quenching in Vertical Up Flow Kurilenko et al. [45] Lavery & Rohsenow [28] Forslund & Rohsenow [29] Ottosen [44] Banerjee [33]	H ₂ N ₂ N ₂ N ₂ Water	α Flow Regime Drop Size α Flow Regime
Quenching in Vertical Down Flow Kurilenko et al. [45] Kalinin et al. [30-32]	H ₂ N ₂	α Flow Regime Δp
Quenching Rod Bundle Cadek et al. [36] (FLECHT) Lee et al. [37] (FLECHT)	Water Water	Flow Regime Drop Size, Velocity
Adiabatic Simulation in Down Flow De Jarlais [40], De Jarlais & Ishii [41,42]	Water - N ₂ } He } gas R-12 }	Flow Regime Jet Break-up Drop Size Volumetric Fluxes

addition, it is experimentally difficult and/or costly to measure flow rates in these film boiling two-phase flow conditions. And, in the transparent test sections needed for visual observation of the flow field, it is difficult to establish steady-state conditions, so that transient behavior (either the general phenomenon of the advancing quench front, or the instability caused thermodynamic non-equilibrium [30-33]) often results in continually changing

conditions (void fraction, liquid and vapor flow rates, flow regime, liquid subcooling, etc.) at the point in the test section where film boiling commences.

Given these considerations, the adiabatic inverted annular flow simulation of Ishii and De Jarlais [9,39-42] offered many experimental advantages. Steady-state flow was possible, inlet flow conditions could be measured and varied systematically, the coupling between heat transfer and hydrodynamics was eliminated, and film boiling heat transfer and temperatures need not be maintained. However, the fact that film boiling did not occur in the test sections of this simulation limited the amount of useful experimental data which could be obtained. Specifically, these limitations are the following:

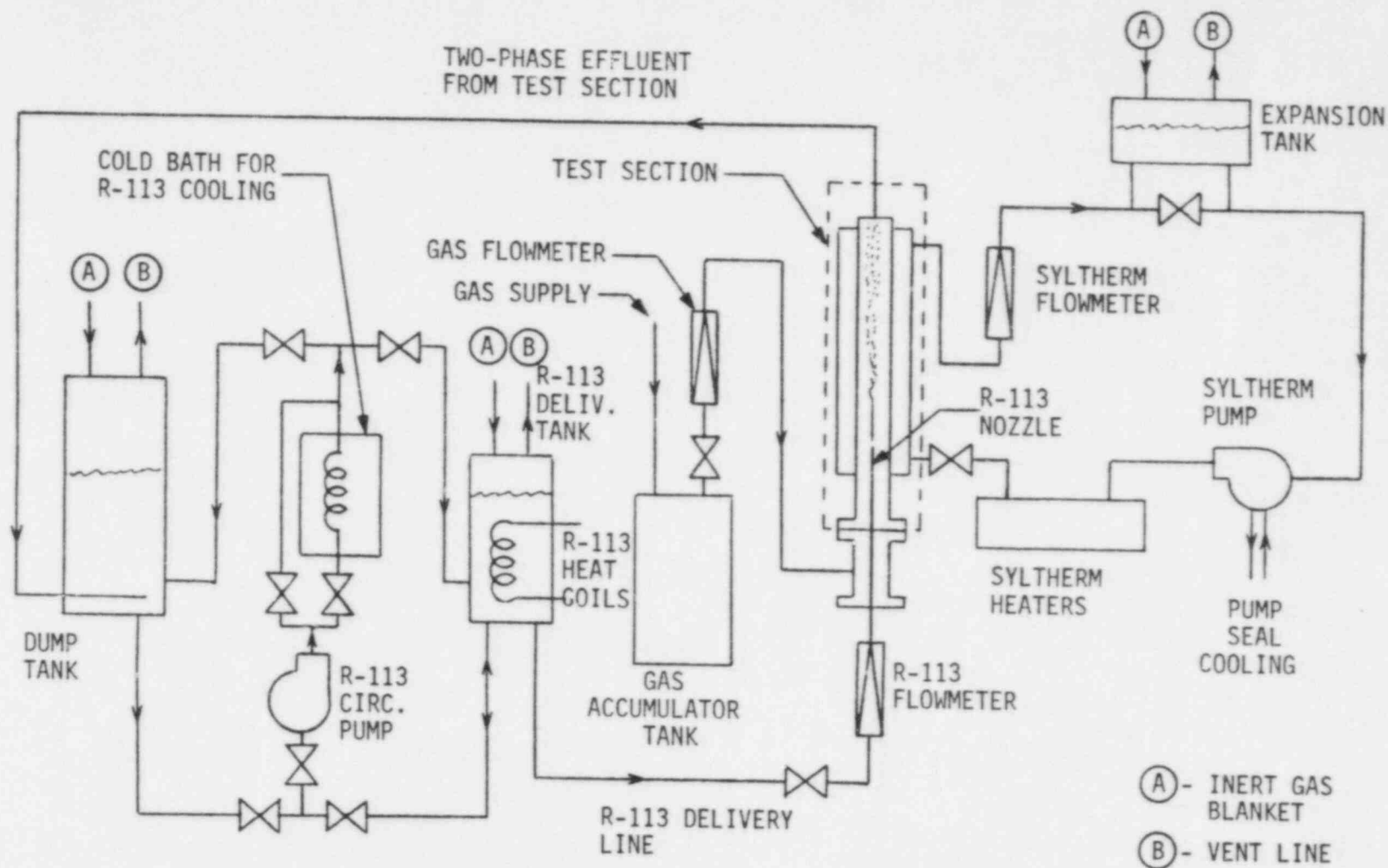
- 1) wetting of the wall by impinging liquid droplets or the unstable liquid core,
- 2) utilization of down flow only,
- 3) no opportunity to observe secondary break-up of the liquid core or unstable slugs/drops beyond the point of wall wetting (due to limited visibility through the annular film which formed),
- 4) use of high liquid flow (above 65 cm/s) only, and
- 5) no effect of phase change (no radially inward force due to vapor generation as liquid surface nears wall, etc.).

Given these limitations, a new experimental facility has been constructed in which steady-state film boiling flow conditions can be maintained, while incorporating the inlet design features of the previous adiabatic simulation, so that flow conditions at the start of the stable film boiling region can be measured and varied systematically. Details of this experimental facility are discussed in the next section.

III. INVERTED ANNULAR FLOW EXPERIMENT

An experimental test facility was constructed to study steady-state film boiling in a transparent quartz tube, using Freon-113 as the test fluid. In addition, simplified inverted annular flow geometry consisting of a cylindrical jet-like core of liquid surrounded by a gas annular jet can be established at the start of the heated portion of the test section. This is accomplished

Fig. 5. Sketch of Test Facility



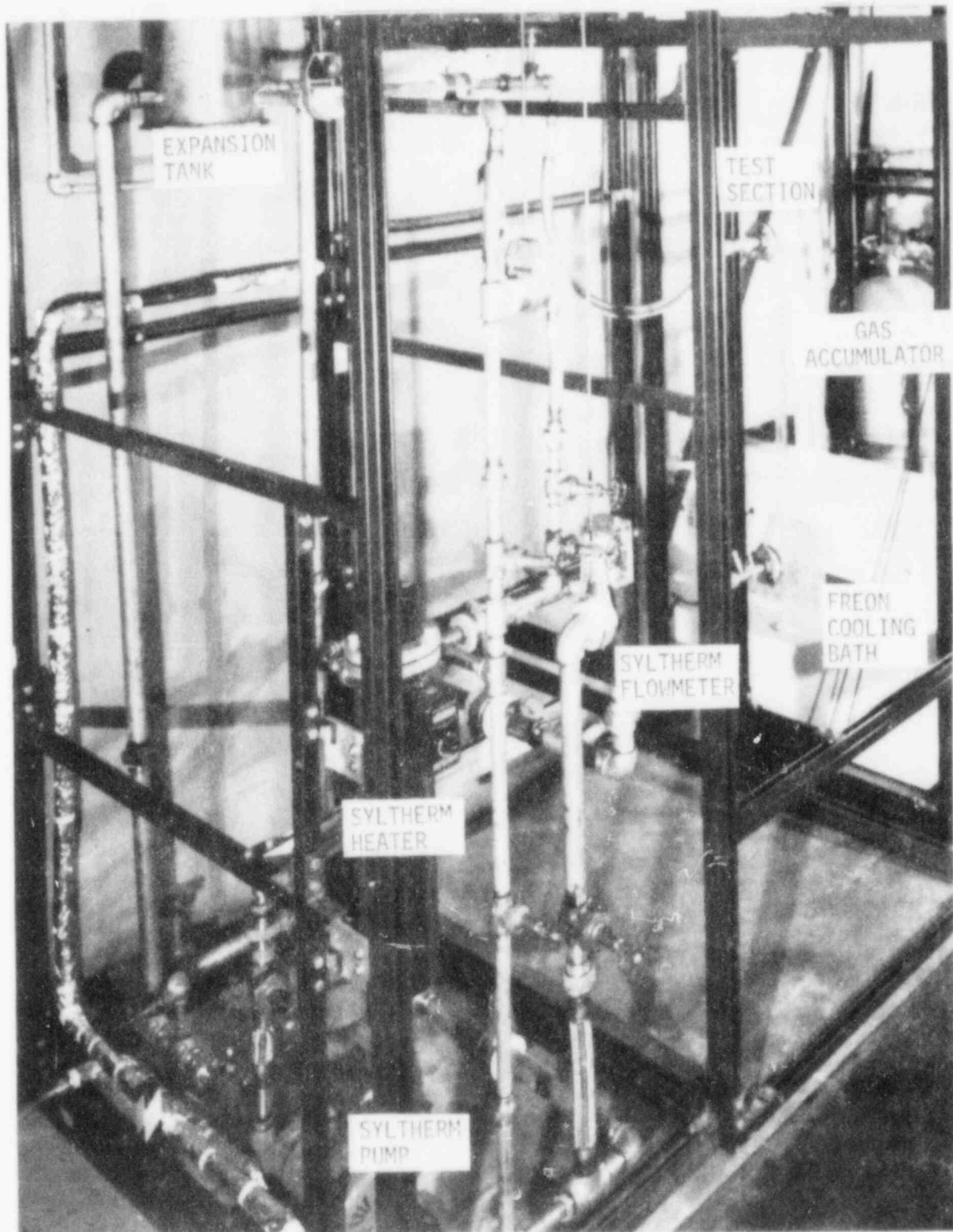


Fig. 6a. Photograph of Test Facility, During Construction

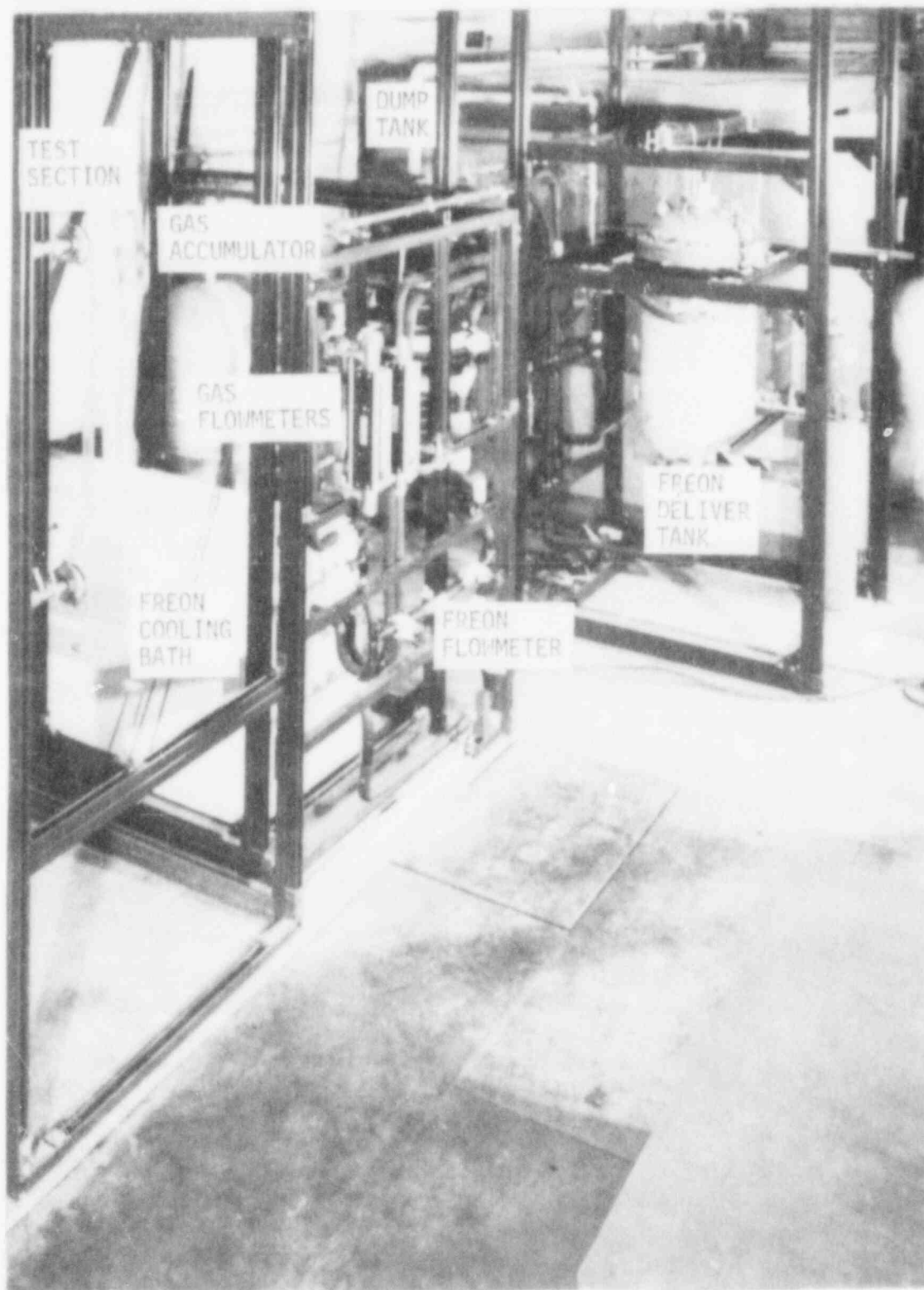
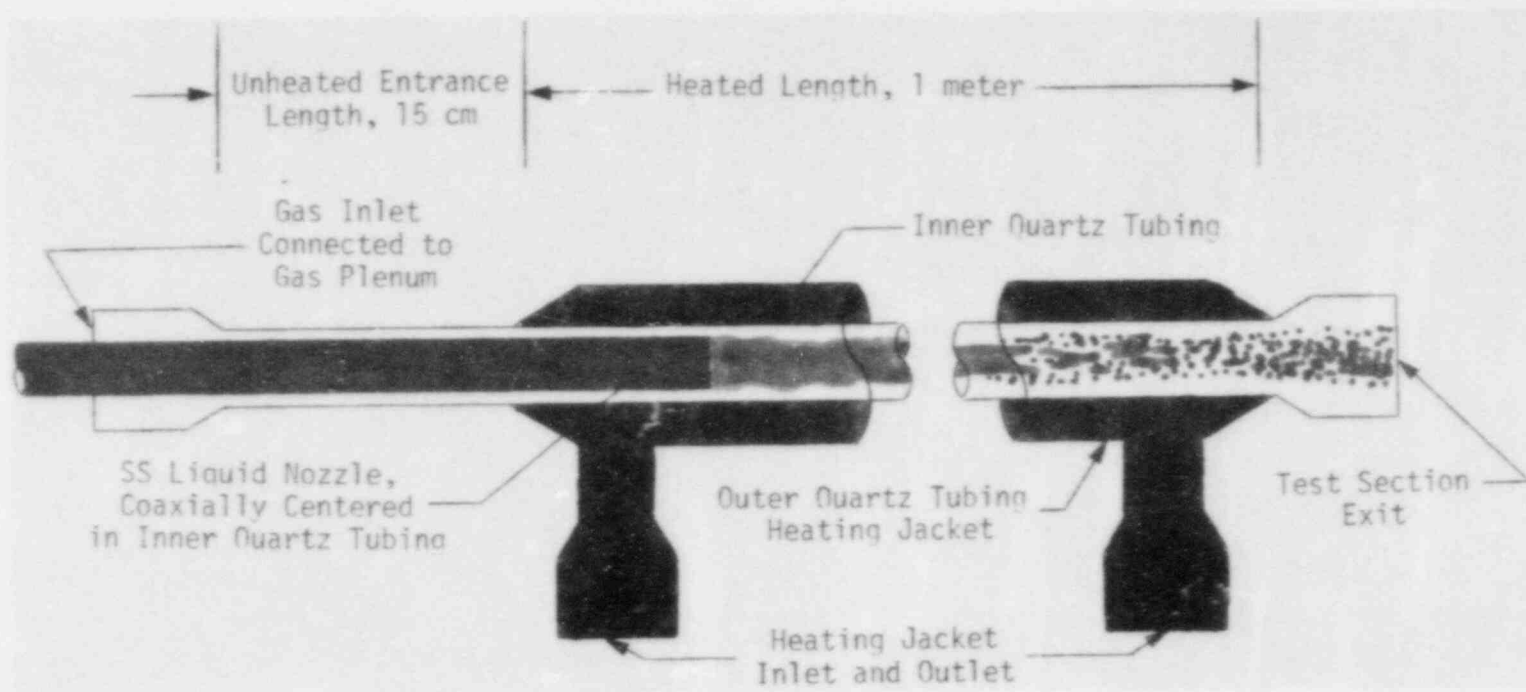


Fig. 6b. Photograph of Test Facility, During Construction

Fig. 7. Sketch of Quartz Test Section, Liquid Nozzle



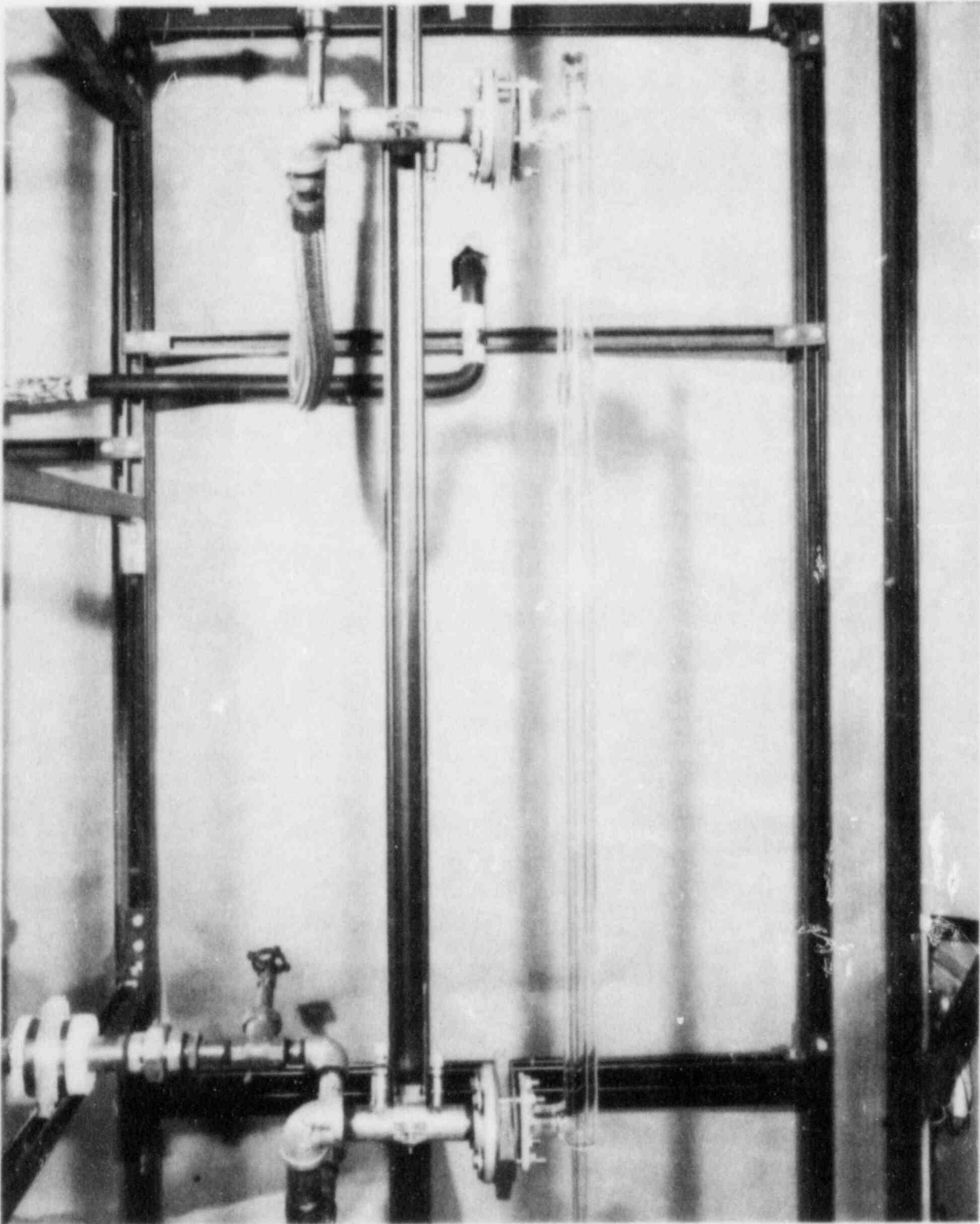


Fig. 8. Photograph of Test Section, During Construction of Facility

by introducing the test fluid into the test section core through thin-walled tubular nozzles coaxially centered within the heated quartz tubing, while vapor or gas is introduced into the annular gap between the liquid nozzle and the heated quartz tubing. This technique, first used in the adiabatic simulation of inverted annular flow discussed earlier [9,39-42], allows one to fix the initial geometry of the flow field, and to measure and vary systematically gas and liquid flow rates. In addition, one can vary the gas species injected into the annular gap to study, for instance, the effect of gas density upon the hydrodynamics of the system.

Pressure in the test section cannot be varied or controlled, and was always near atmospheric. Flow through the test section is upward. Wall temperatures of 265°C or above can be maintained during steady-state low quality film boiling of Freon 113. Information is obtained through flash photography or high speed motion pictures taken anywhere along the full length of the heated test section.

The apparatus and test procedures of this experimental study are described in the following portions of this section.

A. Apparatus

The test facility is shown schematically in Fig. 5. Figure 6 is a photograph of the test facility near completion of construction. Central to the operation of this facility is the heated quartz test section, which is sketched in Fig. 7. Figure 8 is a photograph of the test section in place during construction of the test facility. Basically, the test section consists of two coaxial quartz tubes. A heat transfer fluid (Syltherm 800, by Dow Corning, in all test trials to date) circulated through the annular gap between the quartz tubes maintains the temperatures and heat input necessary to establish film boiling heat transfer at the inner surface of the inner quartz tube. Freon-113 (liquid) and, if desired, various gases are metered and delivered to the test section inlet. The two phase flow leaving test section is dumped into a pool of highly subcooled Freon-113, which acts as a direct contact heat exchanger, condensing and cooling the Freon-113 leaving the test section, and allowing any non-condensable gases delivered at the test section inlet to vent to the atmosphere. The component parts of this system are discussed in the following paragraphs.

1. Test Section

The heated portion of the test section consists of two coaxial quartz tubes, fashioned in much the same manner as Liebig or West condensers. In all test trials to date, the inner quartz tube has been 16 x 13.6 mm OD/ID, and the outer quartz tube has been 35 x 31 mm OD/ID, resulting in an annular gap of 31 x 16 mm OD/ID through which the high temperature heat transfer fluid is pumped. This heated portion of the test section has been fixed at 100 cm in length in all tests to date, although lengths from approximately 50 cm to 120 cm could be accommodated in the structure supporting the test section. The inner quartz tube is extended beyond the outer quartz tube to provide an unheated entrance length. This length has been fixed at 15 cm in all tests to date, but can be varied in conjunction with variations in the heated length of the test section.

Piping connections to the quartz test section are accomplished through the use of quartz, one inch Conical Pipe (Pyrex brand) end connectors, which are fused onto the quartz tubing and can be bolted directly to gasketed (silicon rubber) one inch stainless steel pipe flanges. The quartz test section is installed vertically, with the test fluids injected upward, through the unheated entrance length, and the heat transfer fluid flowing downward, countercurrent to the test fluids. To minimize stress on the quartz tubing, all piping runs include flexible steel hose lengths, and the piping connected to the inner quartz tube are "floating," using a suspension system of springs and guides to isolate the quartz tubing from any piping loading.

Inverted annular flow can be established in this test section by heating the heat transfer fluid above minimum film boiling temperatures, and then introducing saturated or subcooled test fluids (such as R-113) into the inner quartz tube directly. In addition, simplified inverted annular flow geometry (liquid cylindrical core, gas annulus) can be established by introducing the test liquid into the heated portion of the test section through stainless steel thin-walled tubular nozzles of various sizes. These nozzles are coaxially centered within the unheated length of the inner quartz tube by six spacing pins soldered onto the steel tubes. Various gases (nitrogen, helium, Freon vapor, etc.) can be introduced into the annular gap between the liquid core nozzle and the inner quartz tube wall through an annular plenum below the quartz test section. In this configuration, initial geometry is

simplified (coaxial liquid core and gas annulus jets, with circular cross sections) and inlet conditions (gas and liquid velocities, void fraction) can be controlled. See Fig. 9 for a drawing of test section inlet. To minimize flow disturbances at the liquid nozzle exit, the nozzle spacing pins are placed at a distance from the nozzle exit equal to at least 50 times the width of the gap between the nozzle and the quartz wall. In addition, nozzle tube wall thickness, while small to begin with (.0155 m - 0.255 mm in the nozzles available for use), was reduced further near the nozzle exit, ending in a knife edge at the exit itself, so that no sudden change in the gas annulus flow area occurs. All nozzle lengths are at least 50 times the nozzle ID, to minimize entrance effects. In the test trials to date, nozzles with 9.02 mm and 10.8 mm ID have been used, giving inlet void fractions of 0.56 and 0.37, respectively, in conjunction with the inner quartz tube ID of 13.6 mm. See Ref. [40] for details of the tubular nozzle fabrication.

Pressure taps are located at the inlet to the tubular liquid nozzles, in the piping near the one inch Conical Pipe end connector at the start of the unheated length of inlet quartz tubing, and in the piping near the one inch Conical Pipe end connector at the two-phase flow outlet from the heated portion of the test section. Thermocouples (Type K) are inserted into the flow streams at the same points as the above-mentioned pressure taps, and are also inserted into the flow of heat transfer fluid entering and leaving the heated portion of the test section.

The test section is located within a steel enclosure, with a one inch thick Lucite view port allowing observation of the full length of the test section. This enclosure, with one side open and leading off to an unoccupied area, is necessary, since contact with the hot test section and heat transfer fluid piping (temperatures of 265°C and above) could be hazardous. More importantly, the steel enclosure protects against the possible results of test section failure (splashing of hot fluids, fumes from test liquids such as R-113, possible vapor explosion if the cold test liquid and warm heat transfer fluid mix, etc.).

2. Heat Transfer Fluid Delivery System

For all trial runs to date, the heat transfer fluid used to heat the quartz test section up to film boiling conditions has been Syltherm 800. This

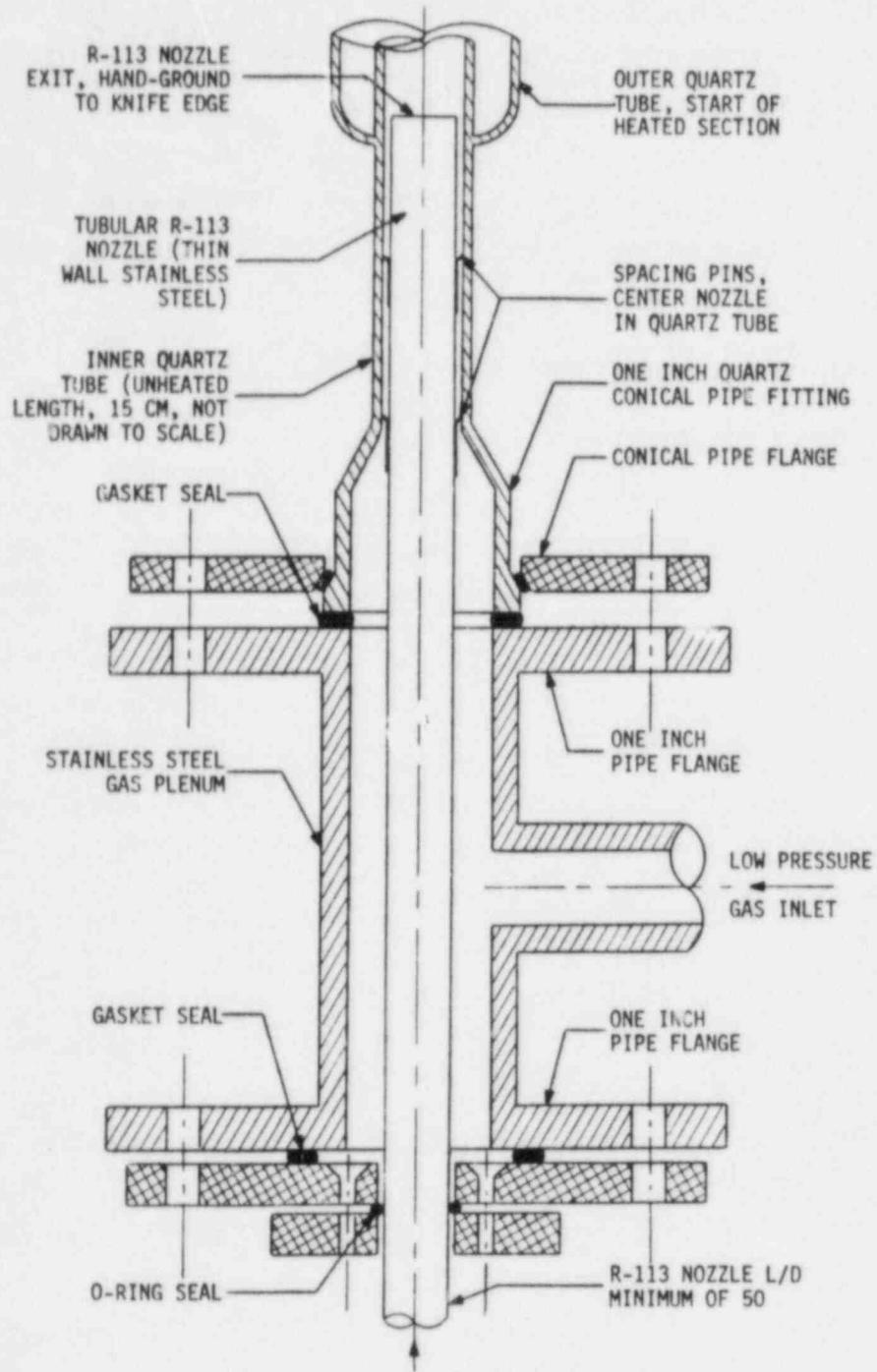


Fig. 9. Drawing of Test Section Inlet

trademarked product of Dow Corning (previously known as Q2-1162 heat transfer fluid) is a low viscosity, clear, straw colored, thermally stabilized silicone polymer, stable up to bulk temperatures of 400°C and film temperatures of 425°C. The long-term clarity of this fluid is such that detailed photographic observations of the flow field in the inner quartz tube of the test section can be made while this fluid is circulating through the annular gap between the coaxial quartz tubes of the test section.

The Syltherm 800 heating loop consists of a liquid expansion tank, 1 h.p. centrifugal pump, electric heaters (8.1 kW), throttling valves, a rotameter and various control valves and piping. The system is capable of heating the load of Syltherm (roughly 75 liters) up to 265°C or more, and can pump this fluid through the annular gap between the coaxial quartz tubes of the test section at flow rates up to 90 Lpm . Heat is supplied by a 4.5 kW circulation heater and by two 1.8 kW clam shell radiant heaters fixed to a 1 1/2 inch stainless steel pipe leading to the expansion tank inlet. These heaters are controlled by a proportioning controller (0.3 second cycle) monitoring the Syltherm 800 temperature leaving the test section, and by an over-temperature cut-off thermostat in case of controller failure. Given the large thermal mass of the system, the short cycle proportioning controller, and the 8.1 kW of power, temperature fluctuations at the point where the Syltherm 800 leaves the test section (i.e., test fluid inlet to test section) have generally been less than $\pm 1^\circ\text{C}$ during normal film boiling runs. Flow rate of the Syltherm 800 is controlled by three gate valves in combined series/parallel configuration, and is measured by an all metal rotameter with extension well and magnetic float follower, installed downstream of the test section. Accuracy of this rotameter is $\pm 10\%$, and space has been reserved for the installation of a more accurate turbine meter. A low flow cut-off switch on the rotameter shuts off the pump when flow of Syltherm 800 leaving the test section falls below 12 Lpm , to minimize the loss of Syltherm following a possible test section failure. Flow in the Syltherm loop is established by a 1 h.p. centrifugal pump, with a shaft seal cooling jacket. A flow switch in the cooling jacket water supply line shuts-off the pump at low cooling flows to prevent heat damage to the shaft seal. To accommodate fluid expansion during heating, the expansion tank ($\sim 0.08 \text{ m}^3$) is located at the highest point in the Syltherm loop, and is roughly half-filled with Syltherm 800. Above this level is a nitrogen blanket maintained at 60 kPa above atmosphere to prevent moisture or oxygen from

entering the system. This blanket is vented during initial start-up, to eliminate moisture, low pressure volatiles, etc., and again during each subsequent start-up to prevent over-pressurization as the blanket is heated by the Syltherm, and to vent dissolved nitrogen.

3. Test Liquid Delivery/Recovery System

For all trial runs to date, the test liquid used has been Trichlorotrifluoroethane (Freon-113, or R-113), chosen for its relatively low film boiling temperature, low chemical reactivity, relatively minor health hazards, and for its low vapor pressure at below-ambient temperatures (see operation of dump tank direct contact heat exchanger). The Freon-113 loop consists of a delivery tank ($\sim 2.3 \text{ m}^3$), a dump tank ($\sim 0.5 \text{ m}^3$), throttle valves, turbine meters, a magnetic drive centrifugal pump, Freon cooling bath coils, and various control valves and piping.

Prior to a set of test runs, a load of Freon-113 (typically 125 kg) is conditioned in the delivery tank for delivery to the test section. R-113 is degassed in the delivery tank by heating the fluid to approximately 60°C , using up to 600 watts of power through heating cables wrapped around the tank. This elevated temperature is held for several hours, with periodic venting to purge all dissolved gases. The R-113 is then cooled to the desired amount of subcooling by pumping it through coils submerged in a cooling bath maintained at roughly -25°C in a large chest-type freezer. The delivery tank load of Freon is then pressurized with a blanket of nitrogen or helium, and delivered to the test section. R-113 flow is controlled by needle valves, and is measured using one of three turbine meters, covering a range of flow rates from 0.05 lpm up to 20 lpm. Turbine meter output is read using a frequency/analog Vdc converter. From the test section exit, the R-113, along with any gases which may be injected into the test section, flows into the dump tank. This tank is partially filled with highly subcooled R-113, which has been circulated through the -25°C cooling bath coils also used to cool the delivery tank, and is maintained at atmospheric pressure, with direct venting to the outside air. Initial loading of the dump tank, prior to a series of test runs, was typically 200 kg. Temperatures as low as -15°C (a subcooling of more than 60°C) have been established in the dump tank. The heated R-113 (and gas) two-phase effluent from the test section enters the dump tank through a

tubular horizontal nozzle inserted 40 cm into the side of the tank, 10 cm above the bottom of the dump tank. A large number of small holes on the sides of this nozzle cause the effluent from the test section to enter the dump tank tangentially, assuring good mixing. In effect, the dump tank is a direct contact heat exchanger, cooling the heated R-113, condensing most of the R-113 vapor, and allowing the non-condensable gases to be vented to the outside. The dump tank has been more than 96% effective (less than 4% of the R-113 delivered to the test section has been lost, vented to the outside). R-113 temperatures at the test section inlet and outlet, turbine meter, dump tank and delivery tank are monitored.

After a day's runs are completed, a portion of the R-113 in the dump tank is returned to the delivery tank, to form a delivery tank loading large enough for the anticipated needs of the next day's runs. This transferred amount is measured by monitoring the liquid level in the dump tank using a liquid level gauge. Transfer is accomplished by depressurizing the delivery tank and either 1) pressurizing the dump tank with a N_2 or He blanket or 2) by using a magnetic drive centrifugal pump (the same pump used to pump R-113 from the delivery or dump tank through the cooling bath coils) to force liquid from the dump tank back into the delivery tank.

4. Gas Delivery System

Two different gas species have been introduced into the annular gap between the liquid Freon nozzles and the inner, heated quartz tube of the test section: nitrogen and helium. The gas delivery system consists of gas supply cylinders, a gas manifold/regulator, gas accumulator (0.5 m^3), throttle valves, rotameters, and various control valves and piping. The system is presently capable of using various compressed, non-condensable gases (N_2 , He, Ar, etc.), and with modifications, could deliver R-113 vapors. Non-condensables like nitrogen and helium are supplied in high pressure cylinders, and are reduced in pressure through the manifold/regulator, typically to 400-600 kPa, filling the accumulator. The accumulator damps-out variations in pressure and temperature as the gas is delivered from the manifold/regulator. From the accumulator, the gas flows through one of three rotameters, and into the test section. Flow rate is controlled by two needle valves. The three rotameters cover a range of 0.1 SLPM to 260 SLPM

(nitrogen). Temperature is monitored at the rotameter exits, and pressure is measured at the accumulator and at the rotameter exits, using Bourdon tube pressure gauges of ± 0.35 kPa accuracy.

5. Photographic Observation Apparatus

Photographic observation of the hydrodynamic behavior within the test section has been accomplished with both still photography and high speed motion pictures. Still photographs are taken with a 35 mm SLR camera, using 400 ASA B&W film. Lighting comes from either of two 3 μ s strobe lights each delivering a 0.5 w-s pulse of light. This short exposure time allows small (~ 0.1 mm) droplets traveling at high speeds (above 10 m/s) to be observed without significant image blurring due to object motion. The light from the strobes is bounced off white backgrounds and onto the test section. Each strobe/background unit is mounted on a frame which traverses the full heated length of the test section. One strobe/background is mounted behind the test section (as seen from the Lucite view port) to provide backlighting for the test section, while the other strobe/background is mounted to the side of the test section, to provide sidelighting. The still camera is mounted in front of the Lucite view port, on a frame which is tied to the motion of the strobe lights, and so traverses the full heated length of the test section in concert with the strobes.

Motion pictures of the flow field have been taken using several different cameras. Film speed has been 500 fps for most cases. The film used is Kodak VNX 430 (400 ASA color reversal film). Lighting is provided by four 450 W flood lights, directed on to the same background as is used by the strobe mounted behind the test section, to again provide backlighting to the flow field.

Opaque shields were placed near the test sections, to eliminate glare or "hot spots" resulting from light reflections. An additional opaque shield was placed between the two strobe/background units, to eliminate any back-lighting when only side lighting was desired.

Finally, a transparent ruler was fixed along side the test section, marked in one centimeter increments, with zero at the liquid nozzle exit. This ruler, seen in all photographs, gives ready reference to position along the test section, and is a secondary source of scale information (primary

information on scale comes from the outer quartz tube outer diameter, which is readily measured on each photograph).

B. Experimental Procedure

1. Equipment Calibrations

All three gas flowmeters were calibrated, at a minimum of six points, using nitrogen gas. For each calibration trial run, the low pressure gas accumulator was filled, and gas pressure and temperature in the accumulator were recorded. A constant flowrate through a given flowmeter was then maintained for a measured time interval, until gas expansion caused a temperature reduction of more than 2°C in the accumulator, or for a maximum of five minutes. After gas temperature returned to the initial value, final pressure in the accumulator was recorded, and the actual gas flowrate was calculated assuming ideal gas behavior. This was repeated at least four times at each calibration point, with more trials for results showing significant scatter. All flowrates were repeatable within $\pm 3\%$, with most settings repeatable within $\pm 1.5\%$. Flow rates for helium were calculated using ideal gas laws, assuming flowmeter dependency upon $\rho_G v_G^2$ (see Section C, Data Formulation).

The single turbine flowmeter used to date, in measuring R-113 flow rate, was calibrated with water, since turbine meter output is independent of fluid density, and viscosity-independent in the range of water and R-113 viscosities. The meter was calibrated at ten different flowrates, with each flow rate repeated at least three times. Flowrate was measured by using a balance scale and recording the time required to pass a given weight of water through the flowmeter. Flowrates were repeatable within 0.5% at the higher flowrates, and within 1% at the low end of the meter range.

Thermocouples were calibrated by the manufacturer to within $\pm 0.2^{\circ}\text{C}$, over the ranges of temperatures encountered in the experimental loop (-15°C to $+280^{\circ}\text{C}$). The pressure gauge used to measure outlet pressure at the gas rotameter's exits was calibrated using a 152 cm long mercury-filled manometer, with accuracy/repeatability of ± 0.35 kPa. Pressure drop between the gas rotameters and the start of the heated portion of the test section was measured using the same 152 cm mercury manometer (using the rotameter exit pressure taps and the pressure tap at the test section outlet). For the flowrates of

gas used in the trial runs to date, this pressure drop was found to be negligible (less than 0.5 kPa).

2. Optical/Photographic Determinations

To determine if the several curved surfaces and materials of differing refractive indices (the inner quartz tube, the annulus of Syltherm 800 heat transfer fluid, and the outer quartz tube) present along the light path between the two-phase flow field and the photographic equipment may cause significant distortion of the images being studied, photographs were taken of known-dimension objects placed within the inner quartz tube of a spare test section filled with Syltherm 800. These objects were moved radially within the inner quartz tube, perpendicular to the photographic line of sight, to study optical distortion both near the center of the test section and near the inner surface of the inner quartz tube. It was found that the images of the objects photographed (short lengths of wire with diameters of 254 μm , 457 μm and 787 μm) showed no measurable distortions over most of the volume within the inner quartz tube (within the limits of camera lens and film resolution). However, as objects move to within close proximity (less than 0.5 mm) of the inner quartz tube, along a radial path perpendicular to the line of sight through the center of the test section, distortion becomes significant, with images measurably shrinking. For all three wires placed within the test section, the gap between the wire and the quartz wall could not be observed, if it was less than roughly 0.25 mm. When the wire of 254 μm diameter actually was in contact with the wall, it could not be observed, while the wire of 457 μm could still be discerned when in contact with the quartz wall. Since these distortions occur within only a very limited volume within the test section (within 0.5 mm distance to the quartz tube wall, and only then when nearly at right angles to the center line and the line of sight) no corrections were made to measurements taken from photographs. Of course, no distortions are possible along the axial direction of the test section, since there are no curved surfaces in the plane defined by the line of sight and the test section axis.

From preliminary tests of film boiling within the test section, it was determined that much of the hydrodynamic behavior could not be properly observed if less than a 30 cm length of the test section was captured on a

photographic frame. Accordingly, the frame holding the camera in front of the test section (allowing camera and lighting to traverse the full heated length of the test section in concert) was positioned so as to place the film plane of the SLR used 63 cm from the test section centerline. With a 55 mm lens, this projects an image of 30 cm onto the long axis of 35 mm film. With the strobe lighting and ASA 400 film used, proper exposure required F 5.6 apertures. For the 55 mm lens, and the film plane/object distance of 63 cm, this resulted in a depth of field of 35 mm, so that all of the test section could be seen in sharp focus. Using longer focal length lenses to study the flow field in greater detail results in decreased depths of field: for a 105 mm lens, only a 10 mm depth of the flow field can be seen in sharp focus (total flow field depth is 13.6 mm); for a 200 mm lens, only a 2.5 mm depth of the flow field is in focus.

For the above photographic parameters, image resolution is approximately 100 μm when using a 55 mm lens. However, when photographing small transparent droplets, strong backlighting can "wash-out" droplets similar in size to the lower limits of image resolution, making them difficult to discern. For this reason, side lighting is desirable if one wishes to observe small droplets. Using lenses of increased focal length improves image resolution accordingly, so that for the above photographic parameters, use of a 105 mm lens results in image resolution down to roughly 50 μm , and use of a 200 mm lens can give resolution down to roughly 25 μm .

3. Alignment of Test Section

The quartz test section is supported in place by the two flanged pipe connections to the Syltherm 800 heat transfer fluid supply system. These flanged connections are in turn rigidly clamped in place, with their flanged faces and openings positioned to mate exactly with the quartz pipe connections of the test section, to minimize stresses transmitted through the connections. Stress is further minimized by the use of silicon rubber gaskets 3.2 mm thick for these connections (to tube quartz conical pipe connectors fused to the side of the outer quartz), since these gaskets are quite compressible. The frame supporting these pipe flange connections can then be adjusted, so that the test section itself is exactly vertical.

Coaxial alignment of the liquid inlet nozzles within the inner quartz tube of the test section is determined by placing the nozzles inside the quartz tubing, and then slowly rotating the nozzle. Any wobble observed during this rotation, or any looseness in fit, is corrected by adjusting the heights of the six spacing pins soldered about the circumference of the nozzle at two axial locations. These pins project away from the nozzle side at a very shallow angle, so that as cantilevered beams, they flex slightly (to keep from stressing the inner quartz tube unduly) and can be rebent slightly to facilitate the adjustment of their heights.

The liquid nozzle axial position within the test section is then adjusted, so that the nozzle outlet extends 1-2 cm up into the heated portion of the test section. This position reduces the amount of heat conducted into the walls of the nozzle from the heated quartz wall, and so minimizes the amount of temperature rise in the R-113 as it flows through the nozzle, prior to its injection into the inner quartz tube. This position also reduces the amount of R-113 which can fall downward through the annular gap between the nozzle and the inner quartz tube and into the gas inlet plenum. Nozzle axial positioning is accomplished by loosening the O-ring seal where the nozzle passes through the bottom flange of the gas inlet plenum, and sliding the nozzle up or down. See Fig. 9 for inlet plenum geometry.

Finally, the flanged pipe connections to the quartz conical pipe connectors fused to both ends of the inner quartz tube of the test section (see Fig. 8) are aligned by first adjusting the four point spring suspension system of each flange connection, so that these pipe flanges are properly oriented in line with the test section. These springs prevent any axial loading of the test section due to the weight of inlet/outlet piping. Guide rods are then placed against the sides of the piping connected directly to these pipe flanges, so that the flanged connections can only move in the direction of the test section axis. These guide rods prevent any transverse loading of the test section, by eliminating the possibility of any transverse motion in the inlet/outlet piping.

4. Test Runs

The procedures followed to perform series of experimental runs are described in the following paragraphs. In general, five to 15 trials, each

with different inlet gas and liquid flowrates, but with fixed inlet void fraction (gas species), and liquid subcooling, could be performed during a full day of experimentation. Pressure at the test section inlet could not be controlled, and typically varied between 106 kPa and 130 kPa (absolute), due to two-phase flow friction losses between the test section inlet and the dump tank, and due to varying hydraulic head in the dump tank (see Fig. 5). Table IV summarizes the inlet flow parameter ranges studied to date.

Table IV. Flow Parameters Studied to Date (Inlet Conditions)

<u>Test Series</u>	<u>D_o, Inner Quartz Tube ID (cm)</u>	<u>D_j, Liquid Nozzle ID (cm)</u>	<u>Void Fraction</u>	<u>v_F (cm/s)</u>	<u>v_G (cm/s)</u>	<u>T_E (°C)</u>	<u>Gas Species</u>
1-60	1.36	0.902	0.56	4.4-43.4	41.0-490.	23-27	Nitrogen
201-452	1.36	1.08	0.37	3.2-31.2	1.7-448.	14-41	Nitrogen
700-731	1.36	1.08	0.37	3.2-20.6	4.1-243.	24-25	Helium

The following steps were taken in order to perform a series of experimental trials:

a) On the day prior to a day of experimental runs, a load of R-113 was loaded into the Freon delivery tank (for degassing and establishment of desired subcooling). The heating cables encircling this tank would then be energized (total power a maximum of 600 watts) and the Freon transfer pump was turned on, to thoroughly mix and circulate R-113 within the delivery tank. Once the load of R-113 was heated to a minimum of 55°C (atmospheric boiling point for R-113 is 47.7°C), the delivery tank would be periodically vented, to purge the R-113 of any noncondensable gases. To further this, R-113 from the delivery tank would periodically be circulated through the cooling bath coils, to assure that any R-113 in these cooling lines was also thoroughly degassed. This periodic venting would be continued until the pressure in the delivery tank (at a minimum of 55°C) was equal to the vapor pressure of R-113 at the temperature maintained in the tank (pressure was measured to within

± 1.7 kPa, using a Bourden tube gauge). At this point, the R-113 was assumed to be thoroughly degassed.

Once the R-113 load in the delivery tank was degassed, it was brought down in temperature to the desired amount of subcooling. For relatively minor subcooling (temperatures above room temperature), the power to the heating cables was merely reduced until this subcooling was obtained. For greater subcooling (temperatures near or below room temperature), the R-113 load was circulated through the cooling bath coils until the desired amount of subcooling was reached.

For the subcooled R-113, subatmospheric pressures were maintained in the delivery tank until the actual time when R-113 was to be introduced into the heated test section. At that time, a blanket of N_2 or He was introduced into the delivery tank, at a pressure of roughly 270 kPa (absolute), to provide a driving force for delivery of R-113 into the test section. This minimized the amount of noncondensable gas which could be reabsorbed by the Freon.

b) Prior to energizing of the Syltherm 800 heaters, a check was made of the test section and attendant lighting. The gasketed connections to the Syltherm supply loop were checked for leaks (expansion/contraction during loop warm-up and coast-down loosens the connecting bolts, and the silicon rubber gaskets degrade in the presence of Syltherm 800, particularly at higher temperatures), and the connecting bolts would be tightened in an effort to stem any leaks observed. If leaks could not be eliminated, the gaskets would have to be replaced, postponing any experimentation.

Flood lighting would then be adjusted to provide backlighting for the region of the test section to be photographed by motion pictures (unlike the strobe lighting used for still photographs, the flood lights could not be remotely moved up and down along the full length of the test section).

These adjustments were made prior to start-up of the Syltherm loop, since work on or around the test section could be hazardous if hot heat transfer fluid was circulating through the easily broken quartz test section.

c) The Syltherm 800 heat transfer fluid loop was then energized. Flow was first established by powering the centrifugal circulation pump (first opening the water cooling lines to the pump seal cooling jacket). Then the 8.1 kW of electric heating was energized, setting the proportioning controller

to the desired operating temperature (usually 265°C-270°C) and setting the high-temperature cut-off thermostat to 300°C.

Given the mass of Syltherm 800 and the attendant piping to be heated, the heating of the heat transfer loop requires at least 150 minutes (for a temperature rise from room temperature to 265°C). During this warm-up time, the gas blanket of the Syltherm expansion tank was continually vented (at a low flow rate, with fresh N₂ supplied to maintain the desired blanket pressure of 140 kPa absolute) to purge any contaminants absorbed by the Syltherm, and to prevent over-pressurization as the gas blanket warms to operating temperature.

d) Once the delivery tank load of R-113 was brought to the desired amount of subcooling, the tank was isolated from the Freon circulating pump and cooling bath coils. Then, this pump was used to circulate the dump tank load of R-113 (used in direct contact heat transfer to recover R-113 heated or vaporized in passing through the test section) through the cooling bath coils. The load of R-113 in the dump tank (typically 200 kg prior to experimental runs) could be cooled from near room temperature down to -10°C or -15°C in approximately 60 minutes. Stratification within the dump tank was prevented by periodically injecting short bursts of N₂ or He into the bottom of the dump tank, causing a great deal of agitation.

The circulation of R-113 from the dump tank through the cooling bath coils was continued until the series to experimental trials were completed. Because of this, temperatures in the dump tank rarely exceeded 0°C during a day of experimentation, even when a flow of R-113 through the test section was maintained for a long continual period (usually R-113 flow through the test section was maintained for only 3-8 minutes during a given trial run, see following procedures).

e) Ambient air pressure was measured, using a mercury barometer. This pressure reading was used to correct the absolute pressure gauge used to measure pressure at the gas flowmeters.

f) The high pressure gas supply manifold was opened, allowing low pressure gas (N₂ or He in all trials to date) to fill the gas accumulator tank to the desired pressure (usually 440-640 kPa absolute). Temperature in the tank would normally stabilize (near room temperature) within 30 minutes, and

for the relatively low gas flow rates studied to date, seldom fluctuated during experimental trials.

g) When Syltherm 800 temperature reached the desired 265-270°C range, flow of Syltherm through the test section was set in the range of 60-85 gpm (with the higher flow rates for trial runs where wall rewetting tendencies were anticipated; i.e., for greater degrees of subcooling, larger R-113 flow-rates, etc., see discussion of experimental results).

h) The R-113 delivery tank was then pressurized with a flow-driving blanket of N_2 or He.

i) The R-113 delivery line from the delivery tank to the test section was then purged. This was accomplished by bypassing the R-113 flowmeter, and allowing a high R-113 flowrate to flow through the test section (flowrate estimated, roughly, at 20 gpm , beyond the safe operating range to the R-113 turbine meter used in trials to date). This high flowrate forced any gas bubbles out of the line (hydraulic "hammer" caused by two-phase flow moving through a turbine meter can cause meter damage) and to warm or cool the insulated R-113 delivery lines to the delivery tank subcooling.

The experimental facility was then ready for the performance of a series of trial runs.

j) A gas flowrate greater than that desired for the given trial run was introduced into the test section. This flow was used to prevent any wall wetting when the R-113 is first introduced into the "dry" test section, and to prevent the flow of any R-113 downward, through the annular gap between the R-113 nozzle and the heated quartz tube wall.

k) The R-113 flowrate desired for the given trial run was established, by adjusting a needle valve downstream of the R-113 turbine flowmeter. In this manner, R-113 pressure at the flowmeter is roughly the same as that in the delivery tank, so that if any blanket gas has been absorbed into the R-113, it cannot leave solution (causing bubbles or gas slugs), due to depressurization, until after passing through the flowrate controlling needle valve.

l) The gas flowrate desired for the given trial run was then established, by adjusting a needle valve upstream of the gas flowmeters. In this manner, gas pressure at the outlet of the gas flowmeters is in direct

communication with the pressure at the start of the heated portion of the test section. As discussed in the section dealing with gas and delivery system calibration, for the flowrates of gas used to date the pressure drop between gas flowmeter outlet and heated portion of the test section is negligible (less than 0.5 kPa). Because of this, the pressure measurement at the gas flowmeter exit reflects the pressure at the heated test section inlet, simplifying volumetric flowrate calculations for the gas flow.

m) Visual observation of the flow field in the test section was then made. Once this flow field stabilized (requiring significant time when a very low liquid flowrate was introduced into the dry test section), photographic observations of the flow field were made. For each set of flow parameters (for each trial run) a series of still photographs were first taken, using a 55 mm lens which captured 30 cm of the test section length on each 35 mm film frame. These photos were taken at five or six locations, covering the full test section heated length. At each position, two to five photographs were taken, for a total of 16-20 frames. Either back or side strobe lighting was used. Additional still photographs, using 105 mm or 200 mm lenses, for more detailed flow field structure observation, were taken for selected trial runs. Similarly, high speed motion pictures were taken of portions of the test section (15 or 30 cm of the test section length), for selected trial runs.

n) Freon temperature at the liquid nozzle inlet, and temperature and pressure at the gas flowmeters outlet were recorded, as were R-113 turbine meter output and gas flowmeter indicated flowrate, for each trial run. In addition, Syltherm 800 temperatures at test section inlet, and two-phase test section effluent, R-113 delivery tank, and R-113 dump tank temperatures were monitored periodically, as were Syltherm 800 flowrate and dump tank liquid level, to verify proper test loop operation.

o) Once all observations/data recording were accomplished for a given trial run, R-113 flow into the test section was terminated. Then a momentary high gas flux (up to 40 Lpm for N_2 , 100 Lpm for He) was introduced into the test section, to purge the heated test section and the inlet gas plenum of R-113, thereby "drying" the test section. The test section was then ready for a new trial run, with new inlet flow parameters.

To perform a new trial run, steps j) through n) (above) were then repeated. This process was continued until the series of trials planned for a given day of experimentation were performed, or until the amount of R-113 in the delivery tank was nearly exhausted (this was monitored by observing the liquid level in the dump tank, with estimates of remaining delivery tank loading made deliberately conservative, so that experimentation was terminated well before any of the emptying delivery tank blanket gas could be passed through the R-113 turbine meter and potentially cause damage). In addition, experimentation was terminated whenever significant blanket gas absorption occurred in the delivery tank R-113, as evidenced by gas bubbles or slugs evolving in the liquid inlet nozzle.

Liquid flowrates studied to date have only been limited by the liquid turbine meter used to date. Liquid subcooling studied to date has been limited to relatively large values by rapid gas blanket absorption, with subsequent gas bubble evolution downstream of test section inlet, for subcooling of less than 10°C (for R-113 temperatures of more than roughly 38°C). Low gas flowrates studied to date have been limited by the development of significant wall rewetting for large amounts of R-113 subcooling, high liquid flowrates, or large inlet void fractions (with attendant large radial accelerations as the liquid inlet jet expands due to gravity deceleration) when the gas flowrate is reduced beyond a certain value.

When changing from one gas species to another, for injection into the test section inlet, the gas accumulator tank was first purged. This is accomplished by first filling the tank to 550 kPa, then venting, and finally drawing accumulator pressure down to 7 kPa (absolute) (using a vacuum pump) repeatedly, using the new gas species.

C. Data Formulation

From temperature and pressure data, fluid properties were evaluated (see Refs. [50-53]). The gas densities calculated (using ideal gas law) were then used to correct the gas flowmeter indicated flowrates, since they indicate equivalency to nitrogen flows at STP. For the gas flow conditions used, these flowmeters were immune to any changes in gas viscosity. The flowrate correction equation, as given in the Brooks Technical Bulletin No. T-022 [54], is as follows

$$W_{G,M} = W_{G,ind.} \cdot \sqrt{\rho(N_2,STP)/\rho_{G,M}} \quad (8)$$

where $W_{G,M}$ is actual volumetric flowrate at the meter, $W_{G,ind.}$ is the flowrate indicated at the meter, $\rho(N_2,STP)$ is nitrogen density at 21°C and 1 atm, and $\rho_{G,M}$ is actual gas density at the meter. As previously noted, for the gas flowrates used to date, pressure drop between gas meter exit and heated test section inlet is negligible, so that no further correction was required to calculate volumetric flowrate at the start of the heated portion of the test section. If pressure drop was significant, one would merely have to use a mass flow balance, given gas densities at flowmeter and heated inlet, to find volumetric flowrate.

IV. ANALYSIS OF RESULTS

In this section, results of the experimental investigation are presented and discussed. Given the relative complexity of the flow fields we have observed, much of this section consists of still photographs of flow patterns resulting from various inlet flow conditions, with accompanying discussion.

A. Analysis of Photographic Information

Still photographs taken with 35 mm B&W film were first analyzed by placing the developed negatives on a light table fitted with a binocular microscope. Viewed in this manner, general flow field observations could be made quite easily. Intact liquid core length, length of agitated core region, length of large liquid slugs, and core surface wavelengths could be measured directly, by using the image of the transparent ruler mounted alongside the test section as a reference. More detailed measurements were made from the still photograph negatives by projecting the images they contained onto a viewing screen, with a minimum negative-to-screen image magnification of 50. For negatives taken while using the 55 mm SLR lens, this magnification allowed measurement of droplet diameters down to 100-200 μm (real particle size), given favorable lighting (small droplets "wash out" with strong back-lighting). Use of greater projection magnification, or larger focal length lenses, allows for the measurement of smaller droplets. Measurements taken from a projected image can be made quite rapidly, although more precise measurements can be taken by using a micrometer reticle in conjunction with the binocular microscope of the light table.

Motion pictures taken of the test section flow field were analyzed on a motion picture analyzer, with x-y plotting cross hairs and film projection speeds from 48 fps down to zero.

B. General Flow Field Observations

The flow patterns evolving downstream of the heated test section inlet, as the injected R-113 jet, surrounded by a gas annulus, becomes unstable, first with a significant surface roughening, and further downstream disintegrating into large slugs and drops (inverted annular flow leading to inverted slug or churn flow) and/or into small droplets (dispersed droplet flow) (see Fig. 1) are quite complicated. However, the dominant mechanisms controlling the destabilization/break-up of the inlet liquid core are quite similar to those identified in the previous adiabatic simulation of inverted annular flow hydrodynamics [9,39-42]. The results of this adiabatic study, therefore, are reviewed in the following section.

1. Review of Adiabatic Inverted Annular Flow Study Results

For the adiabatic simulation of inverted annular flow, utilizing coaxial cylindrical water jets and annular gas jets, three different mechanisms contributing to liquid core destabilization were noted. For low gas/liquid interface relative velocities, the formation of varicose waves (alternating pinching and expansion of the liquid jet) resulting in the formation of large liquid slugs (which, if spherical, would have diameters roughly twice that of the original liquid jet) well downstream of the jet nozzle outlet. At moderate gas/liquid interface relative velocities or at denser gas flows, the liquid jet was distorted into a sinuous form, again breaking up into large slugs well downstream. Intact liquid jet lengths decrease with increasing gas density and relative velocities, as do sinuous wavelengths (and attendant liquid slugs). The varicose or sinuous break-up mechanisms are the same as the classical jet instabilities long recognized in the study of low velocity (nonatomizing) free liquid jets.

At still higher relative velocities or gas densities, large numbers of roll waves were observed to form near the liquid jet nozzle exit. Entrainment of small droplets (typically maximum diameter of 400-600 μm , most much smaller) from the roll wave crests created dispersed flow downstream of liquid

jet core break-up. The growth of the roll waves to large amplitude and volume, coupled with the acceleration of the liquid in these roll waves to velocities far exceeding the initial liquid velocity, resulted in a large reduction in the amount of liquid remaining in the liquid core jet. Subsequent break-up of these large amplitude/volume roll waves and reduced-diameter liquid core jet remnants could not be observed, due to wall wetting in this adiabatic experiment. However, observation of the dispersed droplet flow at the test section outlet revealed droplet sizes ranging up to 2 to 4 mm, with most of the droplets in the sub-400 μm size group to be expected of roll wave entrainment. The larger droplets can be explained as the maximum stable drop size in churn-turbulent flow, or as the drops resulting from varicose/sinuuous break-up of reduced diameter liquid core remnants on the order of 1-2 mm diameter.

For all break-up mechanisms observed, increased liquid velocity resulted in longer intact liquid core length while increased gas velocities (beyond the bulk liquid velocity) and gas densities resulted in less stable liquid cores.

2. Hydrodynamic Behavior Observed in Present Diabatic Study

In the present film boiling experiment, the disintegration of the liquid, jet-like core of inverted annular flow into inverted slug/churn flow or dispersed droplet flow is somewhat more complicated and violent than was observed in the previous adiabatic study. However, roll wave entrainment and jet instability are still the two predominant mechanisms for the break-up of this liquid core.

a) Inverted Annular Flow: Starting at the liquid nozzle exit into the heated portion of the test section, the following hydrodynamic behavior has been observed. Since flow is upward, and since only low liquid inlet velocities (3-43 cm/s) have been utilized, as the jet issues from the nozzle exit, jet expansion due to gravity deceleration occurs. This, of course, is most significant for lower liquid velocities, higher inlet void fractions (larger gap between liquid jet and heated wall), and for lower inlet gas velocities, where there is less interfacial shear to accelerate the liquid upward. For the test trials using an inlet void fraction of 0.56, the attendant radial acceleration of the jet liquid as it expanded was such that extensive wall rewetting would occur for minimal gas inlet flows. In actual film

boiling, where liquid originally occupying the whole flow area is ultimately forced away from the heated wall beyond the CHF point, this jet expansion region would not be present.

Beyond the point of initial jet expansion, a relatively smooth, stable liquid core could be observed. The R-113/heated wall annular gap was only observable for brief intervals, indicating a gap of roughly less than 250 μm (see Experimental Procedure, Optical Determinations) over most of this stable region. For initial void fraction of 0.56, this stable region was quite small, due either to disturbances caused by radial expansion or due to the larger gas inlet velocities utilized. For initial void fraction of 0.37, however, this stable region could be quite long, for minimal inlet gas velocity. Increased inlet liquid velocities in general resulted in longer stable, smooth liquid cores. Decreased inlet gas velocities, and minimal gas heating/expansion and vapor generation downstream of the inlet, due to the effect of increased liquid subcooling, also result in longer stable inverted annular flow liquid cores. This stabilizing effect of liquid subcooling was negated when sufficient subcooling lead to extensive wall rewetting and attendant vapor generation. However, small patches of rewetting seemed to have no great effect on liquid core stability.

b) Agitated Region: Increased gas annulus velocities, due either to increased gas flowrates at the test section inlet or due to vapor generation and gas expansion due to heating as one moves further downstream of the heated inlet (see stabilizing effect of high subcooling), eventually cause the growth of disturbances on the surface of this smooth liquid core. These disturbances first result in the formation of roll waves, with wavelengths of roughly 10 mm (order of magnitude). One can observe small droplets being sheared from the crests of these roll waves. As these disturbances progress downstream, the core becomes quite agitated, with a fine interfacial structure beyond the lens/film resolution limits of our photographic equipment (structure finer than 25-50 μm). The large interfacial area generated in this region indicates large heat and momentum transfer rates. Liquid/heated wall proximity is continuously maintained, with no visible gap. From the downstream edge of this agitated region, a stream of fine droplets can be observed.

The mechanisms of this agitated region appear to be the following. As the roll wave disturbances grow in amplitude and volume, their large

surface area per volume results in their rapid acceleration by the gas annulus stream. As a result, liquid is pulled away from the liquid core, as was observed in the previous adiabatic simulation [9,39-42]. This accelerated liquid, as sheet-like expanded and distorted roll waves and as droplets sheared from roll wave crests, forms a thin, highly agitated annulus of liquid in close proximity to the heated wall. As this agitated annular structure moves downstream, it depleats the liquid core, reducing it in diameter, while itself losing mass, from evaporation and from droplets shearing-off and accelerating downstream faster than the bulk of the agitated region. When this liquid which has been formed and ejected from the agitated region has progressed downstream far from its point of original occurrence, it becomes less coherent. Gaps can be seen in the once-uniform sheet, and is not in continual, close proximity of the heated wall. Eventually this annular sheet of liquid degrades into droplets and small (less than 500 μm) ligaments.

Near its point of original formation, this agitated region appears to be quite solid, since a near-intact liquid core still fills the center of the test section. At the leading (i.e. downstream) edge of the agitated region, however, one can see a smooth, reduced diameter remnant of the original liquid core in the center of the test section, with the thinned edges of the agitated region surrounding it. As the liquid sheet from the agitated region accelerates and moves downstream, motion pictures show it passing over, and apparently leaving undisturbed, slower moving reduced diameter smooth liquid core jet remnants. Well downstream, when this agitated liquid sheet and droplets has lost much of its mass, one can see these same core jet remnants through gaps in the agitated annular liquid sheet.

Given the process of roll wave growth (a finite number of relatively large waves), formation of a skirt-like annular sheet from the extreme growth and distortion of these roll waves, and subsequent acceleration of this agitated sheet and cloud of droplets, the agitated region of the flow field is not very stable, particularly for low liquid and gas inlet flowrates. Under these low flow conditions, the agitated region gradually builds up, extending up to 10 to 30 cm in length. It then rapidly expels a large agitated sheet and cloud of droplets, leaving behind a much smaller agitated region and depleted liquid core, the latter often falling back down into the agitated region in the wake of the fast moving sheet/droplets. This quasi-periodic

chugging behavior and the length extents of the agitated region are lessened by increased liquid flow (less drastic liquid core depletion in the wake of annular agitated sheet acceleration/ejection) and are also lessened by increased gas inlet flow (a more continuous formation of roll waves, and a more continuous ejection of annular agitated sheets/droplets).

At very high inlet gas flowrates, the agitated region is drastically reduced, as roll-wave entrainment disintegrates the liquid core rapidly, into dispersed droplets near the liquid nozzle exit. Similarly, at high liquid flow rates, the significance of the agitated is drastically reduced, as the agitated region is not able to grow and deplete much of the faster-moving liquid core before it, still moving with the bulk of the liquid, passes out of the heated portion of the test section. For these higher liquid flows, most of the liquid core instability is due to varicose/sinuuous deformation of the liquid core, with small agitated regions or merely isolated roll waves appearing at the sinuous or varicose wave crests.

c) Inverted Slug/Churn Flow: Downstream of the agitated region, remnants of the original liquid core jet are still present. For low inlet gas and liquid flow conditions, where violent chugging occurs, the core liquid may be reduced to a few 1-2 mm diameter ligaments only a few centimeters long rather than a single coherent jet. Through varicose/sinuuous jet instability, they disintegrate into drops of up to 3 mm diameter. With less core mass depletion, the core remnants become larger multiple ligaments. Finally, with substantially reduced agitated region and attendant core mass depletion, (see previous paragraphs) a coherent liquid core still emerges downstream of the agitated region. Again, jet instabilities cause the break-up of this core remnant. But the resulting liquid slugs are too large to be stable in the churn-turbulent flow field downstream of the original inverted annular flow. The slugs are deformed into multiple ligaments (where jet instabilities can now form stable droplets up to roughly 3 mm), or roll waves form as the slugs or precursor varicose/sinuuous wave crests approach the heated wall, causing secondary roll wave entrainment and/or formation of agitated liquid sheets. For low liquid flowrates, no droplets larger than 3 mm are observed. For higher liquid flowrates, larger droplets are observed, but they are highly distorted (rather than true spheres), indicating that they are unstable and would eventually break-up in a longer test section.

While these liquid core remnants are forming into droplets and unstable liquid slugs, moving at relatively low velocities (on the order of original liquid inlet velocity), the agitated annular film/dense droplet sheets generated in the agitated region are continually sweeping past them. From analysis of motion pictures, there appears to be little interaction between these two sets of liquid masses. The reduced core remnants remain near the center of the test section, while the agitated sheets occupy only a very thin annular area in close proximity to the heated quartz wall.

As previously discussed, well downstream of the agitated region, the ejected liquid film/dense droplet sheets become depleted in mass, losing their coherency. Gaps can be seen in the once uniform sheet, and as the liquid moves away from close proximity to the heated wall, its surface structure becomes less agitated. Eventually, the annular sheet of liquid degrades into a low-density cloud of droplets and small (less than 500 μm) ligaments.

d) Dispersed Flow: While droplets resulting from the break-up of liquid core remnants in the range of roughly 0.6 mm to 3 mm diameter, along with larger, distorted slugs, may constitute most of the liquid mass well downstream of the original inverted annular flow, most of the liquid surface area comes from the smaller droplets formed by roll wave entrainment, and within the agitated region and its attendant agitated sheet/dense droplet cloud annular sheet which is ejected and propagates downstream. Largest droplets observed generated at these sites are in the range of 400-600 μm . Given our knowledge of roll wave entrainment in annular flow (Kataoka et al. [55]), one can assume that most of the droplets generated at roll wave crests are in the sub-200 μm range. Similarly, given the very fine agitated structure of the agitated region (less than 25-50 μm), one can assume that a predominance of the droplets generated in the agitated region will be in the sub-50 μm range. For droplets this small it is difficult to obtain good photographic images. Most of these droplets are beyond the resolution capabilities of our equipment. And, with strong backlighting, most are not discernible. Furthermore, most are generated in close proximity to the inner quartz tube wall, with optical distortions along the radial line perpendicular to the line of sight (i.e. the sides of the inner quartz tube visible as lines from the point of photographic observation). Yet it is at these far edges of our view of the flow field that our view of these droplets is least obstructed by the bulk of

the liquid filling the test section. Finally, for small droplets generated in close proximity to the heated wall, vaporization must be extremely rapid, so these droplets rapidly diminish in size.

Near the test section exit, the flow field is dispersed droplet for all but the highest liquid flowrates, when distorted liquid slugs may be present. For the lowest gas and liquid inlet flowrates, only very small droplets were present at the exit, due to the limited liquid supply and resulting core depletion in the agitated region and due to the low gas fluxes and attendant drag forces available to lift droplets through the test section. For increased gas fluxes, either due to increased inlet gas flowrates, or due to decreased liquid subcooling (less heat absorbed by the liquid, more heat used to form vapor and to heat/expand gas), larger droplets and more liquid mass appear at the test section exit. Similarly, for larger inlet liquid flowrates, larger droplets, and more liquid mass in general, are present at the exit (one meter from the heated inlet, for all trials to date). For high liquid and gas flowrates, many of the larger liquid masses at the exit are highly distorted, indicating that they are still in the process of disintegrating into smaller, stable droplets.

In Fig. 10, a flowchart is given which generalizes the flow fields and liquid core break-up mechanisms observed within the experimental test section, as inverted annular flow leads to downstream agitated flow, inverted slug/churn flow and ultimately dispersed droplet flow.

C. Discussion of Specific Flow Field Photographs

Given the quite complicated flow field observations detailed in the previous section, a limited number of photographic illustrations cannot demonstrate all the behavior of interest. In addition, phenomena associated with the agitated region in particular differ greatly for variation in inlet flow parameters, and indeed seem to vary from one photographic frame to another for a given set of flow conditions. Therefore, in this section, a large number of photographic figures are presented and discussed. The order in which these figures are presented is such that a sequential series of figures demonstrate the effects of variation of a single inlet flow parameter (inlet void fraction, gas flowrate, liquid flowrate, liquid subcooling, or gas inlet density). In addition, figures near the end of the series give more detailed

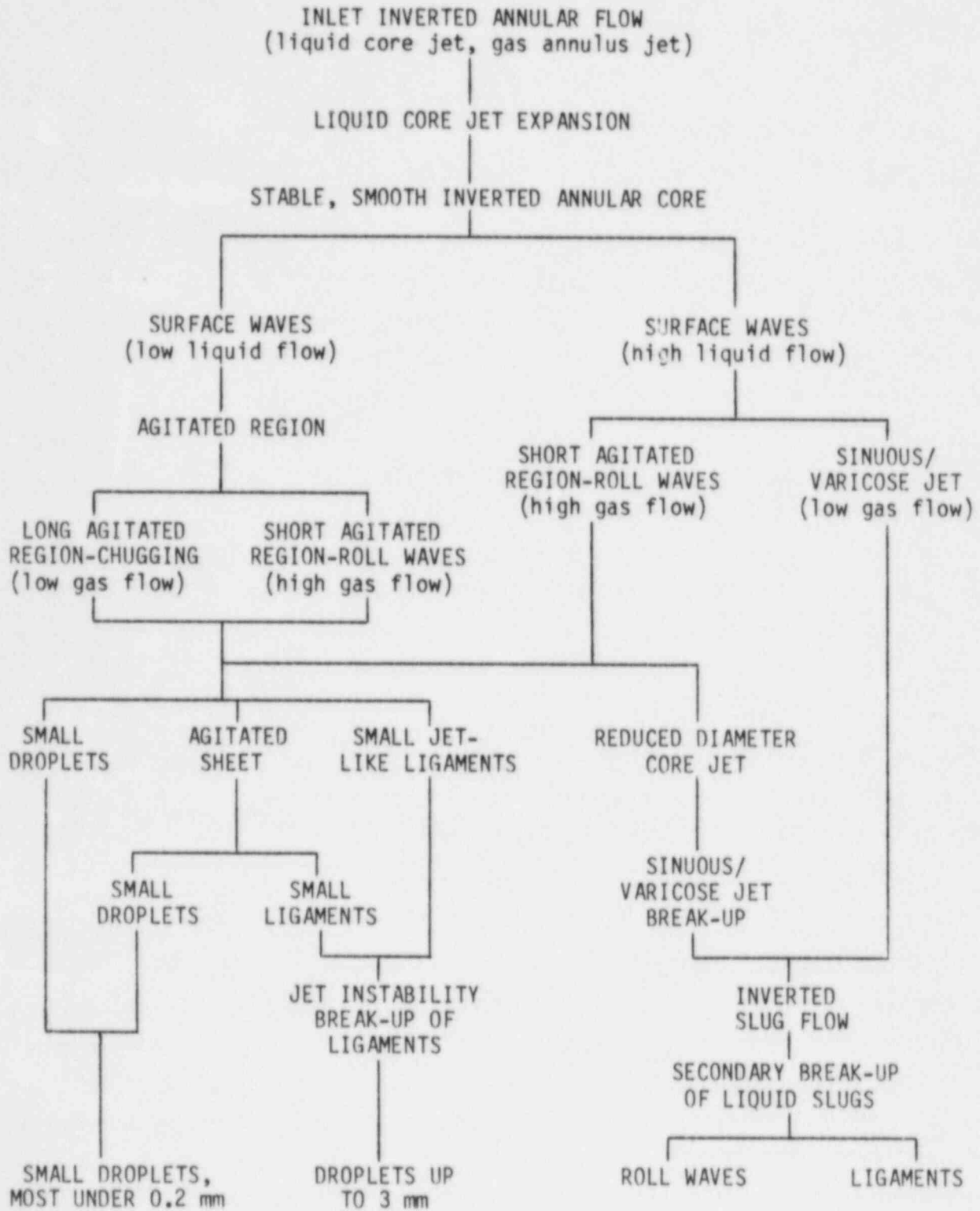


Fig. 10. Downstream Transitions From Inverted Annular Flow

views of flow field structure. Table V summarizes flow parameters relevant to each figure in the photographic series.

The following paragraphs discuss the flow field information contained in each of the figures. Note that the scale along the side of each photograph indicates distance, in cm, from the liquid nozzle exit into the heated portion of the test section.

1. Figures 11 and 12: High Inlet Void Fraction

For Figs. 11 and 12, inlet void fraction is 0.56, and even for the high inlet liquid flow rates used, jet expansion is significant. In Fig. 11, the low inlet gas velocity results in a relatively small agitated region (due to large v_F) and only moderate reduction. Thinning agitated sheets can be seen enveloping the liquid core (at 35 and 65 cm), with a cloud of droplets streaming from their downstream edges. Near the test section exit, jet instabilities are causing expansion/contraction of the reduced liquid core, inducing secondary break-up where the core mass approaches the heated wall. In Fig. 12, very high inlet v_G causes rapid core break-up due to roll wave entrainment, before an agitated region can form. The high density, agitated dispersed flow results in violent droplet impingement against the heated wall, causing wall rewetting in the region from 3 to 17 cm downstream of nozzle exit. This wall rewetting changes the optical properties at the inner wall of the inner quartz tube, so that the heavy dark line seen when the inner tube wall is dry vanishes after rewetting.

2. Figures 13 and 14: Low Inlet Void Fraction

In Figs. 13 and 14 (all subsequent figures through Fig. 30), the void fraction at the inlet is 0.37. Compared with Fig. 11, the jet expansion is substantially reduced, even though lower inlet v_F are utilized in Figs. 13 and 14 (15.6 cm/s compared to 43.4 cm/s). In Fig. 13, the low inlet v_G results in a very stable, smooth inverted annular core, with significant surface disturbances only appearing more than 40 cm downstream of the nozzle exit. A small rewetting patch at 18 cm is generating very little vapor, given the long term stability of the core. Small agitated regions starting at 50 cm and propagating downstream with a slight chugging effect (reduced in importance by the still appreciable inlet v_G , compared to the following figures) result in small agitated sheets, smooth reduced core remnants, and fine droplets.

Table V. Inlet Flow Parameters for Figures in Flow Field Photographic Series

Fig. No.	Trial No.	D_J (cm)	α	v_G (cm/s)	v_F (cm/s)	T_E (°C)	Gas Species	Comments
11	7	0.902	0.56	71.6	43.4	23	N ₂	High inlet void, Jet expansion, Wall rewetting
12	11	0.902	0.56	154.	43.4	23	N ₂	
13	204	1.08	0.37	1.7	15.6	26	N ₂	Low inlet void, Stable core at low v_G , Effect of increased v_G
14	210	1.08	0.37	64.0	15.6	26	N ₂	
15	345	1.08	0.37	14.1	6.3	35	N ₂	Effect of subcooling, Lower v_F than above
16	395	1.08	0.37	14.0	6.3	14	N ₂	
17	398	1.08	0.37	102.	6.3	14	N ₂	Effect of increased v_G than above
18	373	1.08	0.37	4.5	3.2	38	N ₂	Effect of subcooling, Lower v_F than above
19	214	1.08	0.37	4.4	3.2	27	N ₂	
20	391	1.08	0.37	4.6	3.2	15	N ₂	
21a, 21b	219	1.08	0.37	24.8	3.2	25	N ₂	Effect of increased v_G , Decreased ρ_G , Variability of agitated region
22	711	1.08	0.37	66.5	3.2	24	He	
23	452	1.08	0.37	40.9	10.5	23	N ₂	Details of flow field structure- roll waves, agitated region
24	451	1.08	0.37	19.0	10.5	23	N ₂	
25	433	1.08	0.37	25.1	4.2	15	N ₂	
26	448	1.08	0.37	29.7	4.2	23	N ₂	
27	705	1.08	0.37	37.5	10.5	24	He	Side lighting of flow field details, Effect of decreased ρ_G
28	704	1.08	0.37	97.0	10.5	24	He	
29	707	1.08	0.37	159.0	10.5	24	He	
30	706	1.08	0.37	66.3	10.5	24	He	

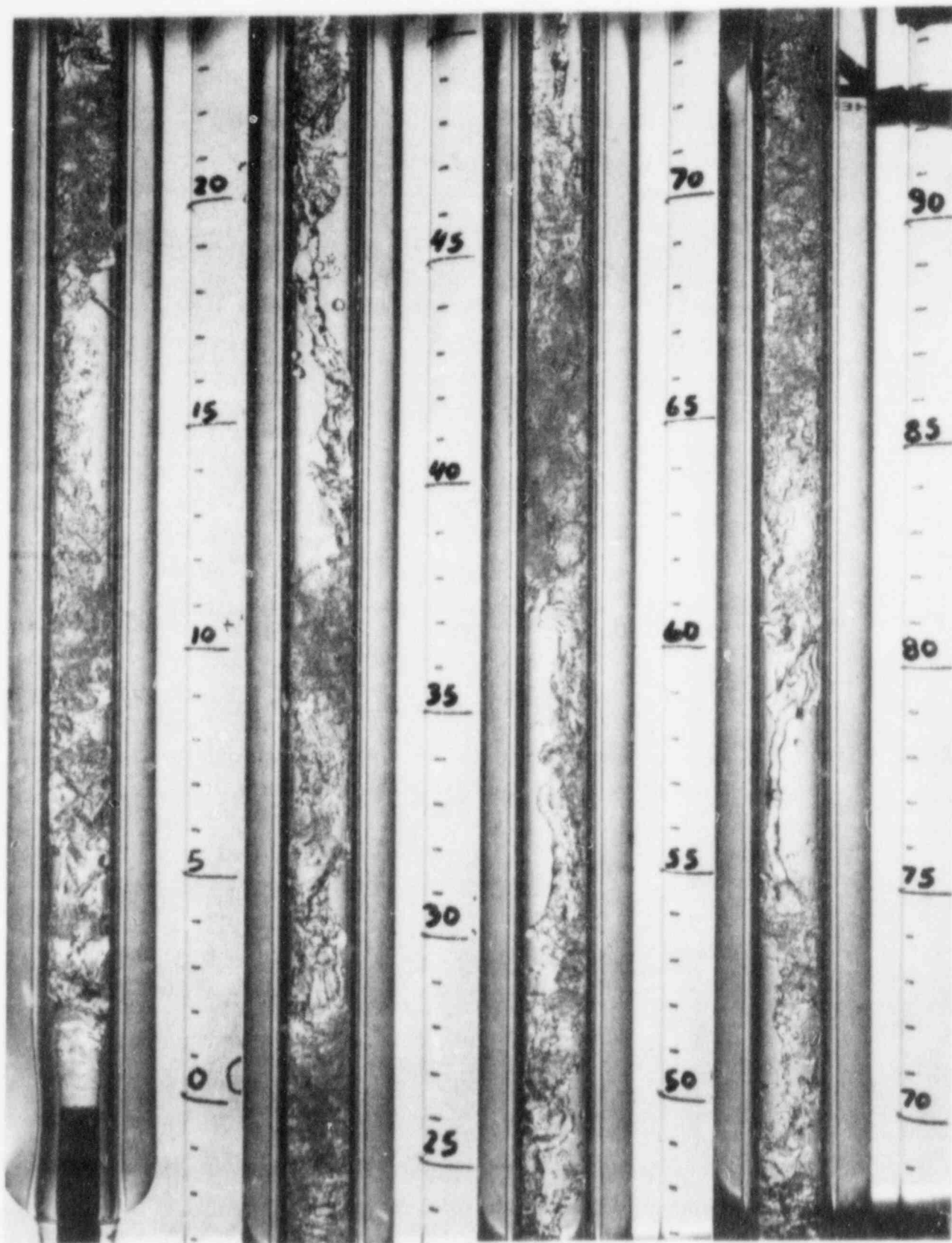


Fig. 11. Void = 0.56, $v_G = 71.6$ cm/s (N_2), $v_F = 43.4$ cm/s

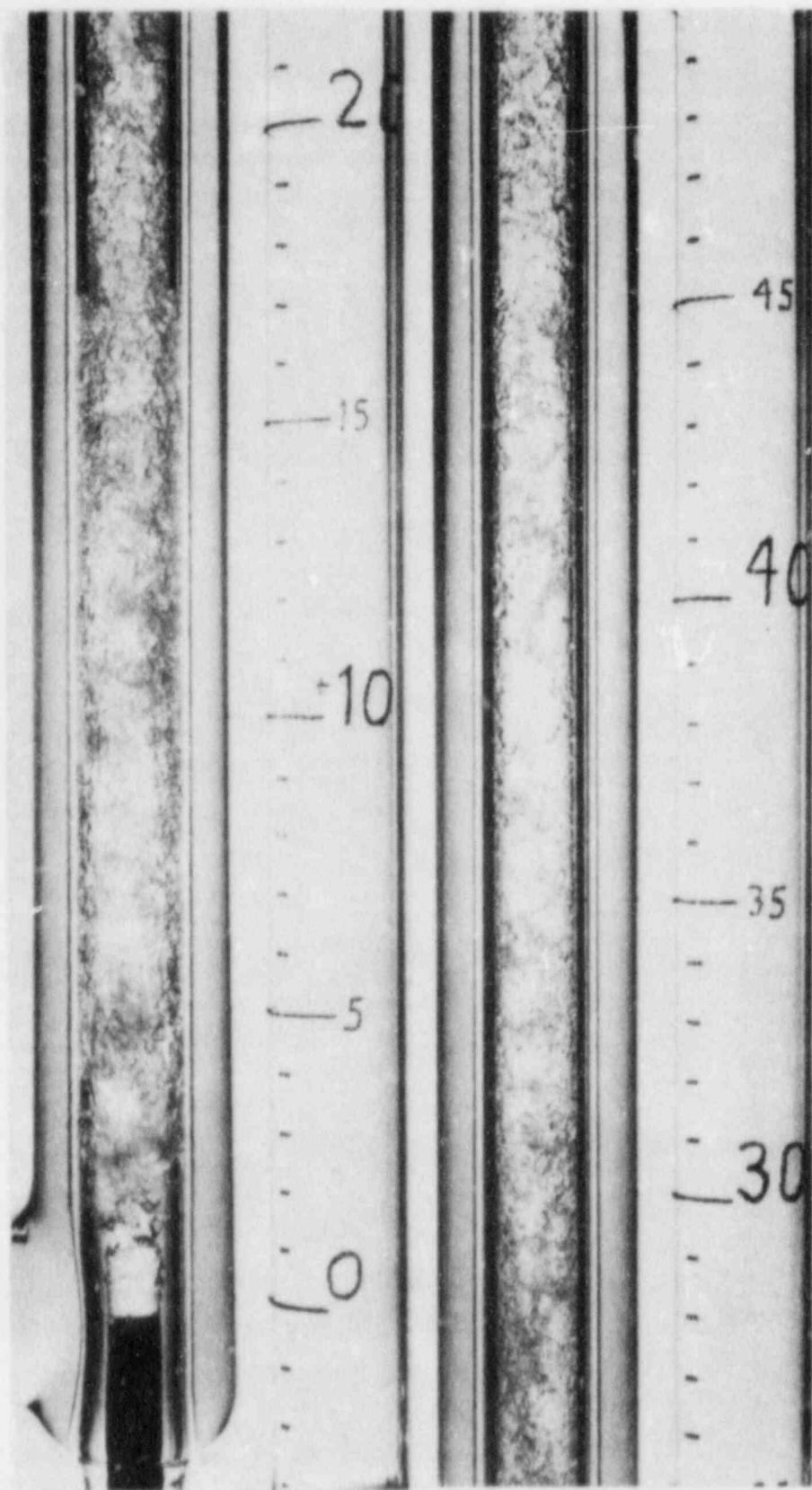


Fig. 12. Void = 0.56, $v_G = 154$ cm/s (N_2), $v_F = 43.4$ cm/s

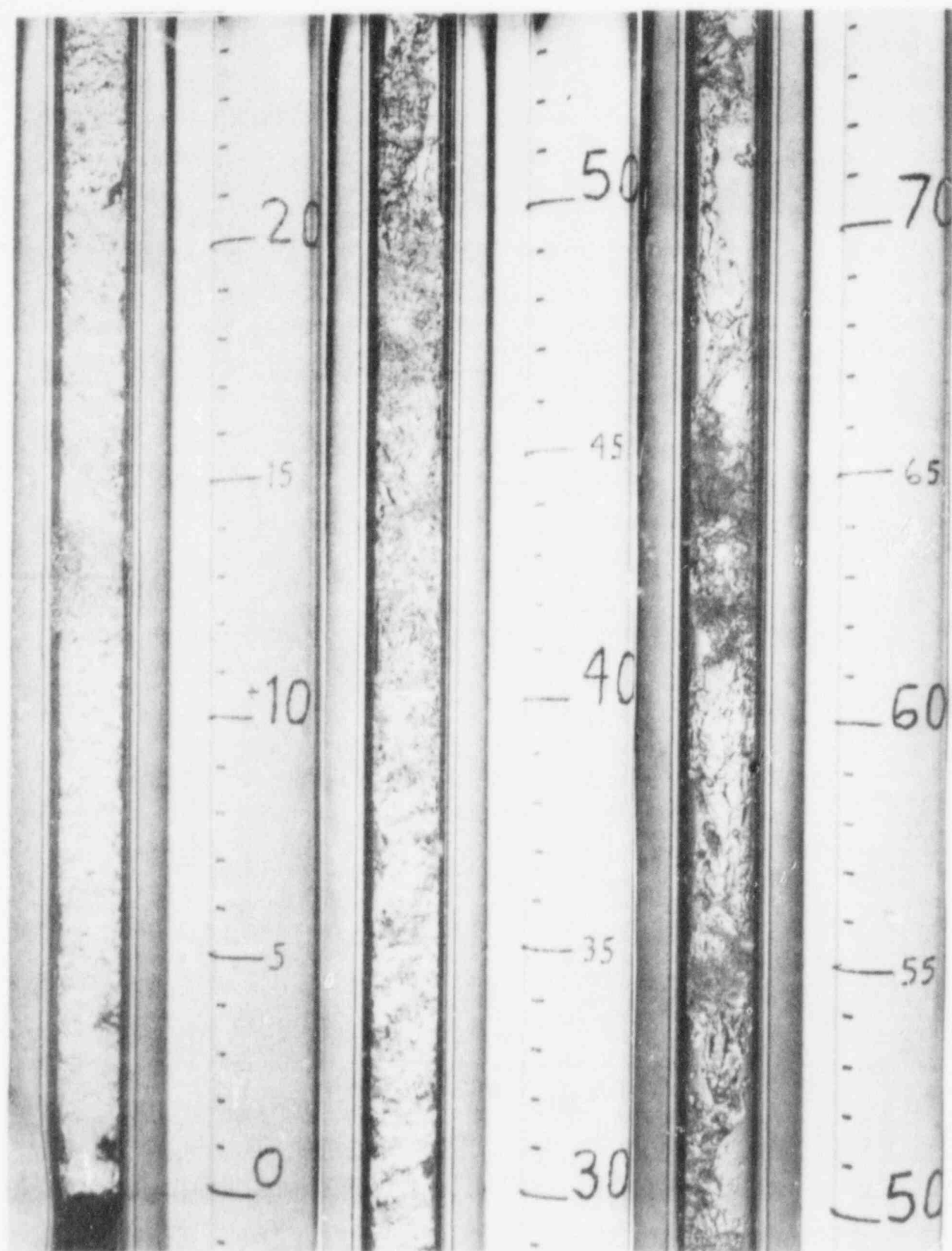


Fig. 13. Void = 0.37, $v_G = 1.7$ cm/s (N_2), $v_F = 15.6$ cm/s

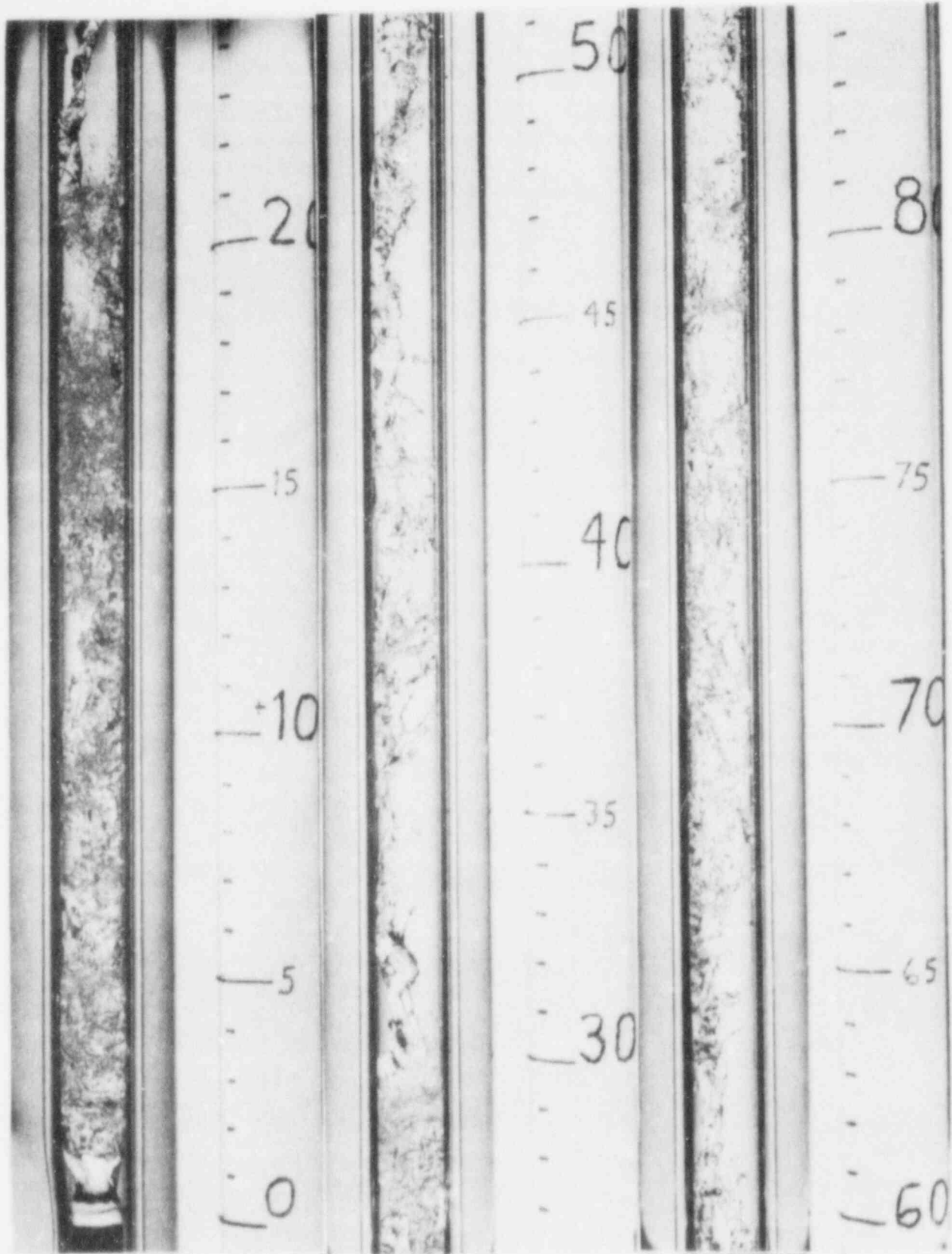


Fig. 14. Void = 0.37, $v_G = 64$ cm/s (N_2), $v_F = 15.6$ cm/s

In Fig. 14, inlet v_G has been increased, resulting in early formation of roll waves and a subsequent agitated region in close proximity to the heated wall (14-18 cm). Roll waves are forming within millimeters of the liquid nozzle exit. Trailing from the downstream edges of the agitated region are fine droplets (most under 200 μm), and a smooth, reduced diameter core remnant can be seen emerging from the agitated region. Agitated thin annular sheets, propagating downstream are small or nonexistent, due to the relatively large inlet v_G . As the reduced core jet approaches the wall (due to sinuous instabilities), roll waves or ligaments and smooth sheets form, and the core disperse into unstable slugs, and stable droplets up to 3 mm in diameter near the exit from the test section

3. Figures 15 and 16: Effect of Subcooling, Lower v_F

In Figs. 15 and 16, the inlet liquid flow rate is lower than in previous figures, and the stable inverted annular core is much reduced in length. In addition, chugging is much more severe, with the agitated region occurring over a greater length, and the reduced core remnants are much smaller. In Fig. 15, the subcooling is only 13°C, so that significant vapor generation results in rapid formation of the agitated region. Higher gas fluxes also result in larger drag forces and attendant larger distorted drops/slugs being lifted to the test section exit. Only very small core remnants (smooth cylindrical jets) can be seen above the agitated region.

In Fig. 16, with subcooling increased to 34°C, suppressed vapor generation leads to a relatively long (13 cm) smooth intact inverted annular core (a small rewetting patch at 2-3 cm proving to be insignificant). Decreased vapor generation, while at the same inlet v_G as Fig. 15, results in a larger remnant core above the agitated region, and also in lower outlet gas flux, with only smaller droplets, most under 3 mm, being lifted out of the test section.

4. Figure 17: Effect of Increase v_G

In Fig. 17, all flow parameters are the same as those for Fig. 16, except inlet v_G has been increased from 14.0 cm/s up to 102 cm/s. The effect is very similar to that obtained by decreasing inlet liquid subcooling (see

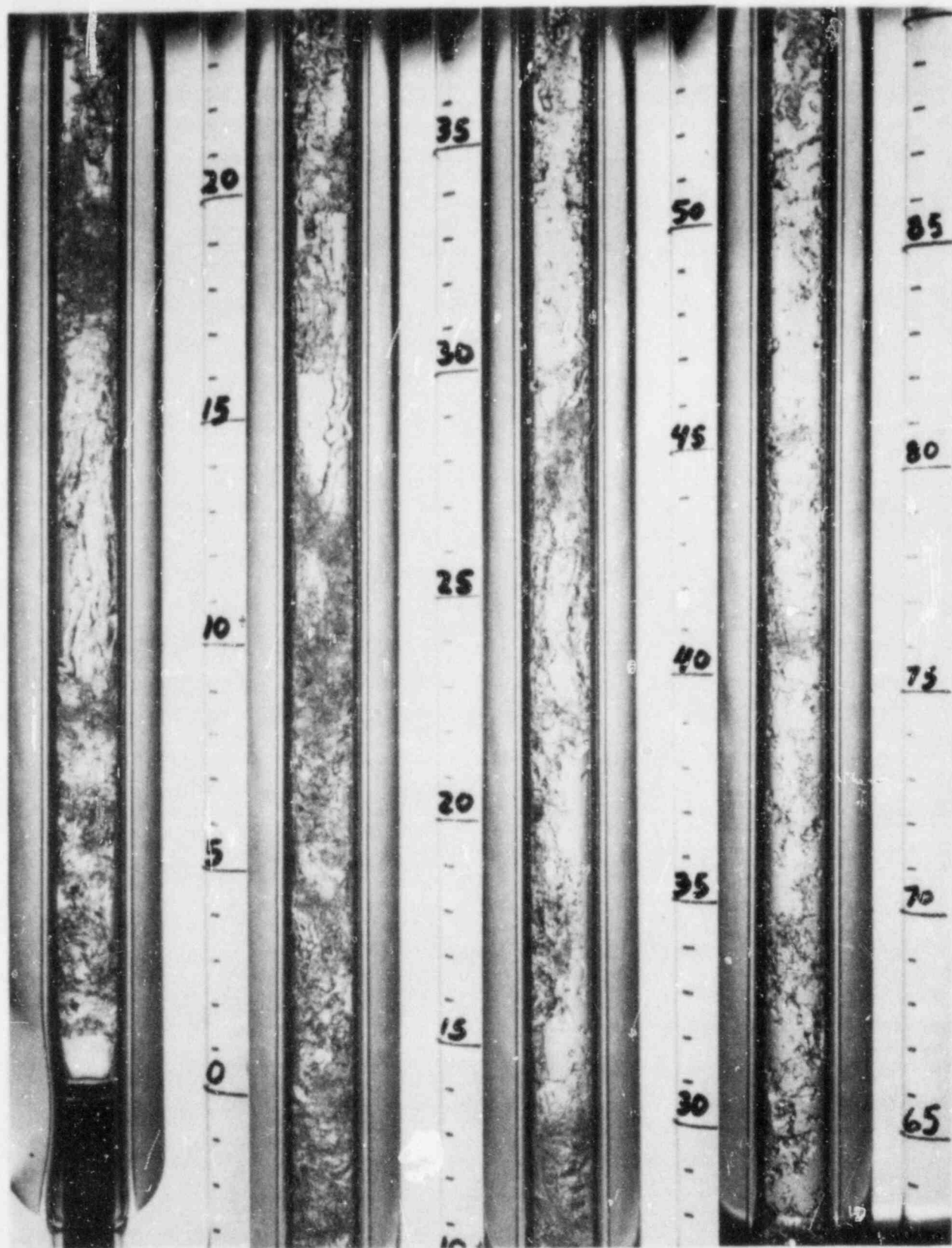


Fig. 15. $v_G = 14.1$ cm/s (N_2), $v_F = 6.3$ cm/s, $T_F = 35^\circ\text{C}$

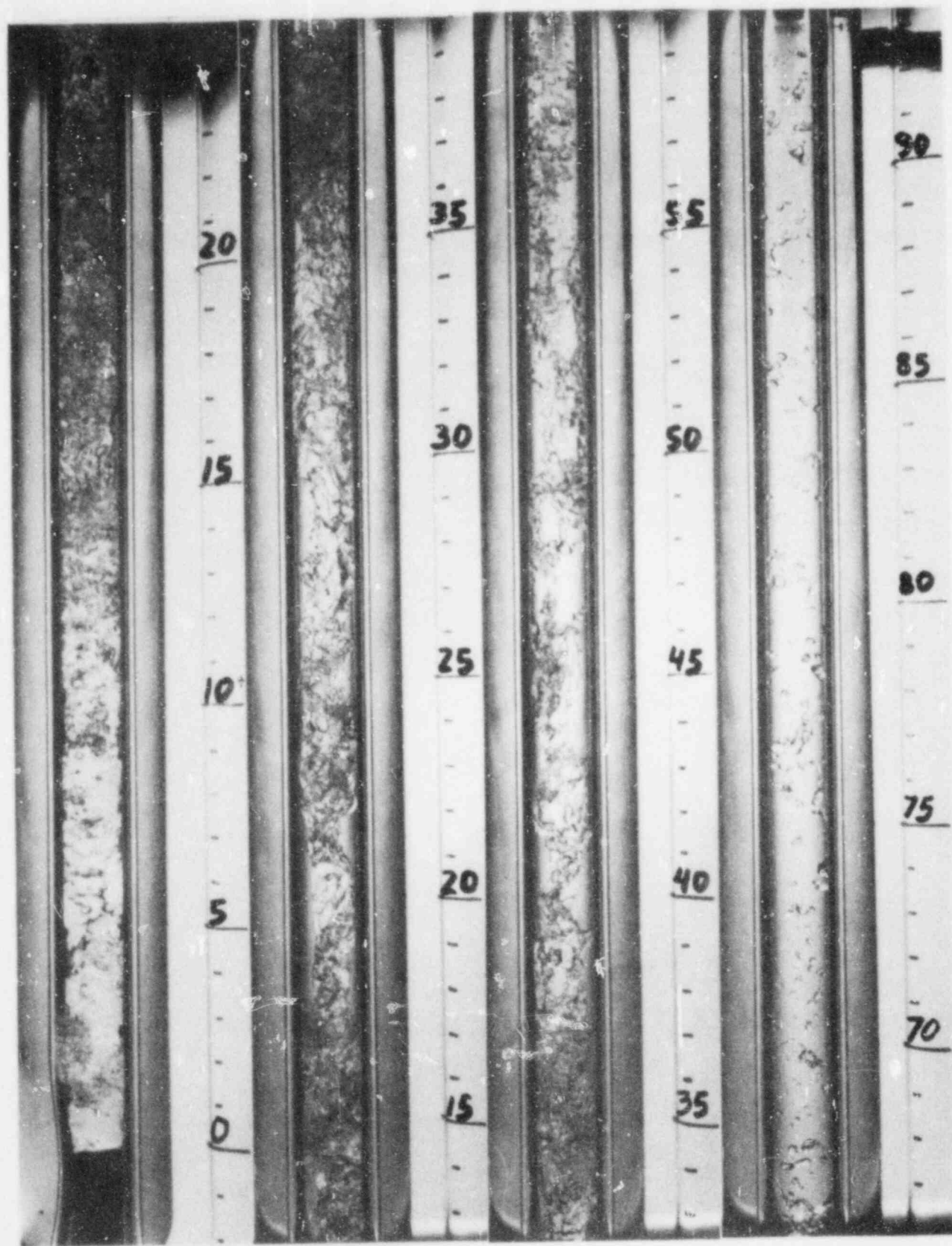


Fig. 16. $v_G = 14.0$ cm/s (N_2), $v_F = 6.3$ cm/s, $T_F = 14^\circ\text{C}$

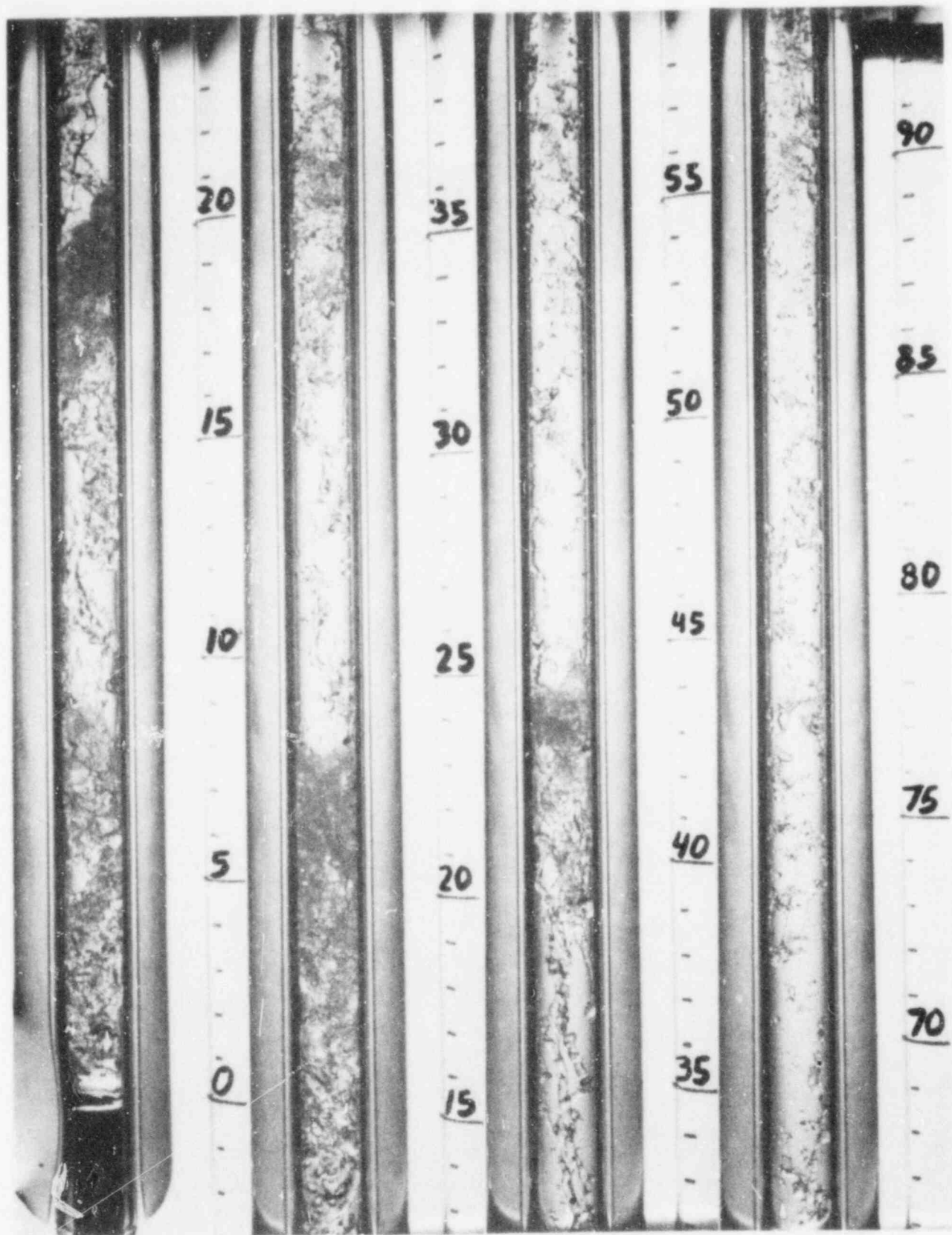


Fig. 17. $v_G = 102$ cm/s (N_2), $v_F = 6.3$ cm/s, $T_F = 14^\circ\text{C}$

Fig. 15); earlier development of the agitated region, smaller core remnants appearing above the agitated region, and more liquid, in larger dispersed masses, being lifted up to the test section exit.

5. Figures 18, 19 and 20: Effect of Subcooling, Very Low v_F

In Figs. 18, 19 and 20, the inlet liquid flowrate is lower still than in previous figures. Above the agitated region, the liquid core is severely depleted, existing only as small ligaments (1-2 mm in diameter and a few cm in length), for all but the largest liquid subcooling, even though inlet v_G is quite small (4.4-4.6 cm/s). In these three figures, inlet subcooling varies from only 10°C (Fig. 18) up to 33°C (Fig. 20). Again, as vapor generation is suppressed by increasing subcooling, the liquid core becomes more stable, the agitated region depletes less of the core (larger core remnants above the agitated region) and only smaller liquid masses are carried upward to the test section outlet by the reduced gas flux.

6. Figures 21 and 22: Agitated Region Variability, Effects of v_G and ρ_G

In Fig. 21 (21a and 21b) the violent chugging behavior at low inlet liquid and gas flowrates is demonstrated, in a series of photographs taken at the inlet portion of the heated test section. Above the stable inverted annular liquid core, the agitated region varies constantly, periodically ejecting large liquid masses. Void fraction in this region varies from near 1.0 to near 0, as this chugging occurs. The flow inlet parameters for Fig. 21 are the same as those for Fig. 19, with the exception of increased inlet v_G .

In Fig. 22, inlet liquid subcooling, liquid flowrate, and void fraction are the same as for Fig. 21. However, helium rather than nitrogen, is the injected gas species, ($\rho_G = 1.29 \text{ kg/m}^3$ for Fig. 21, $\rho_G = 0.18 \text{ kg/m}^3$ for Fig. 22), and inlet v_G has been increased from 25 cm/s up to 66 cm/s. Given the hydrodynamic dependency upon $\rho_G v_G^2$ determined in the previous adiabatic study [9,39-42], it is not surprising that the flow patterns displayed in Figs. 21 and 22 are very similar.

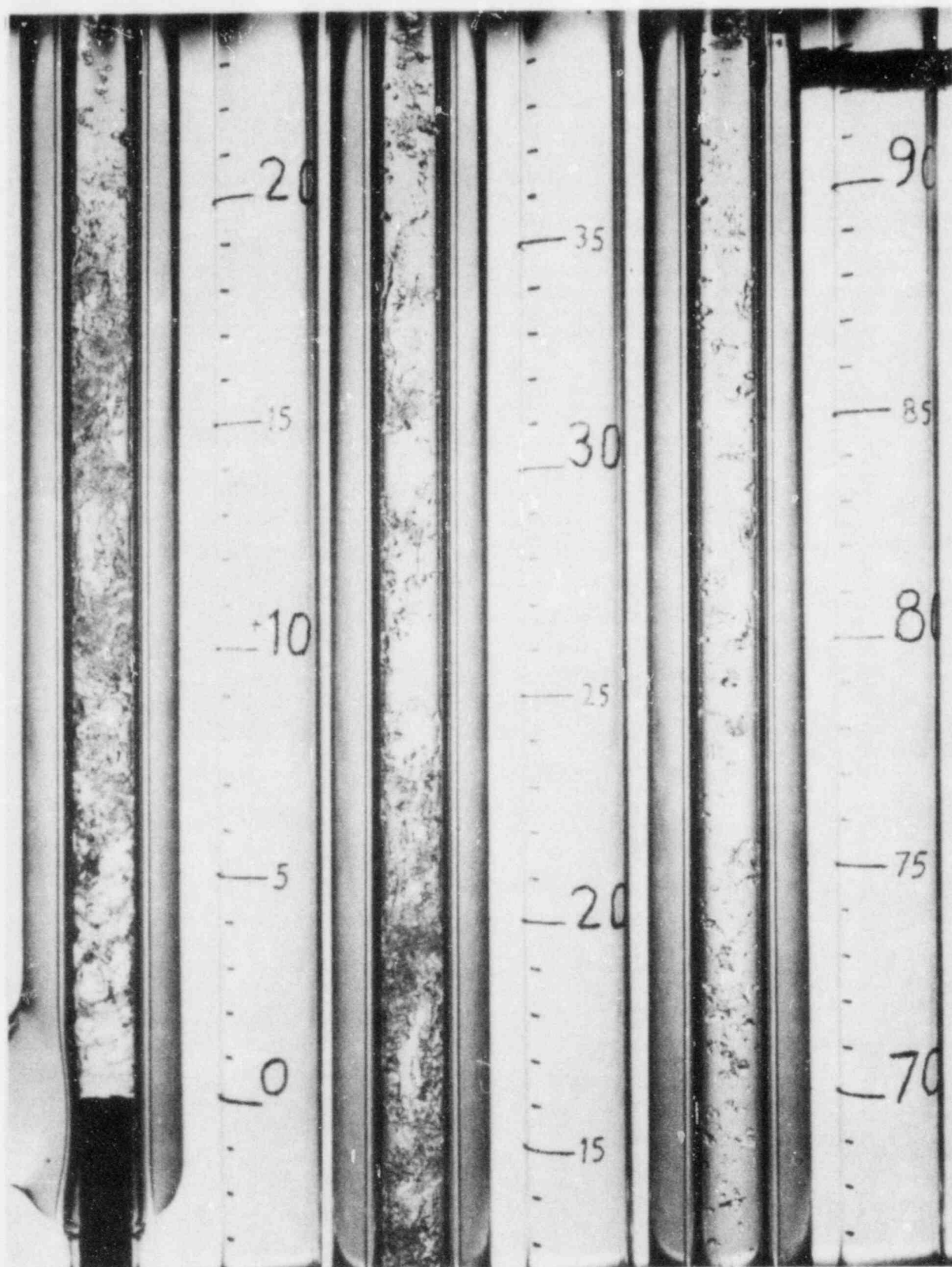


Fig. 18. $v_G = 4.5$ cm/s (N_2), $v_F = 3.2$ cm/s, $T_F = 38^\circ\text{C}$

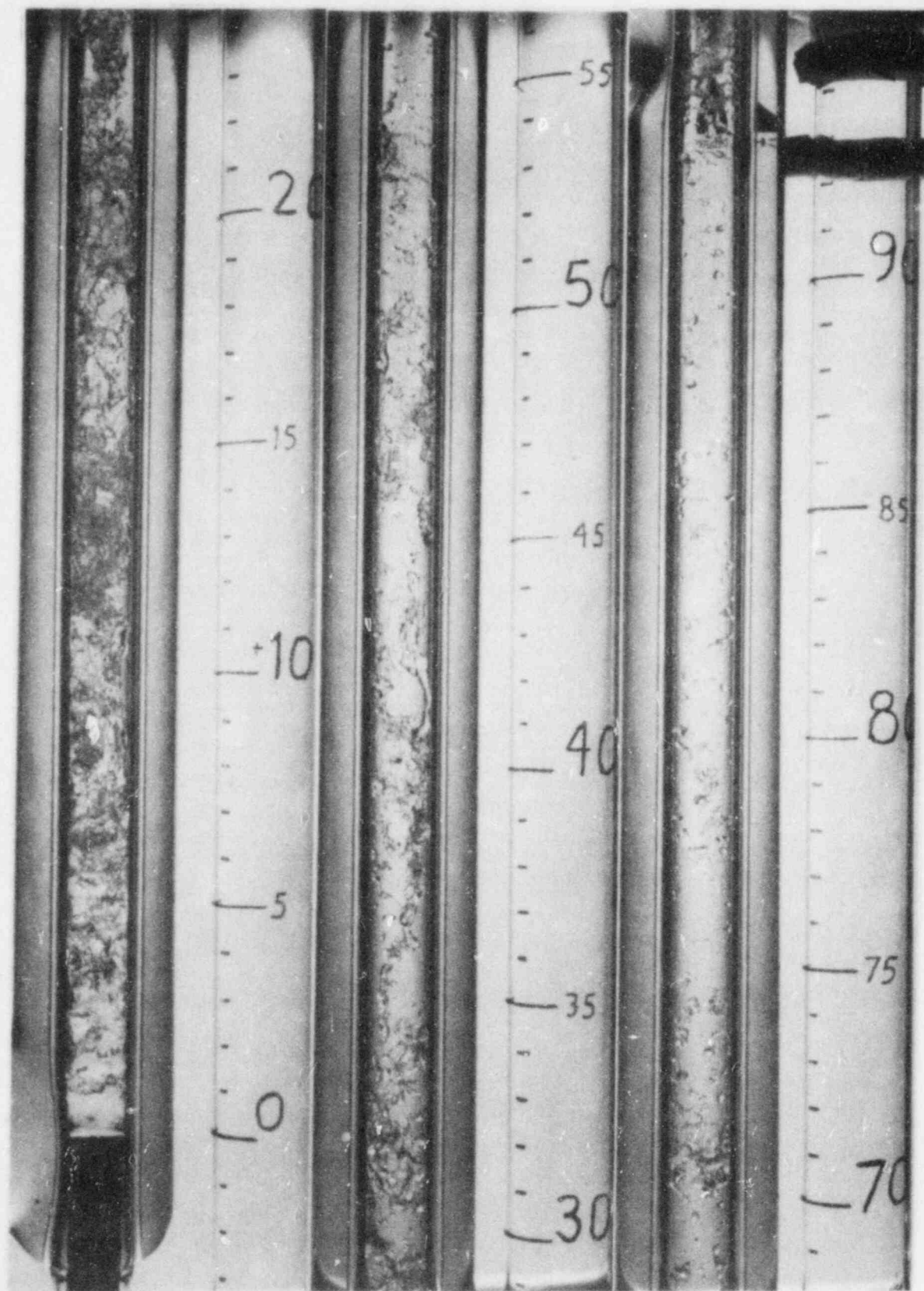


Fig. 19. $v_G = 4.4$ cm/s (N_2), $v_F = 3.2$ cm/s, $T_F = 27^\circ\text{C}$

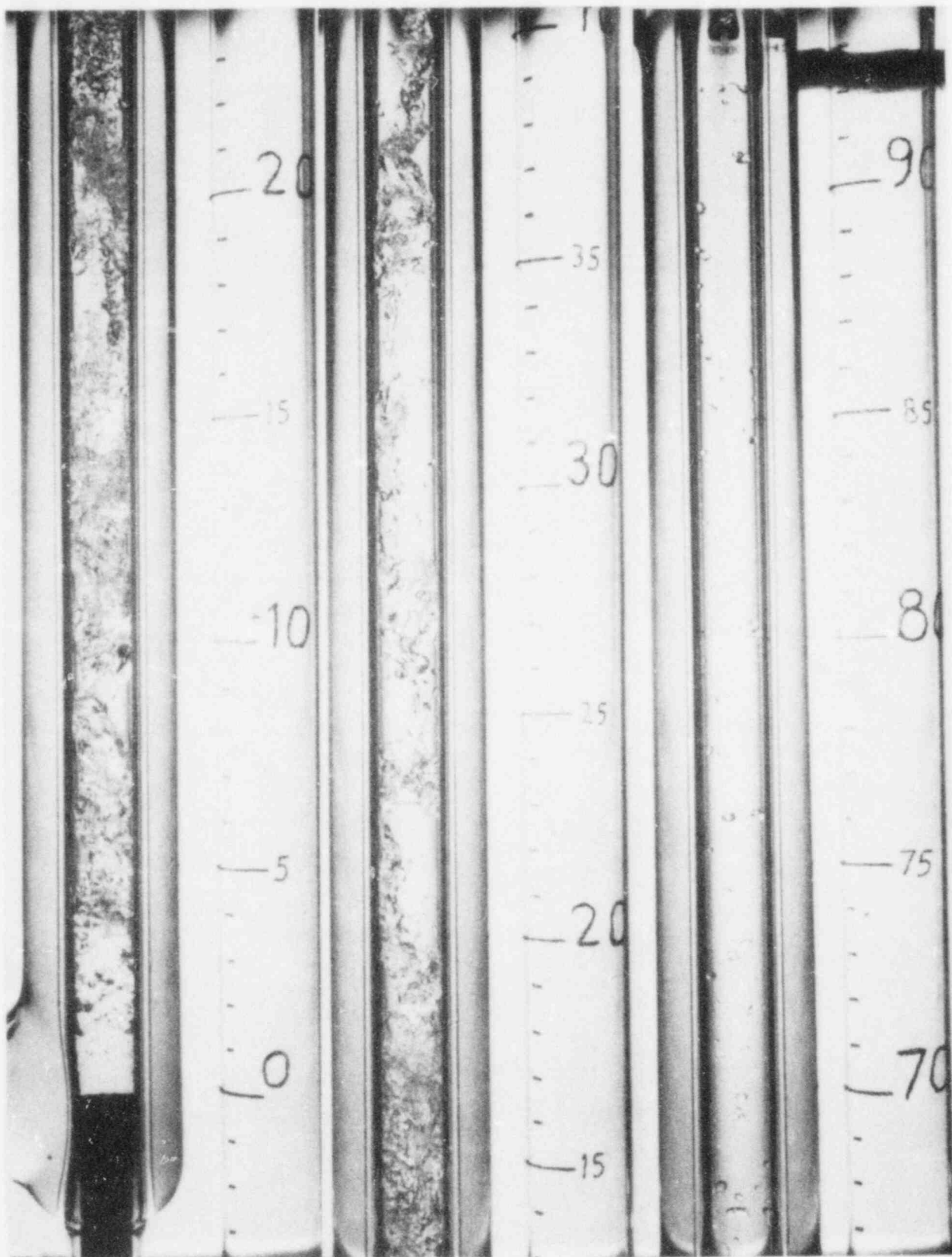


Fig. 20. $v_G = 4.6$ cm/s (N_2), $v_F = 3.2$ cm/s, $T_F = 15^\circ\text{C}$

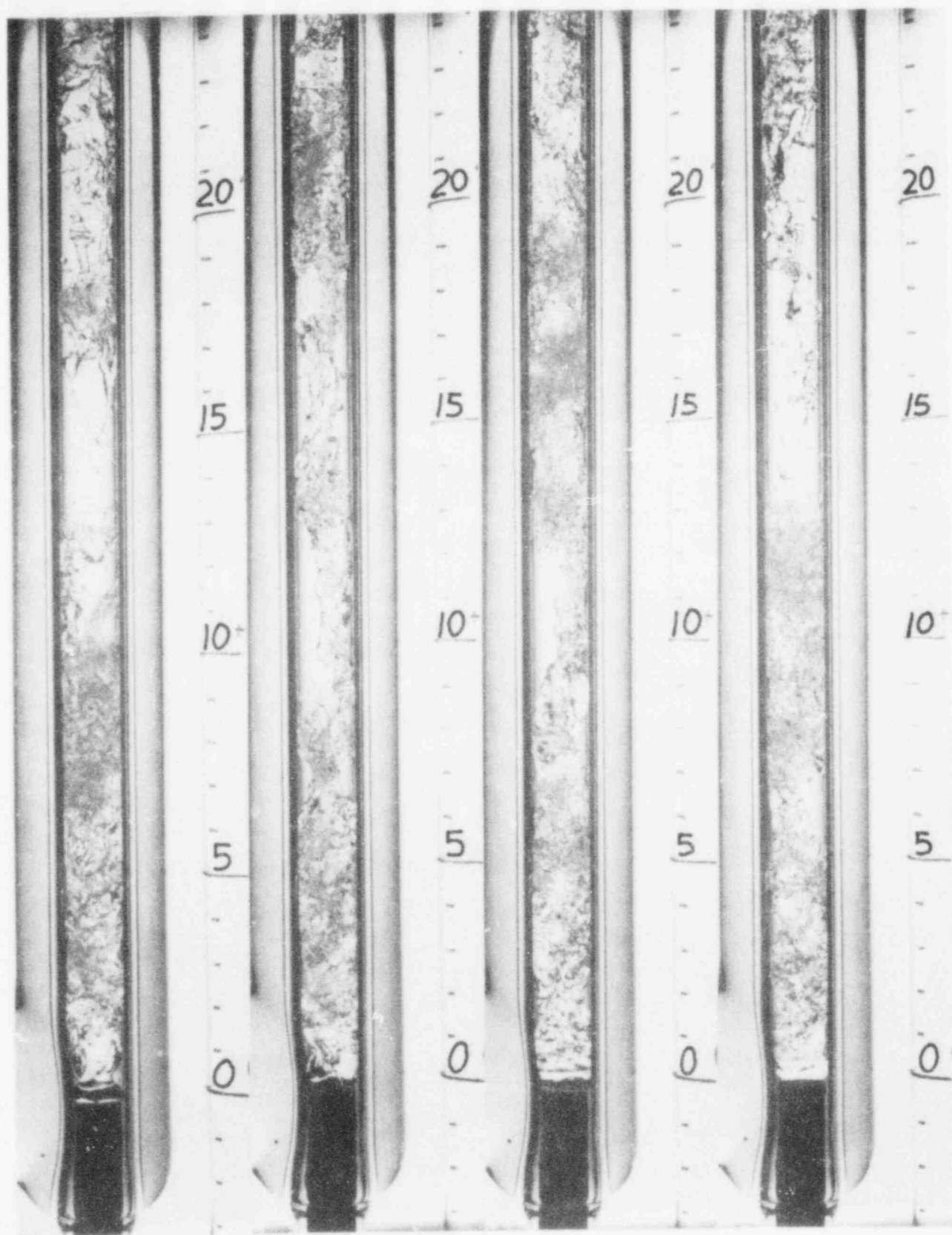


Fig. 21a. $v_G = 24.8$ cm/s (N_2), $v_F = 3.2$ cm/s, $T_F = 25^\circ\text{C}$

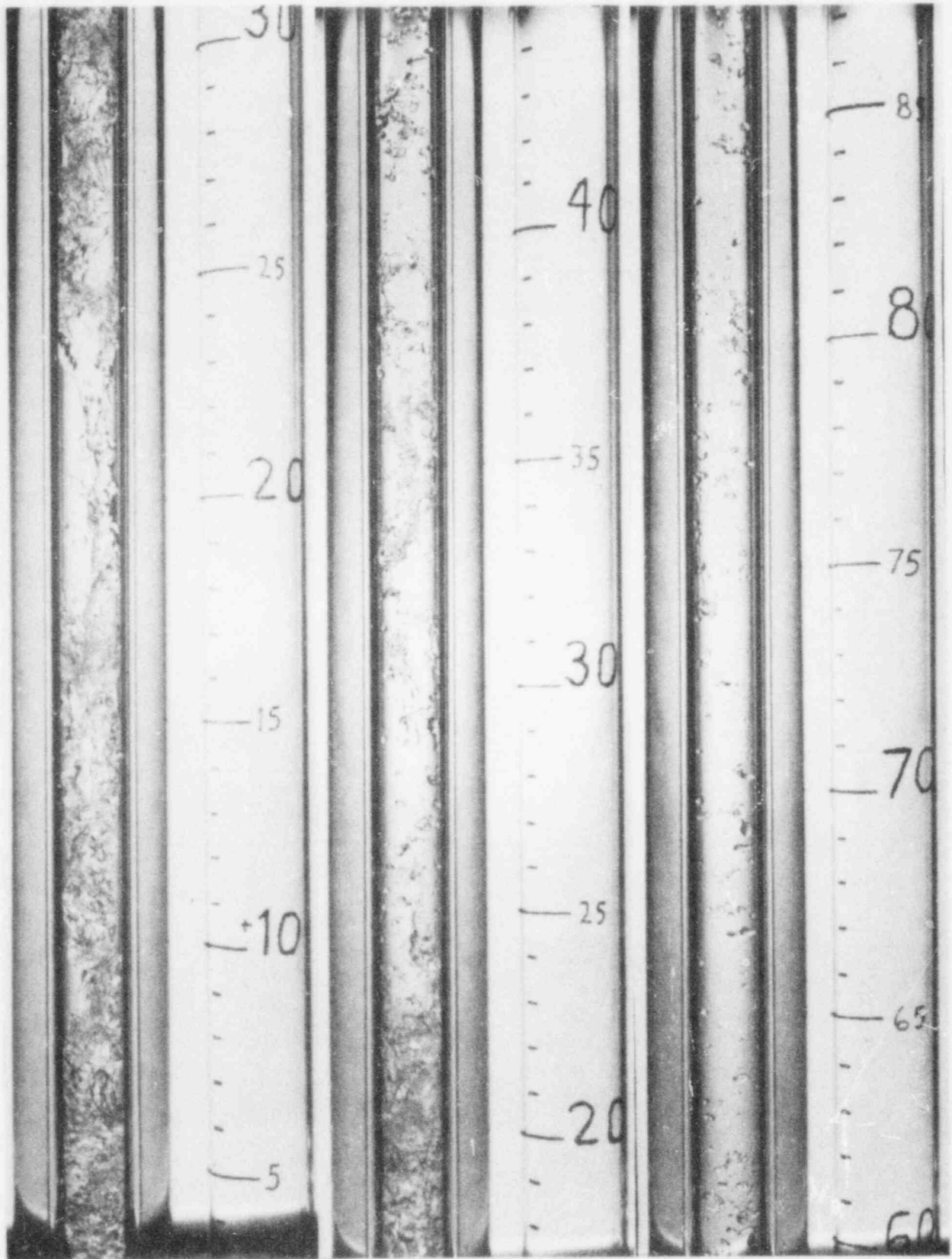


Fig. 21b. $v_G = 24.8$ cm/s (N_2), $v_F = 3.2$ cm/s, $T_F = 25^\circ\text{C}$

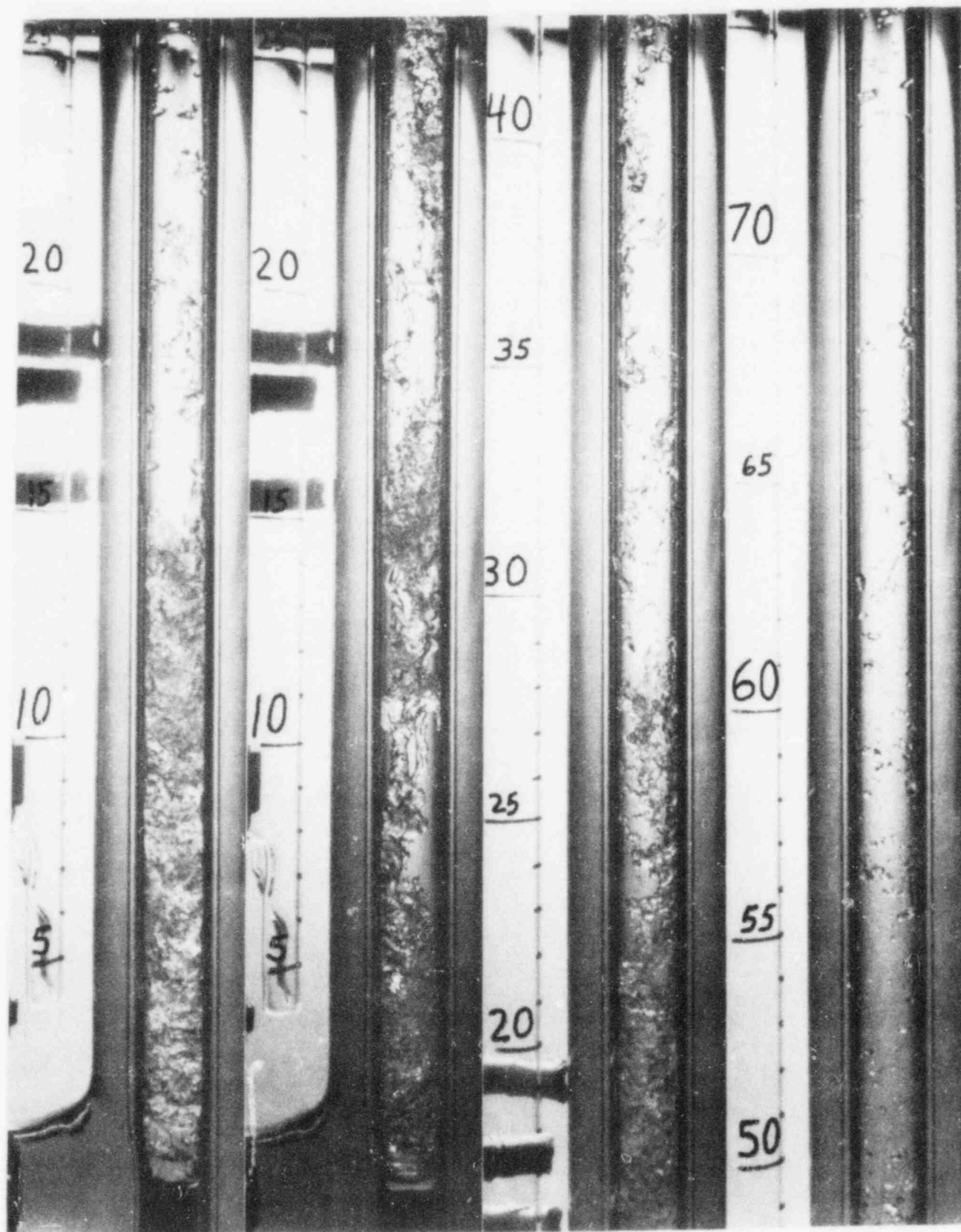


Fig. 22. $v_G = 66.5$ cm/s (He), $v_F = 3.2$ cm/s, $T_F = 24^\circ\text{C}$

7. Figures 23, 24, 25 and 26: Details of Flow Field Structure

In the previous photographic figures, all the photographs were taken using a 55 mm lens, which results in good overall views of the flow field, but limits the amount of detail one can discern. The photographs in Figs. 23-26, however, were taken with a 105 mm lens, so that greater detail of the flow structure are visible. For all figures, relatively low to moderate inlet flowrates were used, nitrogen is the injected gas and backlighting is used.

In Fig. 23, one can see droplets being entrained from the crests of roll waves forming near the liquid inlet nozzle. Downstream, at 25 cm, the agitated region is forming. Surface structure is agitated and quite fine, below the resolution capabilities of the photographic equipment (roughly 50 μm). At the downstream edge of this agitated region, small droplets are forming and accelerating downstream rapidly. Further downstream, at 45 cm, an agitated sheet is thinning, dispersing into droplets and small ligaments as it passes over a smooth liquid core remnant. Droplets down to 100 μm can be observed.

The fine agitated structure of the agitated region and agitated sheets/dense droplet films, the small droplets generated in these agitated structures, and the eventual break-up of the agitated sheets and liquid core remnants can similarly be seen in Figs. 24, 25 and 26. In Fig. 24, the thinning of a small liquid sheet encircling a core remnant distorted by sinuous instabilities, and a cloud of large droplets and the unstable ligaments from which they form are visible. In Fig. 25, a large, thin annular sheet at 25 cm can be seen passing over a smooth cylindrical core remnant. This sheet is not coherent, and the core remnant can be seen through gaps in this sheet. While very thin, this annular sheet is still in close proximity, while the sheet-like distorted liquid core seen at 40 cm is much thicker, but well removed from the heated wall, and exhibits a much less agitated surface structure. Finally, in Fig. 26, a liquid core distorting into large ligaments at 25 cm, small agitated regions (or areas of roll wave entrainment) forming on the crest of a varicose distortion (alternating expansion/contraction) of the liquid core at 19 and 25 cm, and the degrading of an agitated sheet into a smooth sheet and ligaments (as the liquid mass decreases and moves away from the heated wall) at 34 cm can be seen.

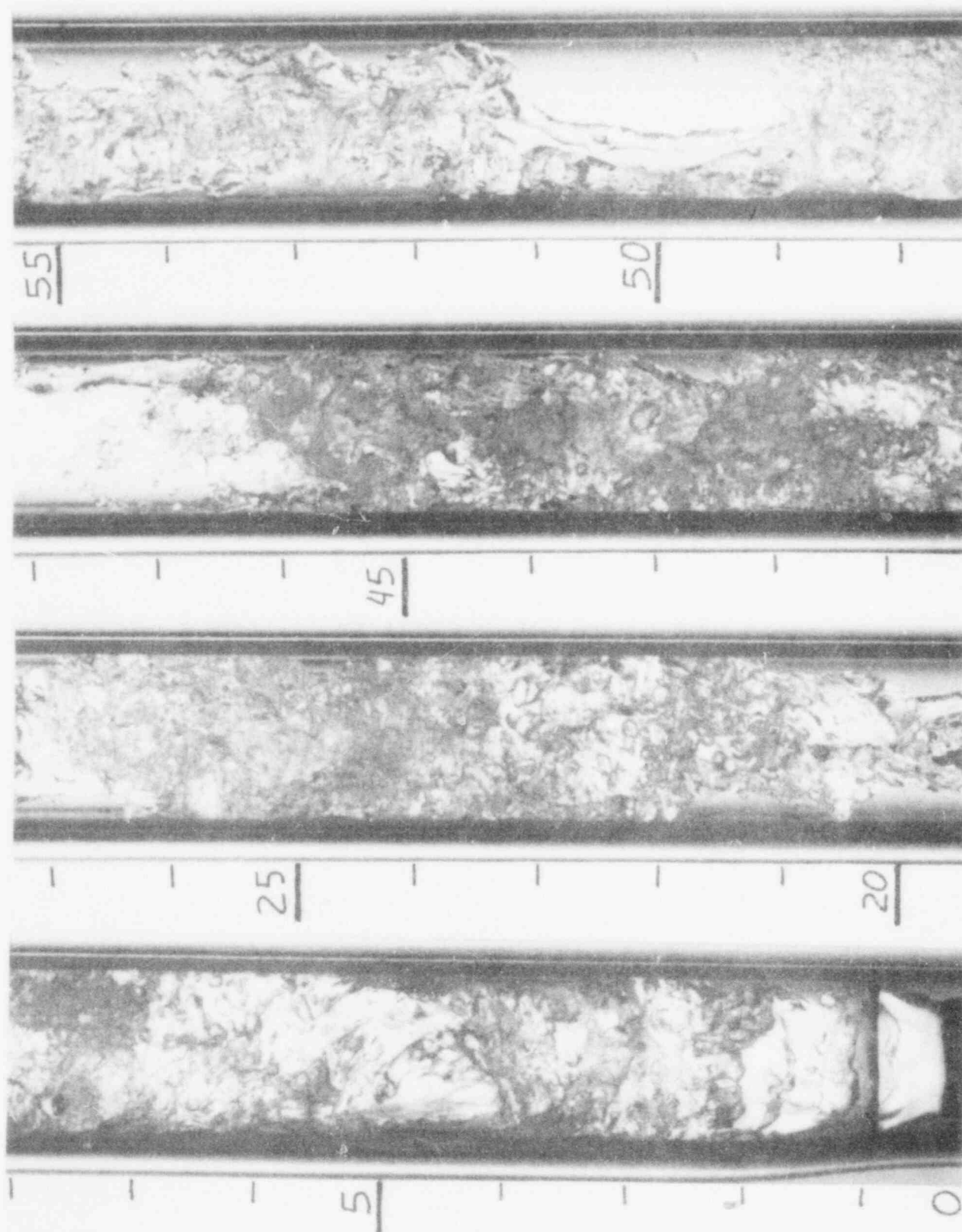


Fig. 23. $v_G = 40.9$ cm/s (N_2), $v_F = 10.5$ cm/s, $T_F = 23^\circ\text{C}$

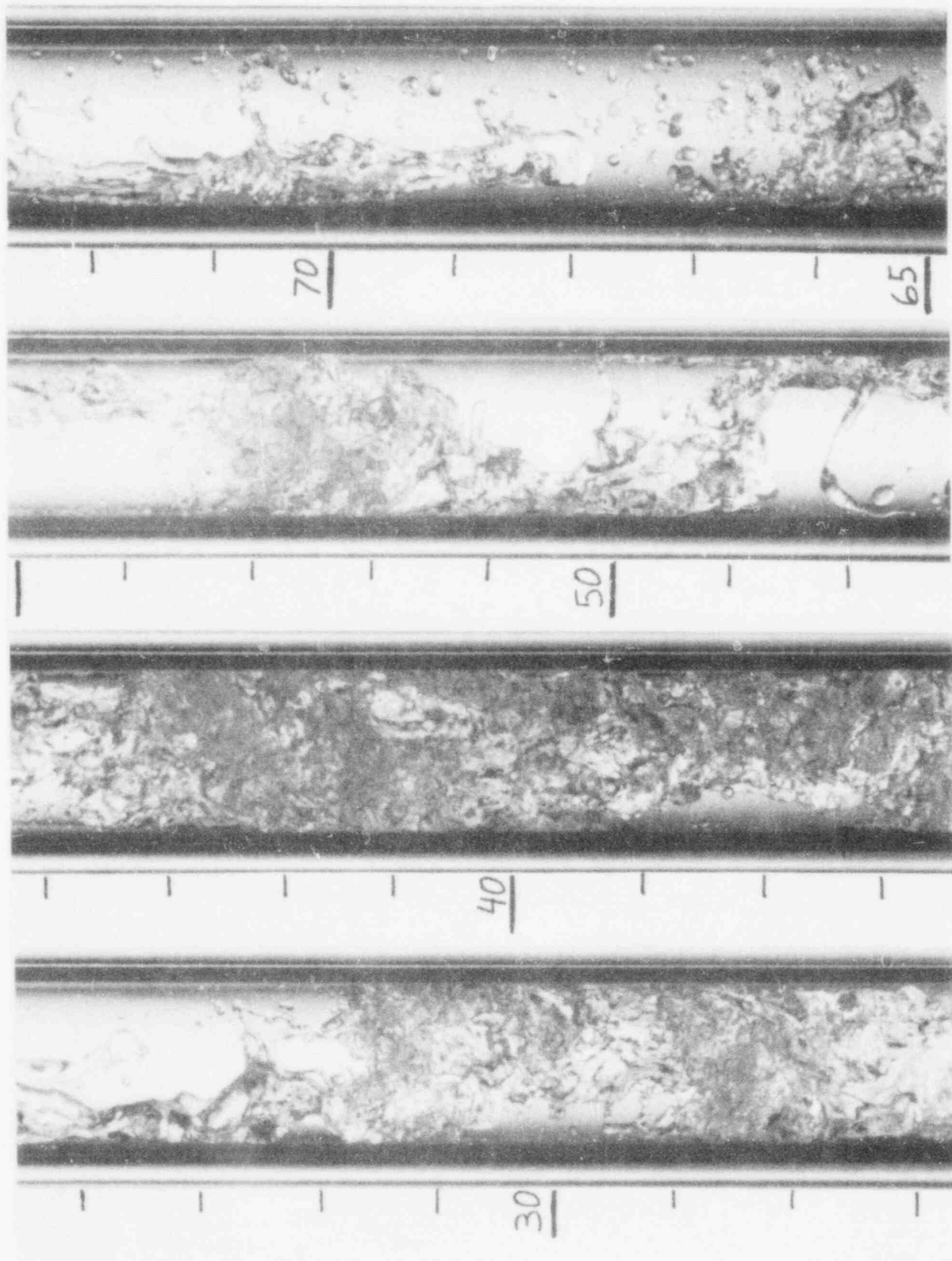


Fig. 24. $v_G = 19.0$ cm/s (N_2), $v_F = 10.5$ cm/s, $T_F = 23^\circ\text{C}$

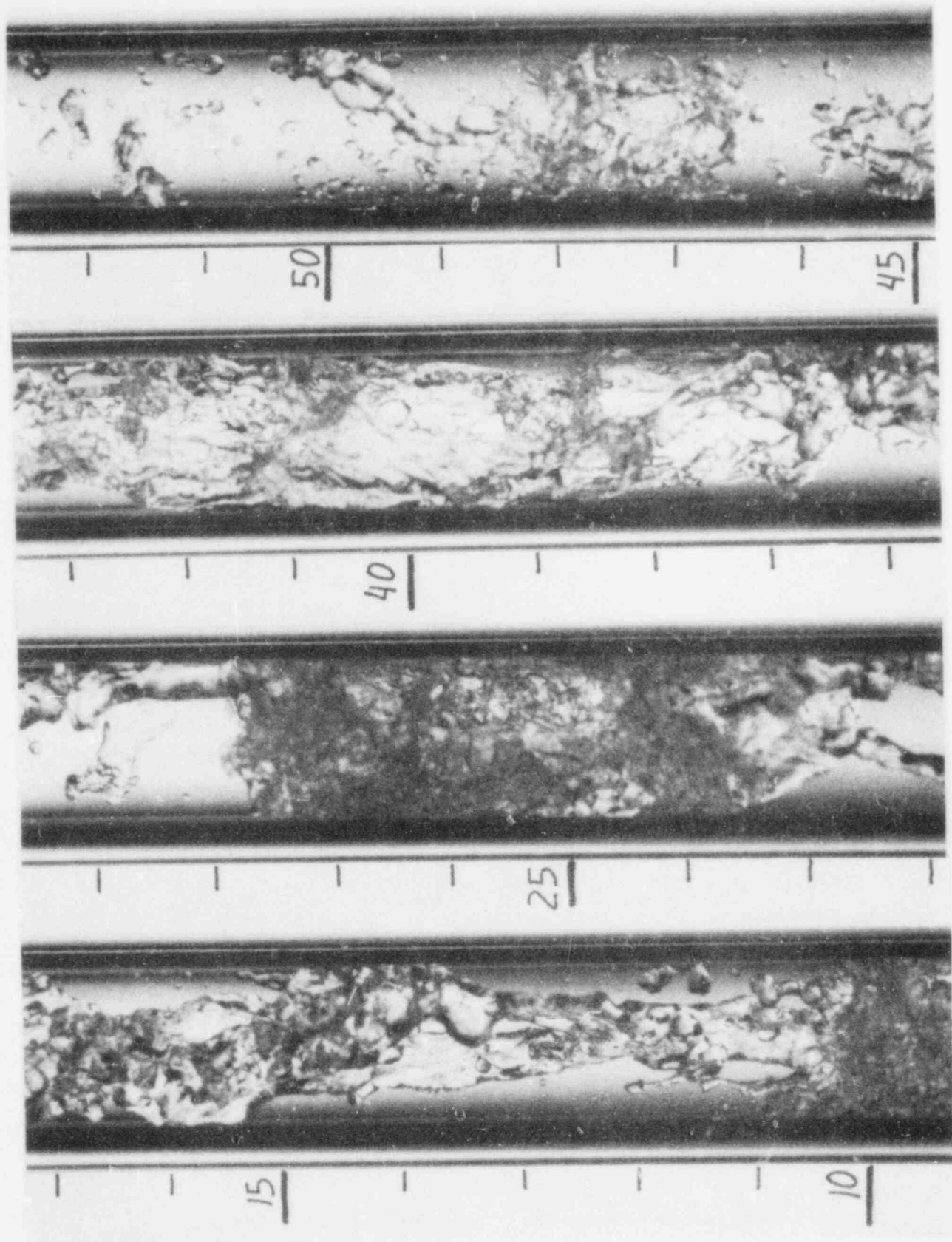


Fig. 25. $v_G = 25.1$ cm/s (N_2), $v_F = 4.2$ cm/s, $T_F = 15^\circ\text{C}$

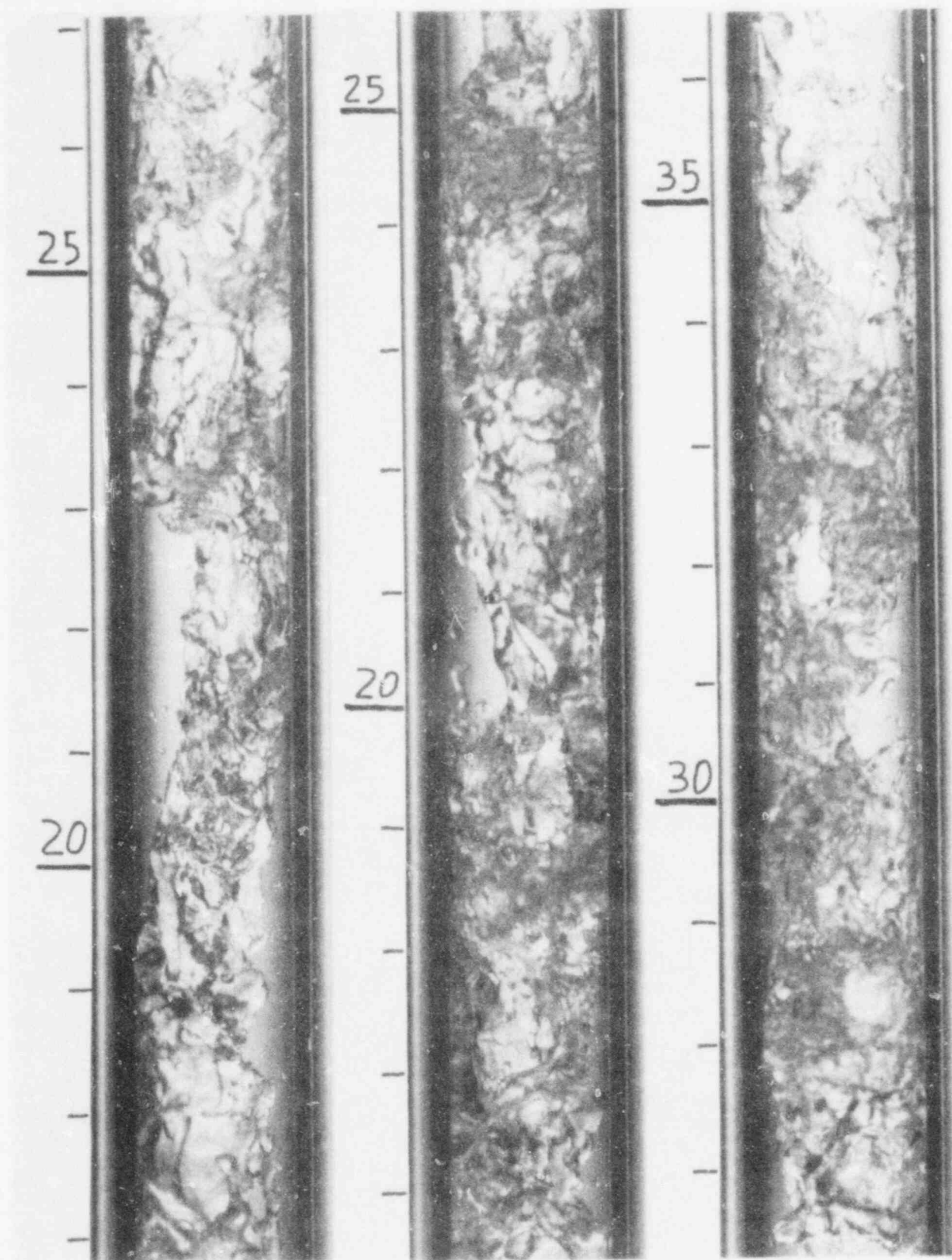


Fig. 26. $v_G = 29.7$ cm/s (N_2), $v_F = 4.2$ cm/s, $T_F = 23^\circ\text{C}$

8. Figures 27, 28, 29 and 30: Sidelighting, Helium Inlet Gas, Flow Field Structure

In Figs. 27-30, helium rather than nitrogen is the gas species used as the gas annulus injected around the R-113 liquid core jets at the heated inlet to the test section. As in the case of Figs. 21 and 22, for the lower density helium, larger inlet volumetric flowrates are required to form the same flow field patterns, than are required when using the higher density nitrogen. For these figures, sidelighting rather than backlighting was used. While this makes the outlines of large liquid masses less distinct, it makes small, transparent droplets more visible. In addition, the surface details of the agitated region become more distinct, since light is bounced directly off these surfaces, rather than diffused through the bulk of the liquid in the test section.

Figure 27 shows the distortion of the liquid core remnant into a smooth thick sheet, a large number of fine droplets streaming downstream of an agitated region at 45 cm, and a smooth reduced diameter liquid core jet emerging from the downstream edge of an agitated region. The number of droplets highlighted by sidelighting is much higher than with backlighting. In Fig. 28, a similar distortion of the liquid core remnants into large smooth sheets and ligaments at 15-20 cm above the liquid nozzle inlet, and moderately agitated core-surface disturbances can be seen. In Fig. 29, degrading agitated liquid sheets, a smooth core remnant exhibiting sinuous jet instabilities, and dense droplet clouds can be seen. Finally, Fig. 30 shows the leading (downstream) edges of agitated regions with attendant fine droplets (down to 25 μm), and ligaments formed from liquid core remnants at high magnification. However, with the 200 mm lens used for these photographs, depth of field is quite limited. The agitated surface facing the camera, while located at the center of this depth of field and illuminated with sidelighting, still displays a fine structure beyond the limits of lens/film resolution.

D. Selected Data on Flow Regimes, Droplet Sizes

Correlations have not been developed, to date, to encompass all the data derived from analysis of the still photographs and motion pictures taken of the test section flow field. However, to help illustrate the hydrodynamic observations made in the previous sections, selected data is presented in this section.

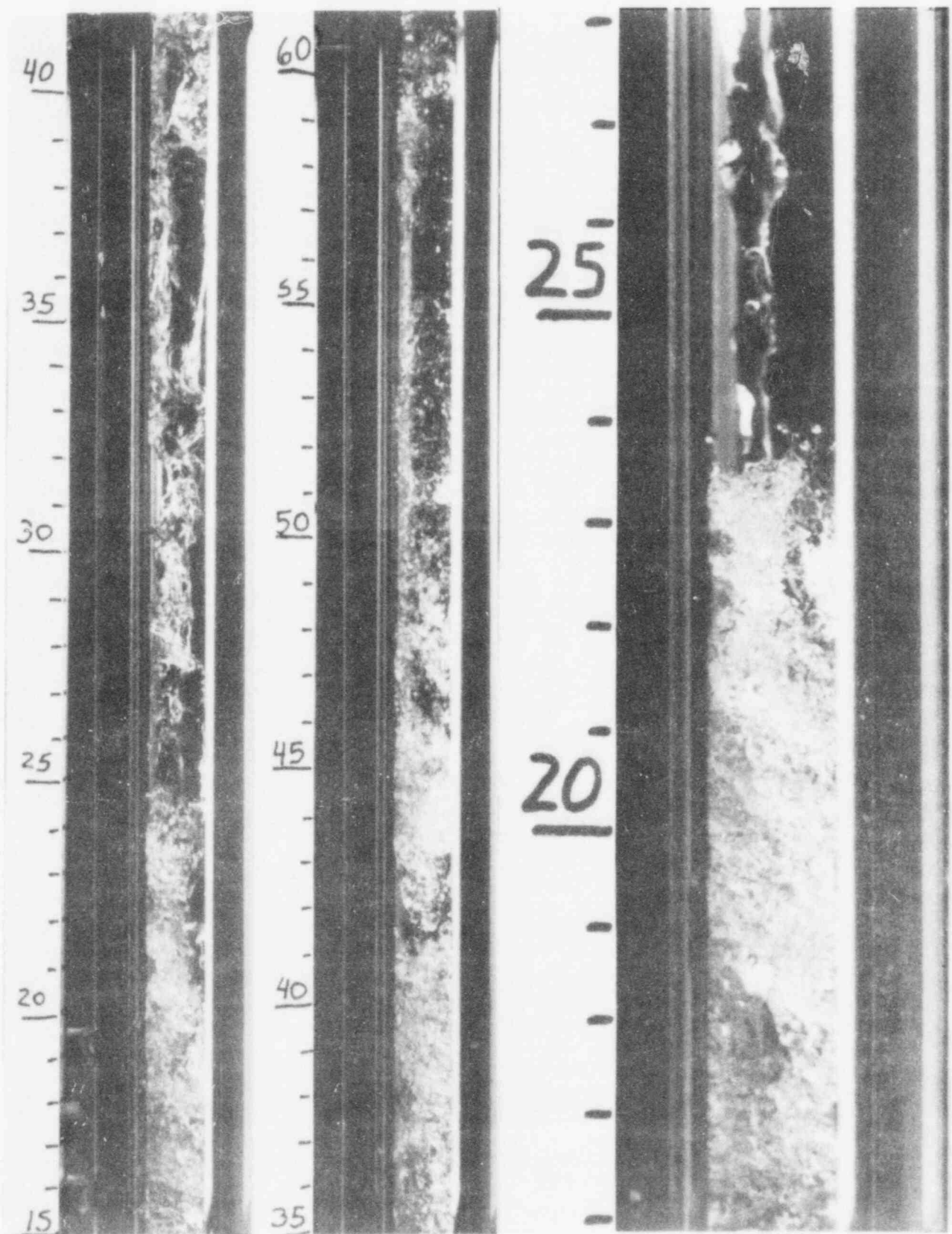


Fig. 27. $v_G = 37.5$ cm/s (He), $v_F = 10.5$ cm/s, $T_F = 24^\circ\text{C}$

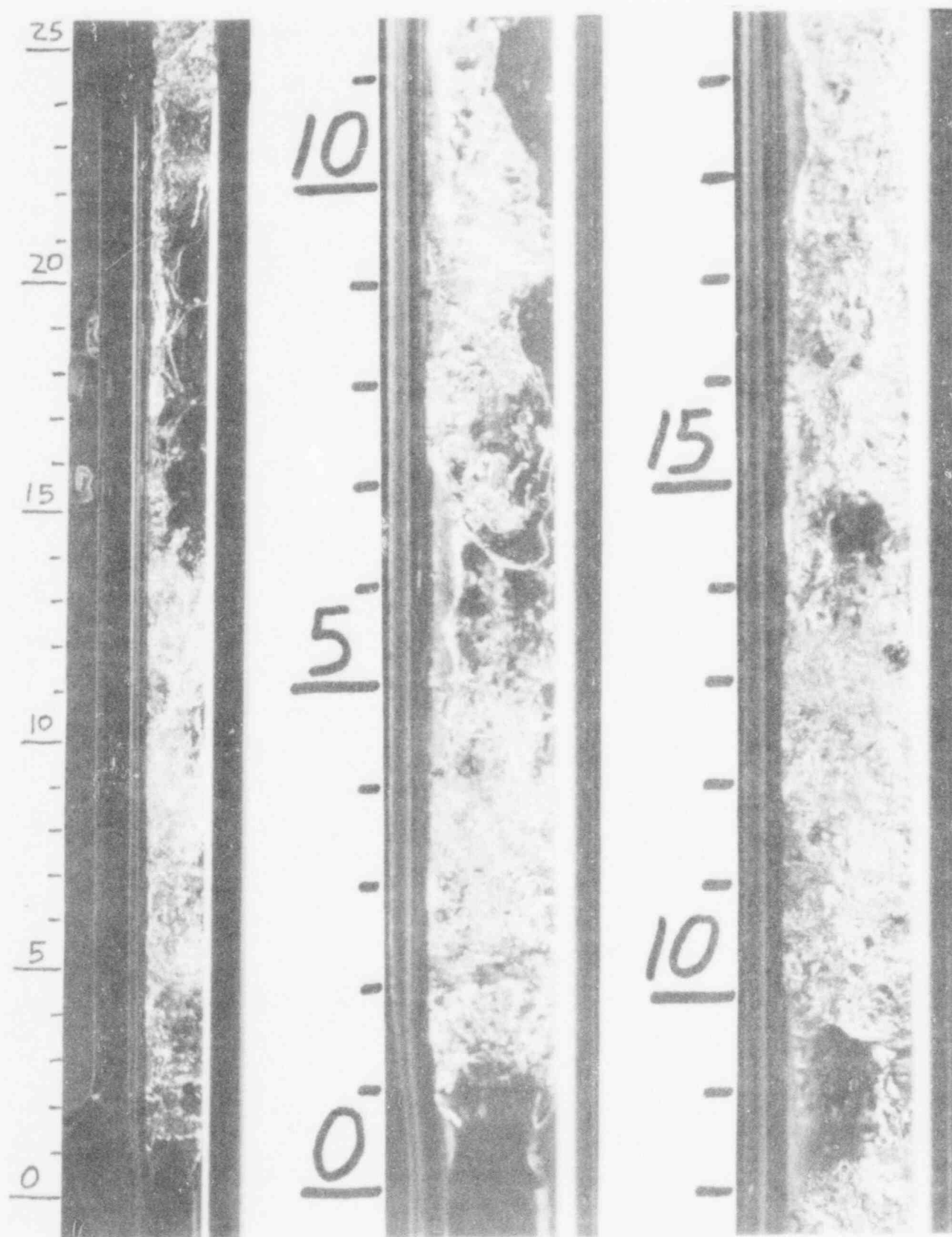


Fig. 28. $v_G = 97.0$ cm/s (He), $v_F = 10.5$ cm/s, $T_F = 24^\circ\text{C}$

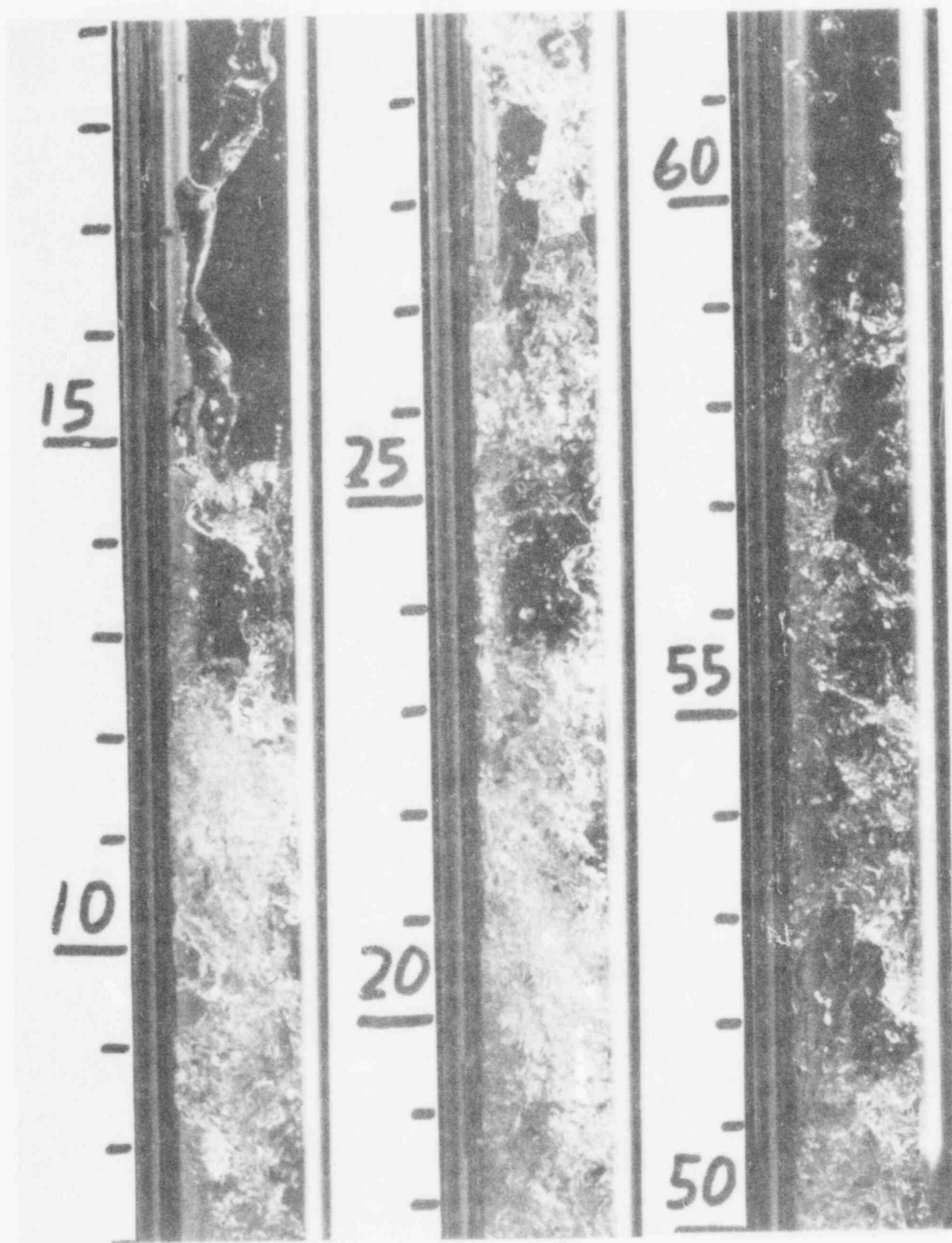


Fig. 29. $v_G = 159$ cm/s (He), $v_F = 10.5$ cm/s, $T_F = 24^\circ\text{C}$

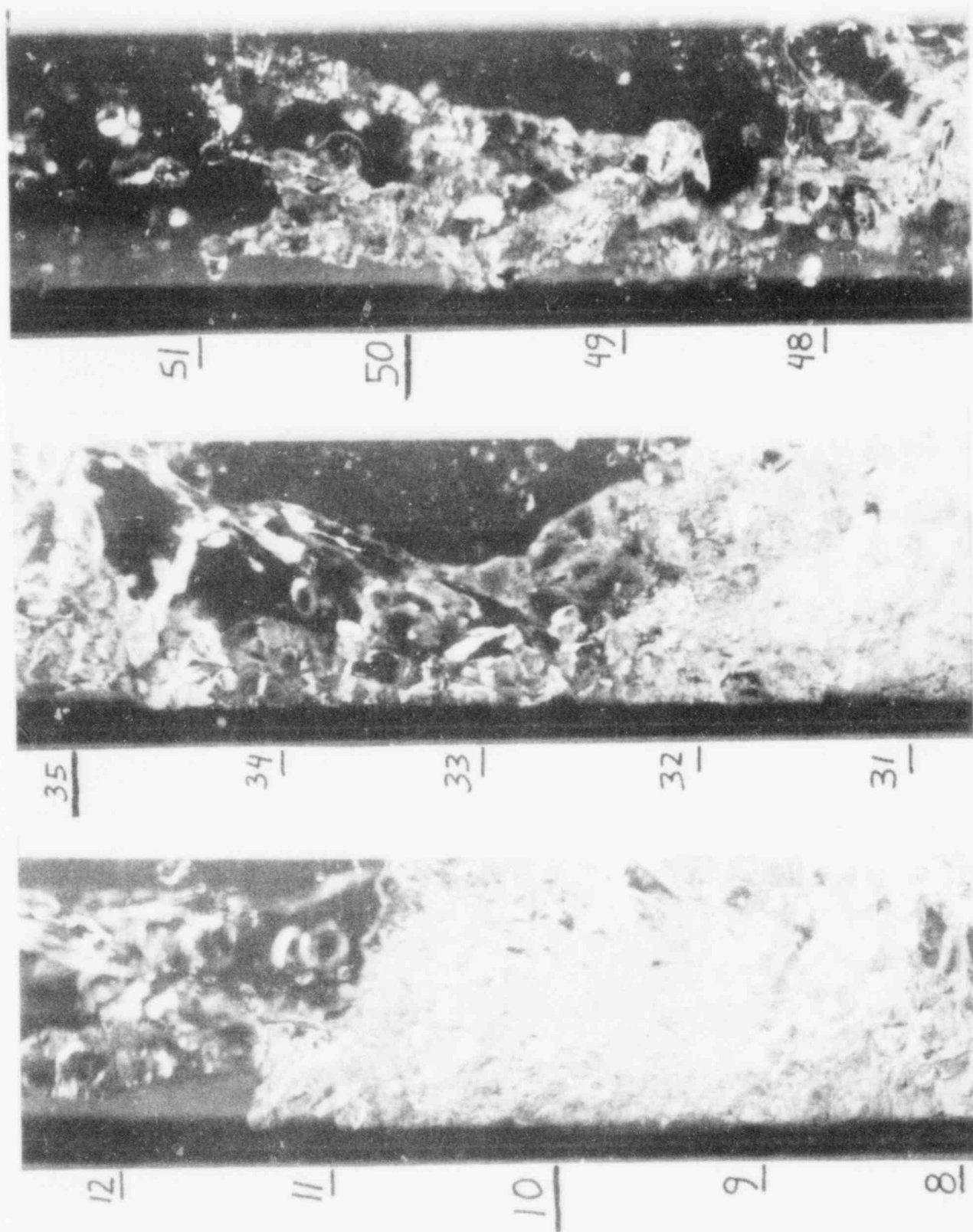


Fig. 30. $v_G = 66.3$ cm/s (He), $v_F = 10.5$ cm/s, $T_F = 24^\circ\text{C}$

1. Formation/Motion of Agitated Film/Dense Droplet Annuli

Motion pictures taken at various downstream distances (measured from liquid nozzle exit to center of film field of view) from the heated test section inlet were used to analyze the behavior of the agitated region and the subsequent ejection of agitated, thin annular masses. Selected data from this analysis is presented in Table VI. For each motion picture, the frequency of agitated mass ejection from the agitated region was determined by counting the number of such masses generated over a given number of frames. Velocities for these agitated liquid annuli were determined by tracking the leading or trailing edges of these masses as they progressed through a given length of the test section, typically 15 to 25 cm, and counting the number of film frames covering this motion.

From the large agitated mass velocities, one can immediately recognize that very large interfacial areas must be present, to cause such rapid acceleration beyond the bulk liquid velocity. And clearly, the agitated masses must be thin annuli. For example, in Trial 384, the following upper-bound estimate may be made, regarding agitated mass structure: The agitated masses observed leaving the agitated region for Trial 384 were roughly 3-5 cm in length, and were in continuous proximity to the heated wall. Even if all the inlet volumetric flux of liquid were to be ejected downstream in these agitated masses (assuming no evaporation, no dispersed flow, no core remnants), the frequency/rate of 5.9 masses ejected per second would indicate that each mass, 3 cm in length, with OD of 1.31 cm (assuming a 250 μm gap between agitated liquid and heated wall) could not be a solid liquid slug, and if a uniform annulus, would be only 0.9 mm thick. This is calculated by equating inlet liquid volumetric flowrate to volumetric flowrate contained in the ejected agitated masses.

Some general trends are indicated by the data in Table VI. For given inlet flow parameters, there are fewer intact agitated liquid annuli as one moves further downstream, away from the agitated region. However, the velocities of the agitated annuli remaining are quite similar to, although slightly higher than, the agitated mass velocities observed near the point where they are first ejected from the agitated region. As inlet liquid and/or gas velocities are increased, the frequency of agitated annulus ejection increases. This indicates the transition from chugging behavior, with a very long

Table VI. Agitated Annuli Formation/Motion Data

<u>Trial</u>	<u>Inlet T_F (°C)</u>	<u>Inlet v_F (cm/s)</u>	<u>Inlet v_G (N₂) (cm/s)</u>	<u>Downstream Distance (cm)</u>	<u>Agitated Mass Count or Freq. (number/second)</u>	<u>Average Velocity (cm/s)</u>	<u>Velocity Range (cm/s)</u>	<u>No. of Masses in Velocity Sample</u>
380	15	3.2	4.4	18	4.5	62.5	51-76	11
249	28	3.2	20.3	13	4.4	83.4	62-117	22
231	26	3.2	19.5	42	2.2	98.2	73-123	11
250	28	3.2	77.9	13	5.1	99.7	73-130	32
232	26	3.2	76.9	42	1.8	99.1	85-140	9
376	15	6.3	14.0	15	8.5	84.5	75-97	10
387	15	6.3	14.3	38	4.0	110.8	97-139	9
377	15	6.3	81.4	15	8.6	117.0	100-143	10
384	15	6.3	79.2	20	5.9	121.0	104-143	7
389	15	6.3	81.7	38	4.4	130.0	114-157	5
282	27	10.5	4.3	36	5.8	93.4	65-139	32
283	27	10.5	30.5	36	6.7	127.7	89-155	30
284	27	10.5	108.	36	7.8	176.0	154-230	40
375	15	20.6	58.5	15	12.9	117.	108-141	17
390	15	20.6	58.7	38	8.6	155.	134-178	11

unstable agitated region and substantial core liquid depletion, to a more continuous formation of agitated annuli with a smaller, more stable agitated region.

2. Droplets Generated in Agitated Region/Agitated Masses or Roll Waves

Roll wave entrainment of droplets, and droplet formation at the fine rough surfaces of the agitated region and agitated ejected masses, results in quite small droplets, with maximum sizes in the range of 500 μm , and with most droplets under 200 μm in diameter. These smaller droplets however are, for the most part, short-lived, and are less easily discerned with the photographic apparatus and lighting used in this experiment.

Examples of these droplet sizes resulting from roll waves and agitated surfaces are given in Fig. 31. In this figure, droplet count/measurement results for two experimental trials (both using He as the injected gas species) are presented. To obtain this data, photographs taken with a 200 mm lens (resolution down to roughly 25 μm , but limited depth of focus) focused at the depth corresponding to the outer (facing) surface of the liquid nozzle were analyzed. With this focussing, droplets within 2-3 mm of the heated wall nearest to the camera were in sharp focus. Droplets observed shearing from roll wave crests, or within approximately 1 cm of the leading (downstream) edges of agitated masses were measured, if they were in sharp focus. All other droplets were ignored. Droplets 50 μm in diameter or smaller were difficult to discern, curtailing the low end of the size distribution plot.

3. Dispersed Flow Droplet Sizes

Far downstream of the agitated region, liquid core remnants and agitated masses no longer are present, having dispersed into droplets and (for high liquid and gas inlet flows) small unstable slugs. The droplet sizes present in this dispersed droplet field are the results of the droplet formation mechanisms involved: roll wave entrainment, behavior at the agitated liquid surfaces, jet instabilities for the liquid core and/or core remnants and for the small ligaments forming upon agitated sheet break-up. In addition, maximum drop size is dependent upon the stability of droplets within the churn-turbulent and dispersed droplet flow fields downstream of the agitated

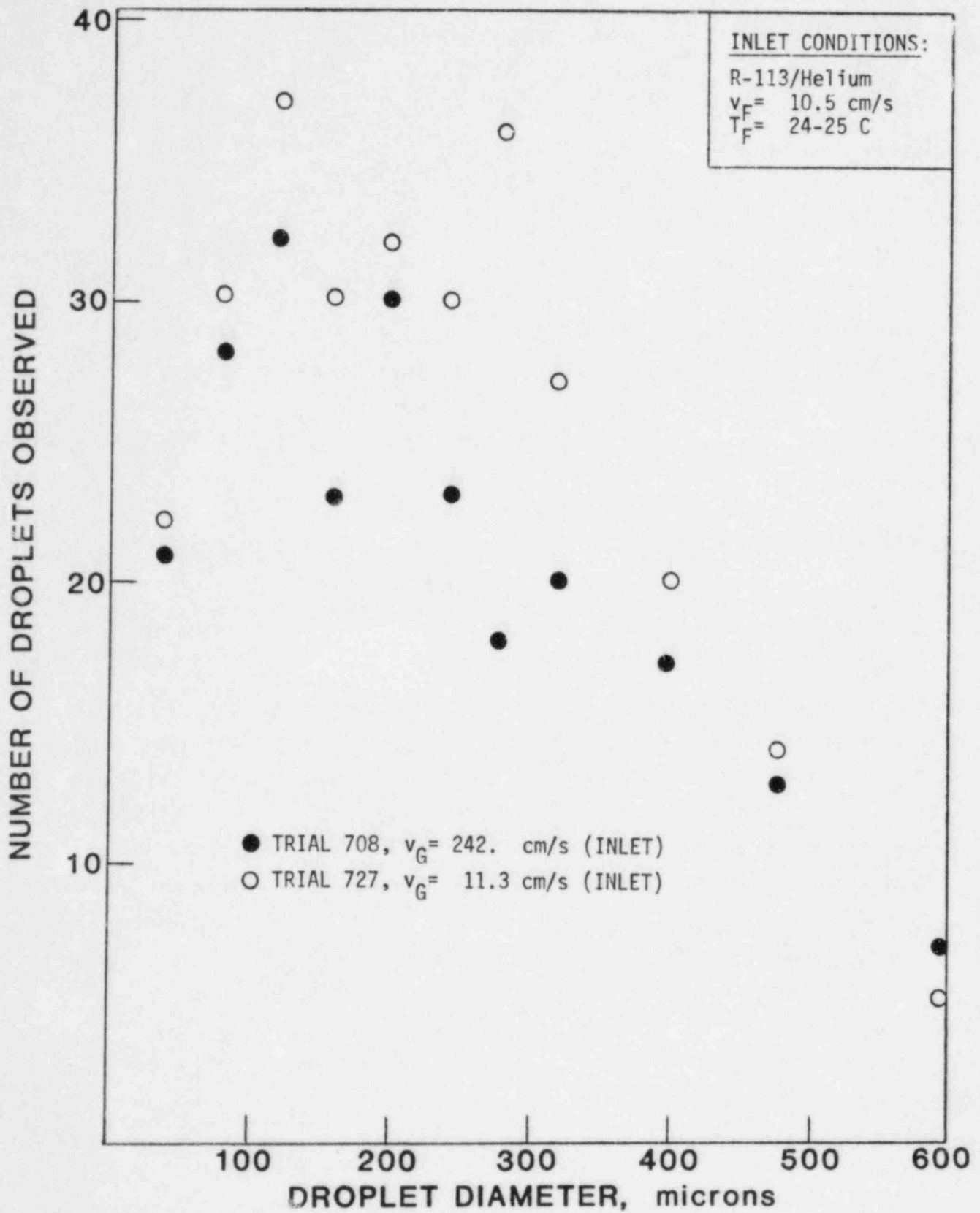


Fig. 31. Droplet Sizes from Roll Waves/Agitated Surface: Trials 708, 727

region. Typically, any droplets over 3 mm in diameter were observed to be distorted far from spherical shape, indicating that these larger droplets (or small slugs) were unstable, and would ultimately break-up into smaller droplets.

Examples of these dispersed flow droplet sizes are given in Fig. 32 for two experimental trials (both using N_2 as the injected gas species). To obtain this data, photographs taken using a 55 mm lens (resolution down to roughly 100 μm) were analyzed. Spherical or near-spherical droplets were recorded by diameter, while unstable, distorted slugs were measured along long and short axes, and recorded by estimated total volume (assuming cylindrical form, with short axis corresponding to diameter). As in Fig. 31, the difficulty in discerning smaller droplets, near the limits of resolution, curtails the low end of the droplet size distribution plot (in this case, droplets at or below 200 μm in diameter were difficult to discern). Also, far downstream of their point of formation, small droplets may be greatly or totally evaporated.

4. Flow Pattern Axial Positions

Moving downstream of the liquid inlet nozzle, several different flow patterns or regimes have been noted. First there is a stable, smooth inverted annular flow liquid core. Then the surface of this core becomes highly agitated, first with roll waves and then with a very fine agitated surface structure in close proximity to the heated wall. This agitated region is not of fixed length, as it periodically emits thin, agitated liquid annuli of continuous sheets or densely packed droplets, with lesser fluctuation for higher gas and liquid inlet flows. At very high inlet gas flows, roll wave entrainment causes substantial liquid core break-up before significant fine-structured agitated surface can form near the heated wall, while for very high inlet liquid flowrate, the stable liquid core extends for most of the test section length, with only minor surface agitation occurring near the test section outlet. Downstream of the agitated region, inverted slug/churn flow occurs, with liquid core remnants breaking-up due to jet instabilities and the agitated liquid annuli breaking-up into small droplets and ligaments. Far downstream, this break-up leads eventually to dispersed flow.

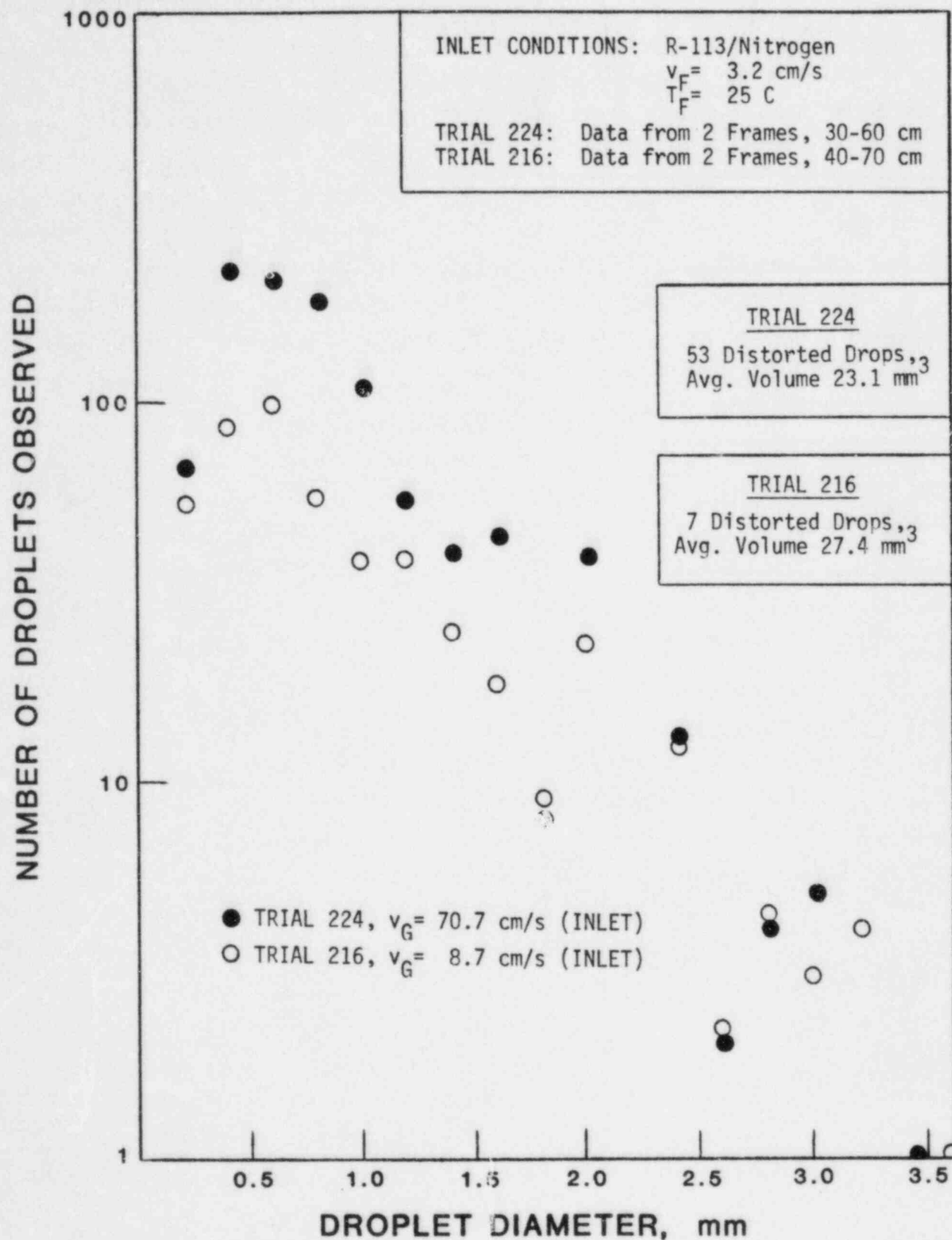


Fig. 32. Dispersed Flow Droplet Size Distribution: Trials 216,224

Examples of the axial positions or extents of these various flow patterns are given in Figs. 33 and 34 for two different values of inlet v_F and various inlet v_G values. Both N_2 and He were used as the inlet gas species. To obtain this data, photographs taken with a 55 mm lens (30 cm field of view) were analyzed. Given the fluctuating extent of the agitated region (i.e., chugging) and the subjective determination of when core remnants and agitated annuli have degraded to the extent necessary to be considered merely droplets in dispersed flow, the data points plotted in these figures are simply average values determined by reviewing the 16-20 photographic frames taken for each set of inlet flow conditions.

In Figs. 33 and 34, these results are plotted in terms of axial extent downstream for each flow pattern, versus the inlet value of the interfacial relative velocity times the square root of the inlet gas density. It can clearly be seen that flow pattern behavior is dependent upon this value of $v_{rel} \rho_G^{1/2}$, as the He and N_2 data represent a gas density range of 0.175 to 1.4 kg/m³. This is in general agreement with the results of the adiabatic simulation of inverted annular flow by Ishii and De Jarlais [9,39-42].

The correlation developed in this adiabatic simulation study, for stable liquid core length, is also plotted in Figs. 33 and 34. This correlation has the following form (with the subscript J representing liquid core jet, and L_B indicating intact core length):

$$L_B/D_J = 480 [Re_J]^{-0.53} \sqrt{We_J} ;$$

$$\text{for } [We_{G,rel}/\alpha^2] < 1.73 \quad (9)$$

and

$$L_B/D_J = 685 [Re_J]^{-0.53} \sqrt{We_J} [We_{G,rel}/\alpha^2]^{-0.645} ;$$

$$\text{for } [We_{G,rel}/\alpha^2] > 1.73 \quad (10)$$

where Eq. (9) represents varicose jet instability break-up, with minimal interfacial shear, and Eq. (10) represents sinuous jet instability break-up at moderate interfacial shear and represents roll wave entrainment break-up at

Fig. 33. Flow Pattern Axial Extents, $v_F = 4.2$ cm/s (Inlet)

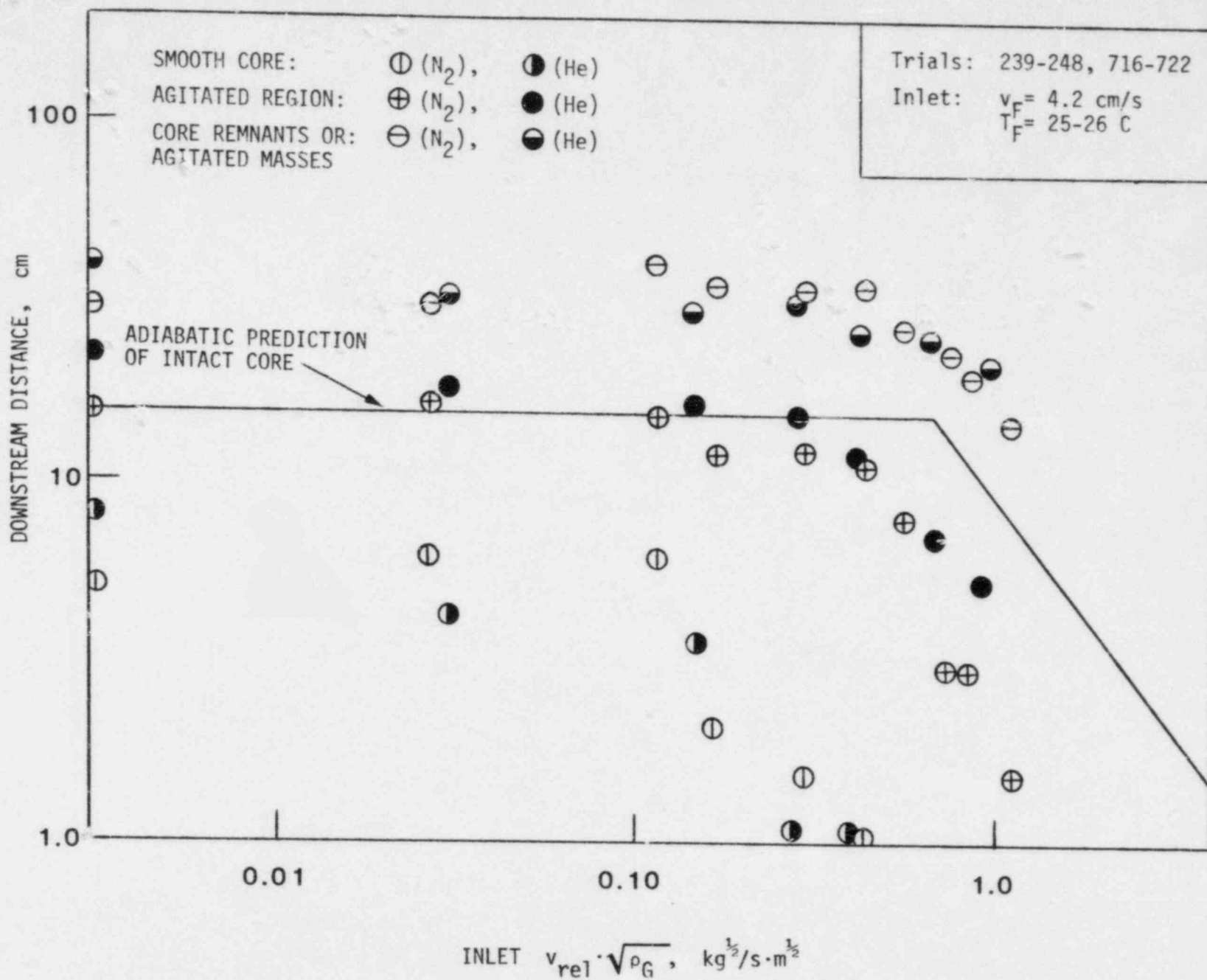
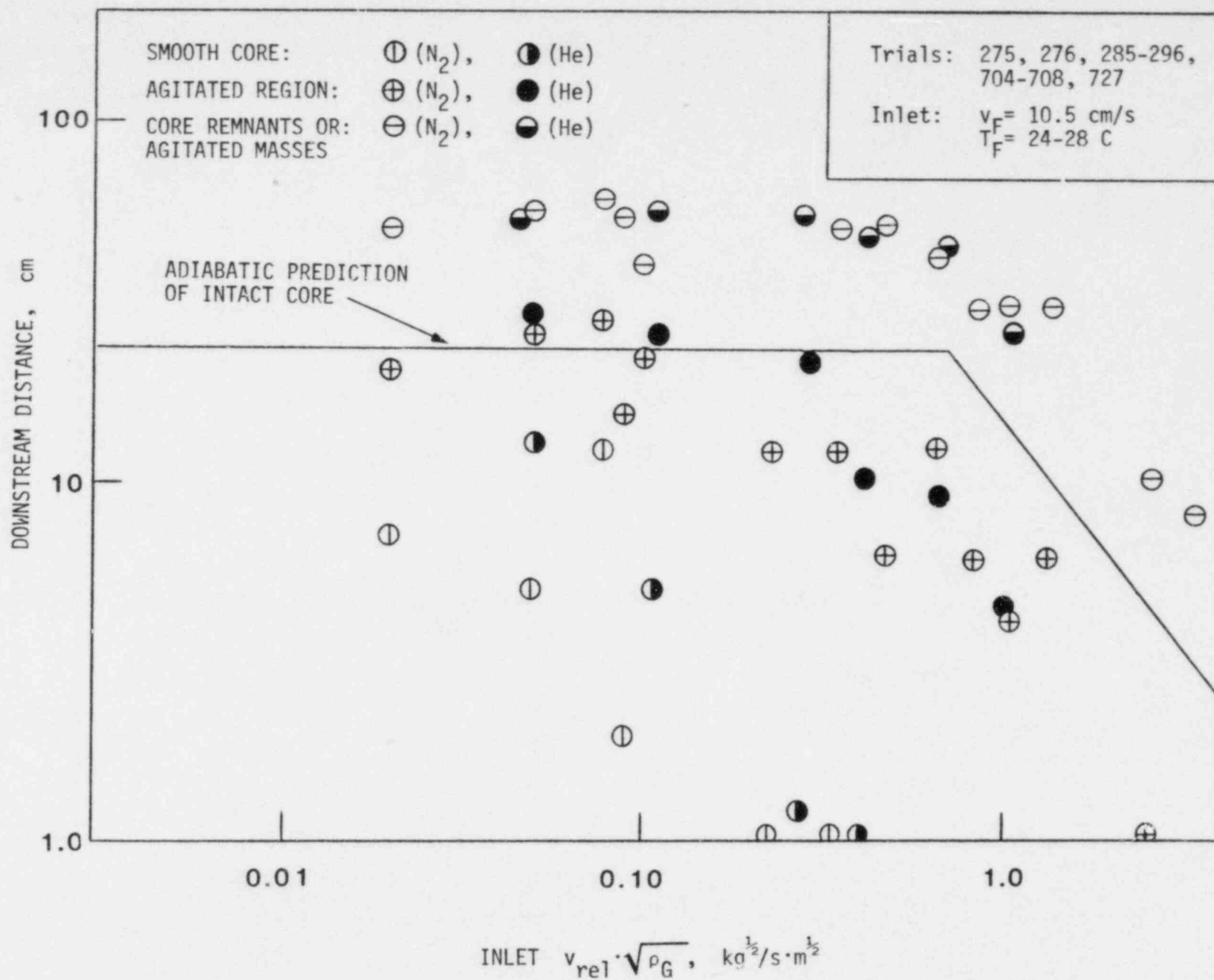


Fig. 34. Flow Pattern Axial Extents, $v_F = 10.5$ cm/s (Inlet)



high interfacial shear. The intact core lengths predicted by Eqs. (9) and (10) seem to correspond to the combined lengths of smooth stable core and agitated region for the present diabatic study, as plotted in Figs. 33 and 34. This correspondence extends to the fact that for the adiabatic simulation, downstream of the intact core was inverted slug/churn flow, just as, for the present diabatic study, downstream of the agitated region occurs an inverted slug/churn flow consisting of liquid core remnants and ejected agitated thin liquid annuli. This might reflect similar underlying break-up mechanisms for the combined smooth liquid core/agitated liquid core observed in the present study, with core liquid behavior obscured by the agitated surface of the agitated region.

V. CONCLUSIONS

A. Summary of Experimental Results

An experimental facility has been constructed and operated, in which steady state inverted annular flow film boiling of Freon 113 can be established in a transparent test section. The inlet to the test section is designed to allow the establishment of idealized inverted annular flow (liquid cylindrical core jet, surrounded by gas or vapor annulus) at the inlet, and to allow the inlet flow parameters of void fraction, v_F , T_F , v_G and ρ_G (by changing gas species) to be measured and varied systematically.

The following flow field observations have been made: Following a period of stable inverted annular flow with a smooth gas/liquid interface near the test section inlet, the liquid core surface becomes very agitated, in close proximity to the heated surface. The agitated region has a very fine structure (roughly less than 25 μm) of very large surface area. The agitated region seems to be initiated by the formation of roll waves at the liquid interface, but downstream of these initiating roll waves no surface detail can be discerned. The large interfacial area generated in the agitated region indicates large heat and momentum transfer rates. The large momentum transfer is manifested in the rapid formation and acceleration of long (roughly 3-5 cm) thin, highly agitated annuli of liquid, which periodically propagate downstream from the agitated region at velocities much greater than that of the bulk liquid. The formation of these agitated annuli deplete the liquid core

of much of its mass. Downstream of the agitated region is an inverted slug/churn flow field, with reduced-diameter liquid core remnants and rapidly moving agitated annuli. The core remnants break-up into slugs and droplets through jet instabilities, and the agitated annuli disperse into droplets and fine ligaments. Slugs, formed by jet instabilities, which are too large to be stable in the churn turbulent flow field incur secondary break-up through the formation of roll waves (for slugs of the same dimensions, roughly, as the flow passage) or through distortions into sheets and ligaments. The break-up of core remnants and agitated annuli eventually lead to dispersed flow, in which two size groups of droplets are present, resulting from the two basic droplet formation mechanisms observed: Droplets up to roughly 3 mm are formed by jet instabilities occurring in liquid core remnants and smaller ligaments, and represent the largest stable droplets which can exist in the flow field; and droplets under 600 μm , with most under 200 μm in diameter, are formed through roll wave entrainment, and entrainment from the agitated surfaces of the agitated region and ejected agitated liquid annuli.

The most significant of these above-mentioned phenomena, as far as the analysis of post CHF heat transfer is concerned, are perhaps the agitated region/agitated annuli and the smaller droplets formed at roll wave crests and at agitated surfaces. The very large interfacial area, in close proximity to the heated wall, for the agitated surfaces, results in very large momentum and heat transfer rates, far in excess of those associated with the other flow fields observed in the test section. These agitated surfaces, therefore, probably play a key roll in the precursory cooling of a hot wall downstream of the dryout point, for quenching phenomena. The dominance of the agitated region ejection of agitated annuli in the break-up of the liquid jet-like core of inverted annular flow at low gas and liquid flows is also a significant finding. Finally, the generation of many small droplets at roll wave crests and at the agitated surfaces effects the amount of vapor superheating which might occur, thereby limiting the degree of thermal nonequilibrium between the vapor and the liquid.

B. Comparison with Previous Post CHF Studies

In general, the flow field observations from the present experiment are in agreement with those of previous researchers, in that inverted annular,

inverted slug or churn flow, and dispersed flow have been observed [2,25,26, 28,30-32]. However, the details of the agitated region and ejected agitated annuli are a significant development in the understanding of this flow pattern, which acts as a transition regime between stable film boiling and dispersed flow, and which was first noted by Cadek et al. [36].

Unlike previous inverted annular flow studies in transparent test sections, the elimination of a quenching front and the establishment of steady state flow has eliminated the cyclic behavior associated with liquid superheating in the quench zone due to poor nucleation characteristics of smooth surfaces [30-32,33]. The present results, utilizing stable inlet conditions, are therefore more useful in the analysis of typical low quality film boiling applications.

The observation of droplet formation mechanisms, and the resulting droplet sizes, is an advance over previous studies, which were limited to the measuring of droplet sizes in the dispersed flow well downstream of the actual regions of droplet formation [29,37] and gave no information on how or where these droplets were formed. The droplet sizes reported in the present study are in general agreement with those reported in these previous studies, but the existence of smaller droplets, 50 μm in diameter or less, near roll wave crests and agitated surfaces, is a new finding. As in the study by Cumo et al. [38], two different droplet size ranges, resulting from two different droplet formation mechanisms, have been reported. However, this previous study related to annular flow prior to CHF, rather than post-CHF low quality flow, so that the vapor bubble bursting of Ref. [38] was not a factor in the formation of small droplets in the present study. However, the formation of larger drops from detached rivulets in this previous study is quite similar to the jet instability break-up of small ligaments or jet core remnants noted here.

The information on liquid core break-up presented here is complimentary to that given by Costigan and Wade [43]. In both studies, break-up of the liquid core through varicose or sinuous jet instabilities was noted. It is likely that the violent liquid core motion near the point of core break-up observed using their neutron radiography technique corresponds to the formation of the agitated region noted in the present study. While the agitated surface obscured the observation of the liquid core behavior using the present

optical method, neutron radiography could not detect the interfacial characteristics and droplet formation of the agitated region.

A significant advance resulting from the inlet design of the present test section is the decoupling of the hydrodynamics and heat transfer of inverted annular flow. The effects of variations in v_G , v_F , ρ_F and T_F could be studied independently. Among the results stemming from this capability is the demonstration of liquid core stability dependence upon the value of the flow parameter $\rho_G v_{rel}^2$. Similarly, it has been demonstrated that liquid core stability is enhanced by increased liquid inlet subcooling in much the same manner as by decreased inlet gas velocity, indicating the destabilizing effect of increased vapor generation within the stable film boiling inlet region.

Finally, the use of a heated test section, rather than the adiabatic simulation of the previous study [9,39-42] is a significant advance, in that the agitated region/agitated annuli were observed, the effect of liquid subcooling could be studied, and the flow fields downstream of the stable liquid core could be observed in detail, all because actual film boiling was occurring. The phenomena of jet instability break-up, roll wave entrainment, and the instability of large droplets in churn turbulent or dispersed flow, however, were greatly similar for both the previous adiabatic and the present film boiling experimental studies.

C. Postulated Modeling of Phenomena Observed

As previously discussed, the length of test section, downstream of the heated inlet, occupied by smooth, intact liquid core and by the subsequent agitated region seems to correspond to the intact liquid core jet length observed in the previous adiabatic inverted annular flow simulation [9,39-42]. Behavior similar to that observed in the adiabatic break-up of the liquid core was also observed in the reflooding tests by Costigan and Wade [43]. The correlations developed from the adiabatic test, [39-41], based upon the break-up mechanisms of free liquid jets [56-86] (see reviews in [40,41]), are the following (where the subscript J refers to liquid core jet, and L_B indicates intact liquid core length):

$$L_B/D_J = 480[Re_J]^{-0.53}\sqrt{We_J} ; \quad (9)$$

$$\text{for } [We_{G,rel}/\alpha^2] < 1.73$$

and

$$L_B/D_J = 685 [Re_J]^{-0.53} \sqrt{We_J} [We_{G,rel}/\alpha^2]^{-0.645}; \quad (10)$$

$$\text{for } [We_{G,rel}/\alpha^2] > 1.73$$

where Eq. (9) represents varicose jet instability break-up with minimal interfacial shear, and Eq. (10) represents sinuous jet instability break-up at moderate interfacial shear, and represents roll wave entrainment break-up at high interfacial shear. These equations seem to predict lengths corresponding closely to those observed for the combined smooth core/agitate core lengths. Given the more complicated geometry of the agitated region (compared to that of free jets or the adiabatic simulation of inverted annular flow), modifications to Eqs. (9) and (10) may be required.

Estimates for the sizes of slugs and drops formed during the jet instability break-up of the liquid core, core remnants, or small ligaments (either from core remnants or degraded agitated annuli) may be made, assuming the volume of the slugs/drops to be equal to that of a cylinder of diameter equal to the ligament, jet remnant, etc., and of length equal to the wavelength of maximum growth rate for the jet instability [86]. Correlations for this instability wavelength, developed from the adiabatic simulation [39-41], are as follows:

$$\lambda = 5.8 D_J; \quad (11)$$

$$\text{for } [We_{G,rel}/\alpha^2] < 1.73$$

and

$$\lambda = 7.6 [We_{G,rel}/\alpha^2]^{-0.5} \cdot D_J; \quad (12)$$

$$\text{for } [We_{G,rel}/\alpha^2] > 1.73$$

where, again, the value of $[We_{G,rel}/\alpha^2] = 1.73$ marks the boundary between varicose and sinuous jet instabilities. Given the jet remnant/ligament diameters observed, and the droplet sizes resulting from their break-up, the above equations seem to be consistent with the present experimental results.

The stability of slugs/droplets formed in the above manner can be analyzed by assuming that a drop will only be stable if, for churn turbulent two-phase flow, the flow around the drop is in the wake flow, rather than distorted particle, flow regime [87]. Using expressions for wake flow and churn turbulent flow relative velocities [10], a maximum stable droplet diameter can be found:

$$d_{max} = 4 \left(\frac{2\sigma}{g\Delta\rho} \right)^{1/2} N_{\mu G}^{1/3} \quad (13)$$

where $N_{\mu G}$ is the gas viscosity number based on the Taylor instability wavelength, and is defined as

$$N_{\mu G} = \frac{\mu_G}{(\rho_G \sigma \sqrt{\sigma/g\Delta\rho})^{1/2}} \quad (14)$$

This expression has proven to be accurate [87] in predicting the maximum droplet sizes reported in the FLECHT SEASET experiment [37], and is also in agreement with data from the adiabatic simulation of inverted annular flow [39-41].

Given the observation of roll wave entrainment in the present study, one can calculate minimum relative velocities at the local points, where such behavior occurs. In the analysis of roll wave entrainment in annular or stratified flow, Ishii and Grolmes [88] developed criteria for the inception of roll wave entrainment, based upon wave crest drag forces exceeding the retaining force due to surface tension. Their results compare favorably with many experimental studies. For rough turbulent liquid flow (as opposed to the flow of thin liquid films attached to a wall), their entrainment inception criterion are:

$$\frac{\mu_{FG}^j}{\sigma} \sqrt{\frac{\rho_G}{\rho_F}} > N_{\mu F}^{0.8} ; \quad (15)$$

$$\text{for } N_{\mu F} < 1/15$$

and

$$\frac{\mu_F j_G}{\sigma} \sqrt{\frac{\rho_G}{\rho_F}} > 0.1146 ; \quad (16)$$

$$\text{for } N_{\mu F} > 1/15$$

where the liquid viscosity number is defined as:

$$N_{\mu F} = \frac{\mu_F}{(\rho_F \sigma \sqrt{\sigma/g\Delta\rho})^{1/2}} \quad (6)$$

As demonstrated in the adiabatic simulation of inverted annular flow [9,39-42], the value of j_G does not accurately represent the local relative velocities at roll wave crests when liquid is in close proximity to a wall. For roll waves formed from the stable, smooth intact core, j_G should be replaced by v_{rel}/α [39-41]. However, further modification must be made when discussing local conditions in the agitated region.

Droplet size distributions for droplets generated at roll wave crests and at agitated surfaces seem to be similar to those observed in annular flow roll wave entrainment. Kataoka et al. [55] related the force balance on a ligament about to be torn from a roll wave crest to the interfacial shear stress in annular two-phase flow. Their results predict droplet sizes and size distributions in reasonable agreement with various experimental studies, including the adiabatic, inverted annular flow simulation [9,39-42]. Their expression for maximum droplet diameter is

$$d_{\max} = 0.088 \frac{\sigma}{\rho_G j_G^2} (Re_G)^{2/3} \left(\frac{\rho_G}{\rho_F}\right)^{-1/3} \left(\frac{\mu_G}{\mu_F}\right)^{2/3} \quad (17)$$

with an attendant size distribution expression which yields a volume mean diameter of

$$d_{vm} = 3.13 d_{max} \quad (18)$$

Again, to represent actual flow conditions at roll wave crests and the agitated surfaces of inverted annular flow, the value of j_G is not relevant. Work must be done to extend the above expression for application in inverted annular flow analysis.

ACKNOWLEDGMENTS

This work has been performed at Argonne National Laboratory, under the auspices of the U. S. Nuclear Regulatory Commission.

We would like to thank Dr. N. Zuber and Mr. M. Young of the NRC for their assistance in this research, and to thank A. Kras, S.-B. Kim, G. Lambert, D. Armstrong and L. Bova of ANL for their assistance during our design and construction of the experimental apparatus.

REFERENCES

1. Groeneveld, D. C., "Post-dryout Heat Transfer at Reactor Operating Conditions," presented at the Natl. Mtg. on Water Reactor Safety, American Nucl. Soc., Salt Lake City, UT, March 26-28, 1973.
2. Chi, J. W. H., "Slug Flow and Film Boiling of Hydrogen," J. Spacecraft, Vol. 4, p. 1329 (1967).
3. Zuber, N., Tribus, M., and Westwater, J. W., "The Hydrodynamic Crisis in Pool Boiling of Saturated and Subcooled Liquids," 2nd Intl. Heat Trans. Conf., Paper 27, Denver (1961).
4. Berenson, P. J., "Film Boiling Heat Transfer from a Horizontal Surface," J. Heat Transfer Trans. ASME, Vol. 83, p. 351 (1961).
5. Spiegler, P., Hopenfeld, J., Silberberg, M., Bumpus, C. F., Jr., and Norman, A., "Onset of Stable Film Boiling and the Foam Limit," Intl. J. Heat Mass Trans., Vol. 6, p. 987 (1963).
6. Henry, R. E., "A Correlation for the Minimum Film Boiling Temperature," AICHE Sym. Series 138, Vol. 70, p. 81 (1974).
7. Ishii, M. and Mishima, K., "Study of Two-fluid Model and Interfacial Area," ANL-80-111, NUREG/CR-1873 (1980).
8. Mishima, K. and Ishii, M., "Flow Regime Transition Criteria Consistent with Two-fluid Model for Vertical Two-phase Flow," NUREG/CR-3338, ANL-83-42 (1983).
9. Ishii, M. and De Jarlais, G., "Phenomenological Modelling of Two-phase Flow in Water Reactors at ANL (Inverted Annular Flow Modeling)," presented at the NRC 10th Water Reactor Safety Research Information Mtg., Gaithersburg, October 12-15, 1982.
10. Ishii, M., "One Dimensional Drift Flux Model and Constitutive Equations for Relative Motion between Phases in Various Two-phase Flow Regimes," ANL-77-47 (1977).
11. Coury, G. E. and Dukler, A. E., "Turbulent Film Boiling on Vertical Surfaces: A Study Including the Influence of Interfacial Waves," 4th Intl. Heat Trans. Conf., Paper B3.6, Paris (1970).
12. Ishii, M. and De Jarlais, G., "Hydrodynamics of Post CHF Region," Intl. Workshop on Fundamental Aspects of Post-dryout Heat Trans., Salt Lake City, April 2-4, 1984.
13. Bromley, L. A., LeRoy, N. R., and Robbers, J. A., "Heat Transfer in Forced Convection Film Boiling," Ind. Eng. Chem., Vol. 45, p. 2639 (1953).
14. Hsu, Y. Y. and Westwater, J. W., "Approximate Theory for Film Boiling on Vertical Surface," Chem. Eng. Progr., Sym. Ser. 56, Vol. 30, p. 15 (1960).

15. Kalinin, E. K., Berlin, I. I., and Kostyuk, V. V., "Film Boiling Heat Transfer," Advance in Heat Trans., Vol. 11, p. 51 (1975).
16. Groeneveld, D. C. and Gardiner, S. R. M., "Post CHF Heat Transfer under Forced Convective Conditions," Proc. Sym. on the Thermal and Hydraulic Aspects of Nucl. Reactor Safety, ASME, Vol. 1, p. 43, New York (1977).
17. Groeneveld, D. C., "Post Dryout Heat Transfer: Physical Mechanics and a Survey of Prediction Methods," Nucl. Eng. & Design, Vol. 32, p. 283 (1975).
18. Collier, J. G., "Post-dryout Heat Transfer -- A Review of the Current Position," Proc. NATO Advanced Study Inst. on Two-phase Flows and Heat Trans., II, p. 769, Istanbul (1977).
19. Mayinger, F. and Langner, H., "Post-dryout Heat Transfer," Proc. 6th Intl. Heat Trans. Conf., Toronto, Canada, Vol. 6, p. 181 (1978).
20. Clements, L. D. and Colver, C. P., "Natural Convection Film Boiling Heat Transfer," Ind. Eng. Chem., Vol. 62, p. 26 (1970).
21. Hsu, Y. Y., "A Review of Film Boiling at Cryogenic Temperatures," Advances in Cryogenic Eng., Vol. 17, p. 361 (1972).
22. Bressler, R. G., "A Review of Physical Models and Heat Transfer Correlations for Free-convection Film Boiling," Advances in Cryogenic Eng., Vol. 17, p. 382 (1972).
23. Hsu, Y. Y., "Film Boiling on Vertical Surface," Ph.D. Thesis, University of Illinois-Urbana (1958).
24. Arif Caglar, M. and Madsen, N., "Highspeed Cinematographic Investigation of Film Boiling Outside a Vertical Cylinder," Proc. NATO Advanced Study Inst. on Two-phase Flows and Heat Trans., p. 1133, Istanbul (1976).
25. Chi, J. W. H. and Vetere, A. M., "Two-phase Flow During Transient Boiling of Hydrogen and Determination of Nonequilibrium Vapor Fractions," Advanced Cryogenic Eng., Vol. 9, p. 243 (1964).
26. Chi, J. W. H., "Cooldown Temperatures and Cooldown Time During Mist Flow," Advanced Cryogenic Eng., Vol. 11, p. 330 (1966).
27. Chan, A. M. C., "Transient Two-phase Flows: Refilling and Rewetting of a Hot Horizontal System," Ph.D. Thesis, Dept. of Physics, McMaster University (1980).
28. Laverty, W. F. and Rohsenow, W. M., "Film Boiling of Saturated Nitrogen Flowing in a Vertical Tube," ASME J. of Heat Trans., Vol. 89, p. 90 (1967).
29. Forslund, R. P. and Rohsenow, W. M., "Dispersed Flow Film Boiling," ASME J. of Heat Trans., Vol. 90, p. 399 (1968).

30. Kalinin, E. K., Koshkin, V. K., Yarkho, S. A., Berlin, I. I., Kostyuk, V. V., and Kochelaev, Yu. S., "Heat Transfer in Tubes with Rod Regime in the Case of Film Boiling of a Subcooled Liquid," Cocurrent Gas Liquid Flow, p. 497, Plenum Press, New York (1969).
31. Kalinin, E. K., Koshkin, V. K., Yarkho, S. A., Berlin, I. I., Kochelaev, Y. S., Kostyuk, V. V., Korolev, A. L., and Sdobnov, G. N., "Investigation of Film Boiling in Tubes with Subcooled Nitrogen Flow," 4th Intl. Heat Trans. Conf., Paper B3.6, Paris (1970).
32. Kalinin, E. K., Yarkho, S. A., Berlin, I. I., Kochelaev, Yu. S., and Kostyuk, V. V., "Investigation of the Crisis of Film Boiling in Channels," Proc. Two-phase Flow and Heat Trans. in Rod Bundles, ASME Winter Annual Mtg., Los Angeles, CA (1969).
33. Banerjee, S., "Phenomenological Modeling of Reflood and Wave Propagation in Multiphase Flow," Workshop on Multiphase Thermal Hydraulics, Argonne National Laboratory, Argonne, Illinois, March 19-20, 1984.
34. Ishii, M., "Study of Flow Instabilities in Two-phase Mixture," Argonne National Laboratory Report ANL-76-23 (1976).
35. Jeglic, F. A. and Grace, T. M., "Onset of Flow Oscillations in Forced Flow Subcooled Boiling," NASA-TN-2821 (1964).
36. Cadek, F. F., Dominicis, D. P., and Leyse, R. H., "PWR FLECHT Final Report," Westinghouse Report WCAP-7665 (1971).
37. Lee, N., Wong, S., Yeh, H. C., and Hochreiter, L. F., "PWR FLECHT SEASET Unblocked Bundle, Forced and Gravity Reflood Task Data Evaluation and Analysis Report, NRUGE/CR-2256 (1981).
38. Cumo, M., Farello, G. E., and Furrer, M., "Experimental Remarks on Sputtering Phenomena and Droplets Generation in Falling Film Rewetting," Proc. ANS/ASME/NRC Intl. Mtg. on Nucl. Reactor Thermal Hydraulics, NUREG/CR-0014, Vol. 2, p. 1523, Saratoga Springs, NY (1980).
39. Ishii, M. and De Jarlais, G., "Inverted Annular Two-phase Flow Experiments and Modeling," 11th Water Reactor Safety Research Information Mtg., Gaithersburg, MD (1983).
40. De Jarlais, G., "An Experimental Study of Inverted Annular Flow Hydrodynamics Utilizing an Adiabatic Simulation," NUREG/CR-3339, ANL-83-44 (1983).
41. De Jarlais, G. and Ishii, M., "Hydrodynamic Stability of Inverted Annular Flow in an Adiabatic Simulation," Interfacial Transport Phenomena HTD 23, ASME Proc., p. 75 (1983).
42. De Jarlais, G. and Ishii, M., "Hydrodynamics of Adiabatic Inverted Annular Flow - An Experimental Study," 3rd Multiphase Flow and Heat Trans. Sym., Miami Beach, FL, April 18-20, 1983.

43. Costigan, G. and Wade, C. D., "Visualization of the Reflooding of a Vertical Tube by Dynamic Neutron Radiography," Intl. Workshop on Post-dryout Heat Trans., Salt Lake City, UT, April 1-4, 1984.
44. Graham, R. W., Hendricks, R. C., Hsu, Y. Y., and Friedman, R., "Experimental Heat Transfer and Pressure Drop of Film Boiling Liquid Hydrogen Flowing Through a Heated Tube," Advanced Cryogenic Eng., Vol. 6, p. 517 (1961).
45. Ottosen, P., "Experimental and Theoretical Investigation of Inverse Annular Film Flow and Dispersed Droplet Flow, Important Under LOCA Conditions," Riso National Laboratory Report No. R-424, Denmark (1980).
46. Kurilenko, A. A., Dymenko, S. R., and Kochelaev, Yu. S., "Phase Slip and Heat Transfer to the Liquid in Film Boiling of a Cryogenic Liquid in Piston Flow," J. Eng. Phys., Vol. 39, p. 961 (1980).
47. Nijhawan, S., Chen, J. C., Sundaram, R. K., and London, E. J., "Measurement of Vapour Superheat in Post-critical Heat Flux Boiling," ASME J. Heat Trans., Vol. 102, p. 450 (1980).
48. Gottula, R. C., Nelson, R. A., Chen, J. C., Neti, S., and Sundaram, R. K., "Forced Convective Nonequilibrium Post-CHF Heat Transfer Experiments in a Vertical Tube," Proc. ASME/JSME Thermal Eng. Joint Conf., Vol. 1, p. 151 (1983).
49. Jensen, R. T., "Inception of Liquid Entrainment during Emergency Cooling of Pressurized Water Reactors," Ph.D. Thesis, Utah State University (1972).
50. Vargaftik, N. B., Tables on the Thermophysical Properties of Liquids and Gases, 2nd Edition, Hemisphere Pub., Washington, D.C. (1975).
51. Weast, R. C. and Astle, M. J., Handbook of Chemistry and Physics, 61st Edition, The Chemical Rubber Pub. Co., Boca Raton, FL (1980).
52. Braker, W. and Mossman, A. L., Matheson Gas Data Book, 6th Edition, Searle Medical Products USA Inc., Lyndhurst, NJ (1980).
53. Technical Bulletin T-113A: Thermodynamic Properties of Freon-113, E. I. DuPont de Nemours Co., Wilmington, DE (1938).
54. Technical Bulletin: Guide to Rotameter Applications, Brooks Instrument Div., Emerson Electric Co., Bulletin No. 7-022 (1979).
55. Kataoka, I., Ishii, M., and Mishima, K., "Generation and Size Distribution of Droplet in Annular Two-Phase Flow," J. Fluid Eng. Trans. ASME Vol. 105, p. 230 (1983).
56. Weber, C., "Zum Zerfall eines Flussigkeitsstrahles," Z. Angew. Math. Mech., Vol. 11, p. 136 (1931).
57. Lord Rayleigh, "On the Instability of Jets," Proc. Lond. Math. Soc., Vol. 10, p. 4 (1878).

58. Lafrance, P., "Nonlinear Breakup of a Liquid Jet," Phys. Fluids, Vol. 17, p. 1913 (1974).
59. Christiansen, R. M. and Hixson, A. N., "Breakup of a Liquid Jet in a Denser Liquid," Ind. Eng. Chem., Vol. 49, p. 1017 (1957).
60. Tyler, E. and Watkin, F., "Experiments with Capillary Jets," Phil. Mag., Vol. 14, p. 849 (1932).
61. Grant, R. P. and Middleman, S., "Newtonian Jet Stability," AIChE J., Vol. 12, p. 669 (1966).
62. McCarthy, M. J. and Molloy, N. A., "Review of Stability of Liquid Jets and the Influence of Nozzle Design," Chem. Eng. J., Vol. 7, p. 1 (1974).
63. Phinney, R. E., "Stability of a Laminar Viscous Jet - The Influence of the Initial Disturbance Level," AIChE J., Vol. 18, p. 432 (1972).
64. Fenn, R. W. and Middleman, S., "Newtonian Jet Stability: The Role of Air Resistance," AIChE J., Vol. 15, p. 379 (1969).
65. Smith, S. W. J. and Moss, H., "Experiments with Mercury Jets," Proc. Roy. Soc., Vol. A-93, p. 373 (1917).
66. Miesse, C. C., "Correlation of Experimental Data on the Disintegration of Liquid Jets," Ind. Eng. Chem., Vol. 47, p. 1690 (1955).
67. Chen, T.-F. and Davis, J. R., "Disintegration of a Turbulent Water Jet," Proc. ASCE, Hyd. Div., Vol. 90, p. 175 (1964).
68. Litlaye, G., Pub. Sci. Tech. Secret. Aviation, (1942), as cited in Ref. 62.
69. Iciek, J., "The Hydrodynamics of a Free, Liquid Jet and Their Influence on Direct Contact Heat Transfer - II," Intl. J. Multiphase Flow, Vol. 8, p. 251 (1982).
70. Tyler, E. and Richardson, E. G., "The Characteristic Curves of Liquid Jets," Proc. Phys. Soc., Vol. 37, p. 297 (1925).
71. Phinney, R. E., "Breakup of a Turbulent Liquid Jet in a Low Pressure Atmosphere," AIChE J., Vol. 21, p. 996 (1975).
72. Iciek, J., "The Hydrodynamics of a Free, Liquid Jet and Their Influence on Direct Contact Heat Transfer - I," Intl. J. Multiphase Flow, Vol. 8, p. 239 (1982).
73. Baron, T., Tech. Rept. Univ. Illinois No. 4, (1949) as cited in Ref. 66.
74. Van de Sande, E. and Smith, J. M., "Jet Break-up and Air Entrainment by Low Velocity Turbulent Water Jets," Chem. Eng. Sci., Vol. 31, p. 219 (1976).

75. Ohnesorge, W., "Die Bildung von Tropfen an Dusen und die Anflosung flussiger Strahlen," Z. Angew. Math. Mech., Vol. 16, p. 355 (1936).
76. LiHaye, G., Compt. rend., Vol. 217, p. 99 (1943) as cited in Ref. 66.
77. Merrington, A. C. and Richardson, E. G., "The Break-up of Liquid Jets," Proc. Phys. Soc., Vol. 59, p. 1 (1947).
78. Levich, V. G., Physicochemical Hydrodynamics, Prentice-Hall, NY (1962).
79. Tanazawa, Y. and Toyoda, S., Trans. JSME, Vol. 20, p. 306 (1954) as cited in Ref. 62.
80. Lienhard, J. H. and Day, J. B., "The Breakup of Superheated Liquid Jets," J. Basic Eng. Trans. ASME, Vol. 92, p. 515 (1970).
81. Kusui, T., "Liquid Jet Flow into Still Gas," JSME Bulletin 5, Vol. 11, p. 1084 (1968).
82. Ivanov, V. A., "Disintegration of a Liquid Jet," J. Appl. Mech. Tech. Phys. USSR, Vol. 7, p. 19 (1966).
83. Nukiyama, S. and Tanasawa, Y., "Experiment on Atomization of Liquid," Trans. JSME, Vol. 5, p. 63 (1939).
84. Cunningham, R. G. and Doplin, R. J., "Jet Breakup and Mixing Throat Lengths for the Liquid Jet Gas Pump," J. Fluids Eng. Trans. ASME, Vol. 96, p. 216 (1974).
85. Filyand, L. V., "Instability and Breakup of Capillary Liquid Jets in a Parallel Airstream," Fluid Dynamics, Vol. 16, p. 424 (1981).
86. Tyler, E., "Instability of Liquid Jets," Phil. Mag., Vol. 16, p. 504 (1933).
87. Kocamustafaogullari, G. and Ishii, M., "A Preliminary Analysis of FLECHT SEASET Data and Assessment of These with Respect to Inverted Annular Flow Modeling," ANL/RAS/LWR 83-1 (1983).
88. Ishii, M. and Grolmes, M. A., "Inception Criteria for Droplet Entrainment in Two-Phase Cocurrent Film Flow," AIChE J., Vol. 21, p. 308 (1975).

Distribution for NUREG/CR-4277 (ANL-85-31)Internal:

C. E. Till	B. W. Spencer	T. C. Chawla
R. Avery	W. A. Ragland	T. Y. Wei
J. F. Marchaterre	G. De Jarlais (6)	A. M. Tentner
A. J. Goldman	D. P. Weber	M. Ishii (20)
P. A. Lottes	W. T. Sha	ANL Patent Dept.
L. W. Deitrich	Y. W. Shin	ANL Contract File
D. Rose	J. Sienicki	ANL Libraries
D. H. Cho	J. T. Hsu	TIS Files (3)

External:

NRC, Washington, for distribution per R2 and R4 (300)

DOE-TIC (2)

Manager, Chicago Operations Office, DOE

Reactor Analysis and Safety Division Review Committee:

- W. B. Behnke, Jr., Commonwealth Edison Co., P. O. Box 767, Chicago, Ill. 60690
- W. P. Chernock, Combustion Engineering, Inc., 1000 Prospect Hill Road, Windsor, Conn. 06095
- W. M. Jacobi, Westinghouse Electric Corp., P. O. Box 355, Pittsburgh, Pa. 15230
- S. Levine, NUS Corp., 910 Clopper, Gaithersburg, Md. 20878
- E. A. Mason, Standard Oil Co., P. O. Box 400, Naperville, Ill. 60566
- W. F. Miller, Jr., Los Alamos National Lab., P. O. Box 1663, Los Alamos, N. M. 87545
- M. J. Ohanian, University of Florida, Gainesville, Fla. 32511
- J. J. Taylor, Electric Power Research Inst., P. O. Box 10412, Palo Alto, Calif. 94303

NRC FORM 335 (2-84) NRCM 1102, 3201, 3202 SEE INSTRUCTIONS ON THE REVERSE		U.S. NUCLEAR REGULATORY COMMISSION		1. REPORT NUMBER (Assigned by TIDC add Vol. No., if any) NUREG/CR-4277 ANL-85-31	
2. TITLE AND SUBTITLE INVERTED ANNULAR FLOW EXPERIMENTAL STUDY				3. LEAVE BLANK	
5. AUTHOR(S) G. De Jarlais and M. Ishii				4. DATE REPORT COMPLETED MONTH: March YEAR: 1985 6. DATE REPORT ISSUED MONTH: April YEAR: 1985	
7. PERFORMING ORGANIZATION NAME AND MAILING ADDRESS (Include Zip Code) Argonne National Laboratory Reactor Analysis and Safety Division 9700 S. Cass Avenue Argonne, IL 60439				8. PROJECT/TASK/WORK UNIT NUMBER 60190103	
10. SPONSORING ORGANIZATION NAME AND MAILING ADDRESS (Include Zip Code) Division of Accident Evaluation Office of Nuclear Regulatory Research U. S. Nuclear Regulatory Commission Washington, D. C. 20555				9. FIN OR GRANT NUMBER A2026-4	
11a. TYPE OF REPORT Technical				11b. PERIOD COVERED (Inclusive dates) Jan. 1983 - Feb. 1985	
12. SUPPLEMENTARY NOTES					
13. ABSTRACT (200 words or less) <p>Steady-state inverted annular flow of Freon 113 in up flow was established in a transparent test section. Using a special inlet configuration consisting of long aspect-ratio liquid nozzles coaxially centered within a heated quartz tube, idealized inverted annular flow initial geometry (cylindrical liquid core surrounded by coaxial annulus of gas) could be established. Inlet liquid and gas flowrates, liquid subcooling, and gas density (using various gas species) were measured and varied systematically.</p> <p>The hydrodynamic behavior of the liquid core, and the subsequent downstream break-up of this core into slugs, ligaments and/or droplets of various sizes, was observed. In general, for low inlet liquid velocities it was observed that after the initial formation of roll waves on the liquid core surface, an agitated region of high surface area, with attendant high momentum and energy transfers, occurs. This agitated region appears to propagate downstream in a quasi-periodic pattern. Increased inlet liquid flow rates, and high gas annulus flow rates tend to diminish the significance of this agitated region.</p> <p>Observed inverted annular flow (and subsequent downstream flow pattern) hydrodynamic behavior is reported, and comparisons are drawn to data generated by previous experimenters studying post-CHF flow.</p>					
14. DOCUMENT ANALYSIS - a. KEYWORDS/DESCRIPTORS Film boiling Inverted annular flow Two-phase flow Post CHF hydrodynamics b. IDENTIFIERS/OPEN-ENDED TERMS Flow regimes Inverted annular flow Droplet				15. AVAILABILITY STATEMENT unlimited 16. SECURITY CLASSIFICATION (This page) unclassified (This report) unclassified 17. NUMBER OF PAGES 110 18. PRICE	